Setpoint control of motion systems with set-valued friction

Fresen, D.T.

Award date:
2018

Technische Universiteit
Eindhoven
University of Technology

Setpoint control of motion systems with set-valued friction

DC 2018.049

Master's thesis

Author:	D.T. Fresen	
Supervisor:	prof. dr. ir. N. van de Wouw	TU/e
Coaches:	ir. R. Beerens	TU/e
	ir. E. Verschueren	Thermo Fisher Scientific
	prof. dr. ir. W.P.M.H. Heemels	TU/e

Eindhoven University of Technology
Department of Mechanical Engineering
Section Dynamics and Control

In collaboration with Thermo Fisher Scientific

May 15, 2018

Abstract

Electron microscopy plays an essential role in the research of new, innovative materials, in drug development, and in the manufacturing process of the semiconductor industry. In an industrial electron microscope, a high-precision sample manipulation stage is employed to position the sample under the electron beam. In such high-precision positioning systems, friction is a performance limiting factor in terms of positioning accuracy and settling time, as it can induce non-zero steady-state positioning errors, limit cycling, and large settling times. These performance limitations are inherent to classical PID control, which is still employed in the vast majority of industrial applications.

The contribution of this thesis is twofold. First, a reset PID control strategy for improving the settling performance of a motion system subject to friction, presented in [1], is validated on an industrial nano-positioning motion stage. This experimental setup is representative for the sample manipulation stage used in various industrial electron microscopes. The experimental results presented in this thesis are submitted for journal publication in [2].

Secondly, the effects of flexible dynamics on stability and settling performance of a 2 DOF system subject to set-valued, non-collocated friction are investigated analytically. Friction-induced limit cycles are considered in particular, which can occur in flexible systems with higher-order dynamics, without the presence of a Stribeck effect in the friction characteristic, or the presence of an integrator in the controller. Based on this analysis, the intuition behind two novel control strategies for improving the settling performance of a flexible, 2 DOF system, subject to non-collocated, set-valued friction, is presented.

Contents

CHAPTER 1

Introduction

Electron microscopy is widely used in technology and science. Three major areas for microscopy are materials science, life sciences and electronics (e.g., semiconductor applications), each with its own performance requirements. Materials science focusses on innovative materials, which are used in exploring alternative energy sources, developing stronger, lighter materials, or nanodevices. In the study of new materials, the highest possible image resolution created by the microscope is desired in order to map the arrangement of all individual atoms in the material. The field of life sciences focuses on drug development and a better understanding of diseases and viruses. The samples in the Life Sciences industry are often organic, so in order to retain a samples' natural, native state without damaging them, delicate preparation and handling is required. In the semiconductor industry, electron microscopes are used in parallel to the manufacturing process of chips, and, specifically, the individual transistors, in order to quickly detect and correct any undesired process inaccuracies. The pace at which such an image can be created by the microscope is of high importance to achieve higher throughput and, consequently, reduce costs.

An electron microscope is a microscope that uses a beam of accelerated electrons as a source of illumination. Thermo Fisher Scientific produces microscopes that can achieve a resolution as small as 50 pm (0.05 nm) and magnifications up to 50.000.000x, compared to a maximum resolution of 200 nm and magnifications of 2000x achieved with traditional light microscopes. The three main types of electron microscopes are:

- Transmission electron microscopes (TEM),
- Scanning electron microscopes (SEM),
- Scanning transmission electron microscopes (STEM).

In transmission electron microscopes (TEM), see Fig. 1.1, an electron gun is used to produce a high voltage electron beam that (partially) passes through a sample. An image can be created by projecting the outcoming electron beam onto a fluorescent screen or by digitally recording it. TEM can achieve very high resolutions (50 pm), but

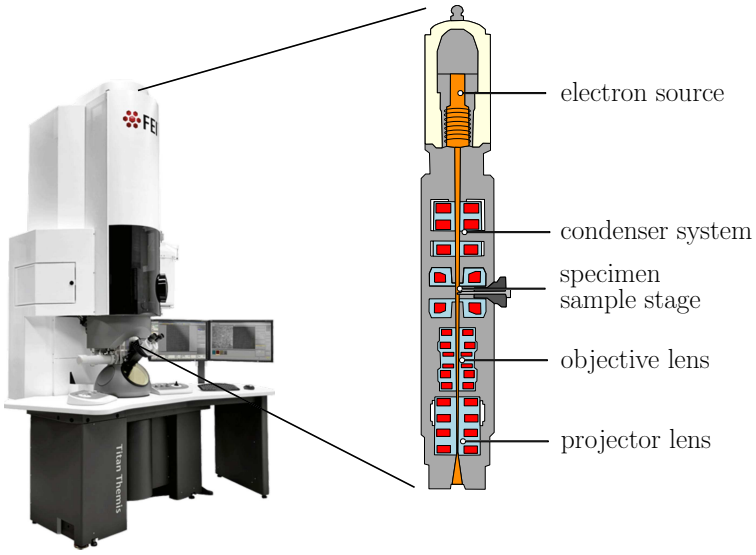

Fig. 1.1. Schematic representation of the FEI Titan TEM.

has the disadvantage that the samples have to be extremely thin ($\pm 0.1\mu$m), which can make sample preparation technically challenging.

In scanning electron microscopes (SEM), a focused electron beam is scanned across the surface of a sample to produce an image. Generally, the image resolution of a SEM is lower than that of a TEM. Since the electron beam only scans the surface of the sample, a SEM is able to image bulk samples of several millimetres in size in contrast to a TEM. An additional advantage of a SEM over a TEM is the possibility to identify the material composition of the sample by detecting characteristic X-rays using energy-dispersive X-ray spectroscopy.

A scanning transmission electron microscope (STEM) combines both principles and scans a focused electron beam across the sample, which is then transmitted through the sample to create an image. This technique combines the high resolution of a TEM with the possibility to identify material composition.

An additional technique used for sample preparation and analysis is the Focused Ion Beam (FIB). The FIB setup is similar to the SEM setup, but uses a focused ion beam, rather than electrons, which can 'mill' a specimen surface via sputtering with nm precision. This makes nano-machining possible to produce minute components or to remove unwanted material.

1.1 Sample manipulation stage

In all variations of electron microscopes, a high-precision sample manipulation stage is employed to position the sample under the electron beam, see Fig. 1.2. This motion stage can manipulate the sample in 5 degrees of freedom (DOF): three translations (x, y, z) and two rotations (R_x, R_y). The three translations and the R_y-rotation are considered frictionless, whereas the R_x-rotation suffers from significant friction instead,

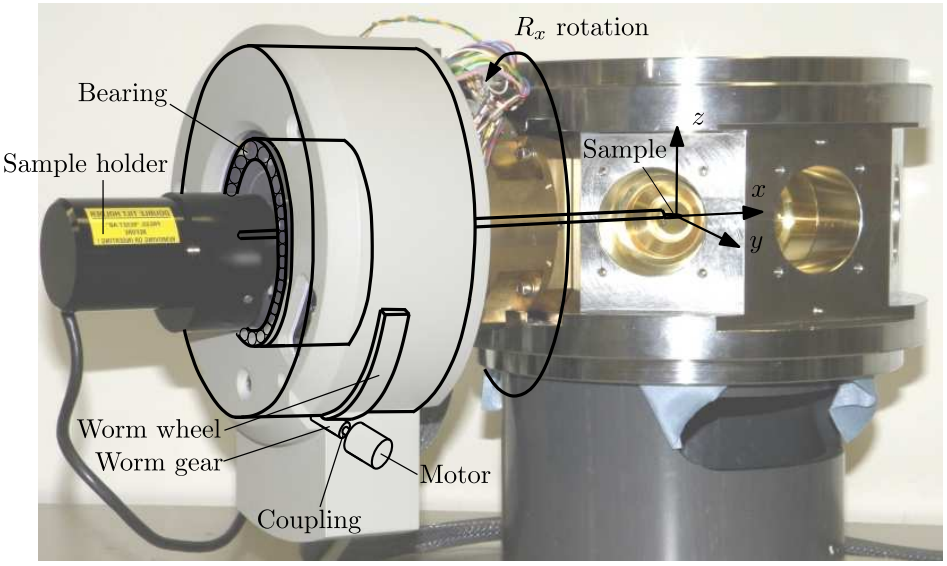

Fig. 1.2. The sample manipulation stage and the sample holder which are used in an electron microscope, including a schematic representation of the main components.

which limits the achievable positioning accuracy. The R_x-rotation is created by rotating the entire motion stage (including the sample holder) on a large bearing, inside the white housing in Fig. 1.2. A DC motor drives a worm gear, which is connected via a flexible coupling. This worm gear drives a worm wheel to which the motion stage is connected. The first significant source of friction is the lubricated contact between the worm gear and the worm wheel. Secondly, the R_x-rotation itself induces large amounts of friction due to rolling contacts of the main bearing and the rubbing of O-rings, which are needed to maintain the required vacuum in the microscope. In this thesis, the R_x DOF is explicitly considered, as this DOF particularly limits the achievable performance due to the apparent friction. It is intended to improve the performance by employing specific control strategies that are able to deal with these frictional effects.

1.2 Control strategies for systems subject to friction

Control of motion systems subject to friction has been an active field of research in the past decades. Two main control approaches can be distinguished when dealing with friction: model-based friction compensation and non-model-based control techniques.

Model-based friction compensation compensates the friction by including a parametric friction model in either a feedback or feedforward loop, see, e.g., [3–6]. This means that a model is required that accurately describes the friction. Various friction models can be used to describe the friction in a system, see, e.g., [7,8]. Three commonly used static models to describe friction on macroscopic level are shown in Fig. 1.3. The most basic friction model consists of only Coulomb friction F_c, depicted in Fig. 1.3a. The addition of viscous friction, which is proportional to the velocity, is depicted in Fig. 1.3b. In Fig. 1.3c, static friction F_s and a velocity-weakening Stribeck effect is added. However, to accurately describe the behaviour of high-precision motion system it is often

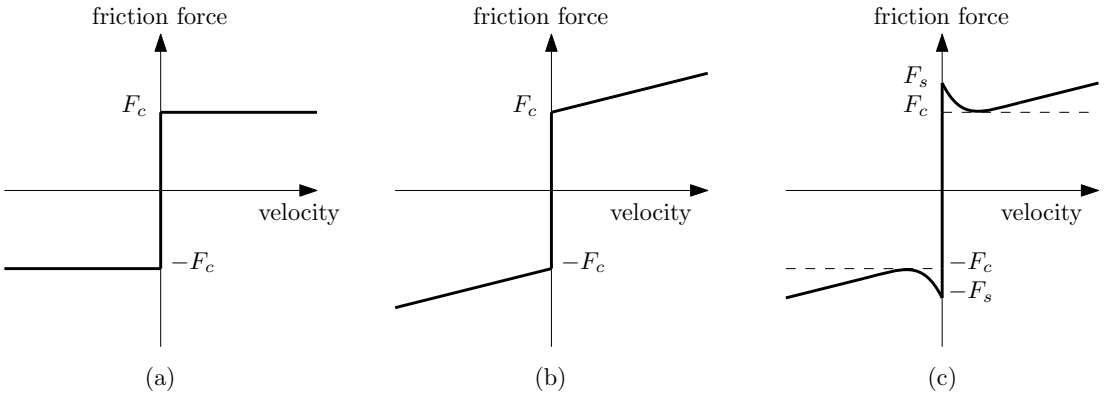

Fig. 1.3. Friction models: (a): Coulomb friction model; (b): Coulomb + viscous friction model; (c): Coulomb + viscous + static + Stribeck friction model.

necessary to also include microscopic frictional effects such as position-dependent local elastoplastic deformation of the various contact points [3], which significantly increases the complexity of the friction model. In practice, exact model-based friction compensation is not possible. Modelling errors and difficult to predict (time-varying) friction characteristics, due to, e.g., temperature differences, humidity, or wear, results in some level of under- or overcompensation when dealing with friction through compensation. Adaptive control may introduce a certain level of robustness against uncertain, or time-varying friction characteristics, see, e.g., [9, 10]. Inevitable modelling errors, however, still remain, which result in a deteriorated positioning performance.

Non-model-based techniques do not rely on accurate knowledge of the friction characteristics, but instead apply specific control signals to change the system response to obtain a desired performance despite the apparent friction. Examples of non-model-based control techniques are dithering-based techniques, see, e.g., [11,12], and impulsive control, see, e.g., [13–15]. The former employs high-frequency vibrations to smooth the discontinuity induced by the friction, whereas the latter uses impulsive control signals when the system gets in a stick phase with non-zero position error. Both these control techniques suffer from the same drawback in the sense that they risk exciting high-frequency system dynamics.

1.3 Problem description

Despite the existence of model-based and non-model-based control techniques for dealing with systems with friction, the vast majority of industrial applications still rely on classical, linear control techniques for achieving a desired performance. This is mostly due to the fact that these techniques are well understood and controller design based on frequency response functions (FRF) is relatively easy. In particular, the classical PID control is most commonly applied in systems with friction, since the integrator action results in compensation of unknown static friction. The current state-of-practice in controlling the sample manipulation stage also consists of classical PID control, including additional lead-, lag- low-pass- and notch filters.

However, due to the ever-increasing performance requirements in high-precision systems, the application of classical PID control unacceptably limits the achievable performance in terms of accuracy and settling times, illustrated in Section 3.3. The first major limitation of PID control applied to systems with friction is the possibility of inducing limit cycling, thereby losing asymptotic stability of the setpoint. Secondly, PID control may result in slow convergence and therefore long settling times, due to the (increasingly) slow depletion and refilling of the integrator buffer (when converging to the setpoint).

In order to overcome these limitations in the considered electron microscope motion stage, the addition of a second, short-stroke (piezo) actuator is investigated, see [16]. While it has been shown that this approach can be effective in improving the performance, both in terms of achievable accuracy and settling performance, adding an additional actuator results in increased complexity and cost of the system. Therefore, a preferred solution to deal with the current performance limiting friction is to apply smart control to the existing, single actuator system, as elaborated in Section 3.4.

1.4 Project goals

The goal of this project is twofold. First, a reset PID control strategy for improving the settling performance of a motion system subject to friction, presented in [1], is experimentally validated on an industrial nano-positioning motion stage. This experimental setup is representative for the sample manipulation stage used in various industrial electron microscopes, described above. The settling performance of the industrial motion stage needs to be improved such that, as a consequence, throughput can be increased. For a cost-aware solution, the aim is to increase the settling performance of the industrial motion stage without adding additional actuators, or making any other changes to the mechanical design. To this end, a smart (and cheap) hybrid control strategy is proposed in [1], to increase the settling performance of a single-mass (1 DOF) motion system, subject to set-valued friction.

Next, the 1 DOF model is expanded to a flexible 2 DOF model. The second goal is to analyse the effect of flexible (higher-order) dynamics on stability and settling performance of a motion system subject to set-valued Coulomb friction acting on the unactuated (non-collocated) mass. Accordingly, two stabilizing control strategies are proposed that aim at decreasing settling times, compared to the state-of-practice solutions.

1.5 Thesis outline

In Chapter 2, the nano-positioning stage, which is used as an experimental setup representative for the R_x-rotation stage in the microscope, is introduced. A parametric model representing this setup is constructed and estimates for the system parameters are derived. Using two different identification techniques, a non-parametric model is obtained and used to enhance the parametric model. Moreover, experiments are per-

formed to identify the friction characteristics.

Chapter 3 focusses on the control of a single-mass motion system, subject to set-valued friction. First, a model of both the system and the friction is given after which the control issues associated with PID-control of such a system are demonstrated in simulation. A hybrid control strategy for increasing the settling performance is introduced, as developed in [1], and experimentally implemented on the nano-positioning experimental setup, addressing the first goal of the project. Based on the experimental result, the achieved performance benefits, the influence of microscopic frictional effects, and repeatability, are discussed.

Chapter 4 expands the setpoint control problem from a 1 DOF case, to a flexible 2-mass-spring-damper system subject to non-collocated friction, addressing the second project goal. The model for this system is given, written in Lur'e-type form, after which an illustrative simulation example is used to identify the control problems regarding stability and settling performance. These control problems are analysed through a simulation-based bifurcation analysis and a more general Linear Matrix Inequality (LMI) approach. Subsequently, two control strategies for setpoint control are proposed, which address these stability- and performance issues.

CHAPTER 2

Nano-positioning motion stage

In this chapter, the nano-positioning stage, which is used as an experimental setup representative for the R_x-rotation stage in the microscope, is introduced. A parametric model representing this setup is constructed and estimates for the system parameters are derived. Using two different identification techniques, a non-parametric model is obtained and used to enhance the parametric model. Moreover, experiments are performed to identify the friction characteristics.

2.1 Description of the experimental setup

An experimental nano-positioning motion stage, shown in Fig. 2.1, is used to study the behaviour of the R_x rotation stage of the sample manipulation mechanism used in various industrial electron microscopes, described in Section 1.1. The setup consists of

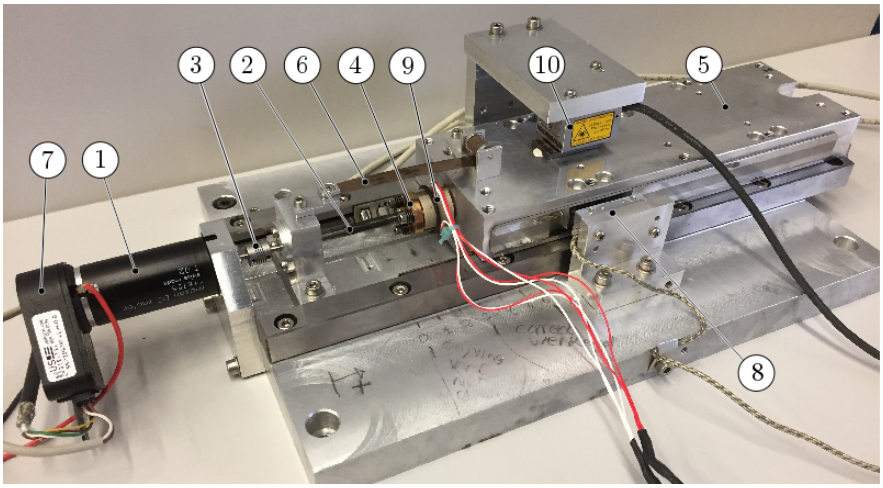

Fig. 2.1. The nano-positioning motion stage used as an experimental setup.

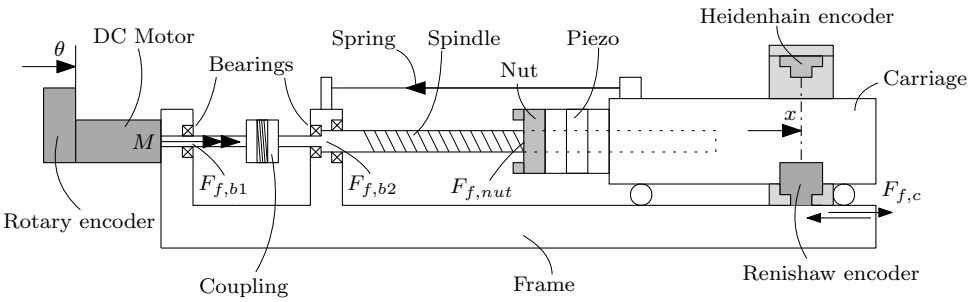

Fig. 2.2. Schematic representation of the nano-positioning stage used as an experimental setup.

a Maxon RE25 DC servo motor ① connected to a spindle ② via a coupling ③ that is stiff in the rotational direction while being flexible in the translational direction. The spindle drives a nut ④, transforming the rotary motion of the spindle to a translational motion of the attached carriage ⑤. A coiled spring ⑥ connects the carriage to the fixed world frame to eliminate any backlash between the spindle and the nut. The motor position is measured by a rotary encoder ⑦ with a transformed resolution of 100 nm. The position of the carriage is measured by a linear incremental Renishaw encoder ⑧ with a resolution of 1 nm. In addition, a piezoelectric actuator ⑨ is located between the nut and the carriage, and a linear Heidenhain encoder ⑩ with a resolution of 1 nm is positioned above the carriage. These last two components, however, will not be used in this research.

The experimental setup of Fig. 2.1 is a good representation of the R_x-rotation stage of the sample manipulation mechanism used in industrial electron microscopes, shown in Fig. 1.2. The worm gear driving the worm wheel of the microscope's motion stage is represented in the experimental setup as a spindle driving a nut. Note that the positioning performance of the microscope's motion stage is determined by the rotational accuracy, opposed to the translation accuracy in experimental setup.

Different sources of friction can be identified in the nano-positioning stage, which are similar to the sources of friction in the R_x-stage of the electron microscope. Friction induced by the bearing supporting the motor axis and the main axis, $F_{f,b1}$ and $F_{f,b2}$ in Fig. 2.2, respectively, contributes a small amount to the overall friction in system. The friction between the carriage and the frame, $F_{f,c}$, can be compared to the friction induced by the main bearing of the sample manipulation stage. The friction between the spindle and the nut, $F_{f,nut}$, contributes dominantly to the overall friction characteristic, and can be associated to the friction between the worm gear and worm wheel in the R_x-stage.

The objective is to control the position of the carriage to a desired constant position setpoint within an accuracy of 10 nanometer (nm), despite the various sources of friction, using non-collocation of sensing and actuation. Non-collocation of sensing and actuating means that additional dynamics are present between the location where the control force is applied and the location of the sensor used for position feedback control. The settling performance is defined as the time it takes for the system to settle within a specified error bound. A mathematical model of the dynamics of the system is required

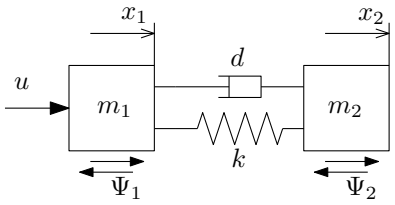

Fig. 2.3. Model of the nano-positioning motion stage used as an experimental setup.

to design a controller for this control objective. First, an analytical parametric model is derived based on the equations of motion, using estimates of the various mass- and stiffness components. Such a parametric model, however, is prone to estimation errors, which makes it difficult to obtain it at a sufficient level of accuracy. Therefore, system identification techniques are used to obtain a non-parametric model of the dynamics of the system from measured frequency response data. An accurate parametric model is obtained by adjusting the parameters of the analytical model, such that it matches the measured input-output relation.

2.2 Parametric system modelling

The nano-positioning motion stage is modelled as a 2-mass-spring-damper system, schematically shown in Fig. 2.3. The equations of motion (EOM) for this system can be written as the following differential inclusions:

$$\begin{cases} m_1\ddot{x}_1 = k(x_2 - x_1) + d(\dot{x}_2 - \dot{x}_1) + u - \Psi_1, \\ m_2\ddot{x}_2 = -k(x_2 - x_1) - d(\dot{x}_2 - \dot{x}_1) - \Psi_2. \end{cases} \tag{2.1}$$

Here, m_1 represents the equivalent mass containing the sum of the transformed motor- and spindle inertia. The moving carriage is denoted by m_2, and the stiffness k is a combined stiffness representing the flexibility of the nut, the spindle, the bearing and the piezoelectric actuator. A damper d represents the internal damping of the system. The motor exerts a transformed force u on m_1. The friction forces acting on m_1 and m_2 are denoted by Ψ_j, $j \in \{1, 2\}$, and satisfy the following set-valued force laws:

$$\Psi_j(\dot{x}_j) \in -F_{s,j}\text{Sign}(\dot{x}_j) - F_{v,j}(\dot{x}_j),\ j = 1, 2, \tag{2.2}$$

where $\text{Sign}(\cdot)$ denotes the set-valued sign function defined as

$$\text{Sign}(y) = \begin{cases} -1, & y < 0, \\ [-1, 1], & y = 0, \\ 1, & y > 0, \end{cases} \tag{2.3}$$

and the static friction and velocity-dependent friction terms are denoted by $F_{s,j}$ and $F_{v,j}(\dot{x}_j)$, respectively.

The derivation steps taken to construct this reduced-order 2 DOF model from a higher-order dynamic model of the setup, including the estimations of the various parameters, can be found in Appendix A.

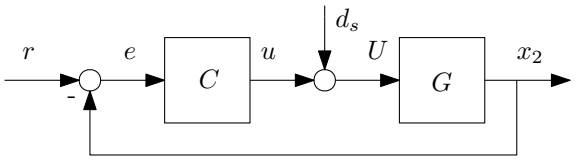

Fig. 2.4. Top level control loop.

2.2.1 Plant components

The standard, high-level position-feedback control loop to control the position of the load, x_2, to the desired setpoint, r, is shown in Fig. 2.4. Here, the position controller C outputs a force u, which is directly used as an input (with an optional addition of a disturbance signal d_s, used for system identification in Section 2.3), as is done in the model in (2.1).

On the actual setup, however, a command voltage, $\hat{V}_{com}$, is used as an input. The low-level block diagram is shown in Fig. 2.5, where G is expanded into its individual electronic and mechanical components, shown inside the red dashed lines. Based on a relative position error, a desired motor force, $\hat{u}$, is generated by the position controller C. This desired motor force is first converted to a desired command voltage, $\hat{V}_{com}$, through the linear transformation

$$\hat{V}_{com} = (\hat{u} + \hat{d}_s)\frac{i}{\hat{g}_m \hat{K}_T},$$

where i is the ratio between the rotation of the spindle and the resulting linear displacement of the carriage, $\hat{g}_m$ is the estimate of the amplifier gain, and $\hat{K}_T$ is the estimate of the motor gain. This digital signal is converted to a continuous voltage V_{com}, by a digital-to-analog converter (DAC). The amplifier converts this input voltage to a motor current I[1]. In order to generate a constant output current, a current control loop inside the amplifier regulates the voltage across the motor such that the desired output current is achieved. Additionally, a low-pass filter is present in the amplifier to reduce high-frequency noise.

The motor subsystem G_{motor} includes the conversion from voltage V to current I. The total current through the DC motor equals the voltage drop across the coil resistance R and the inductor L of the DC motor, minus the back-EMF term. For simplicity, it is assumed that the current is constant, so the inductance can be disregarded, resulting in

$$I = \frac{V - K_v \dot{x}_1}{R}.$$

This back-EMF term $K_v \dot{x}_1$ is essentially an electrical equivalent of a velocity-dependent friction term. The output current I through the motor, results in a transformed force u through the linear relation

$$u = \frac{I K_T}{i},$$

[1]The amplifier has two modes of operation: 1) velocity mode, where the command voltage V_{com} is scaled to an output voltage or 2) torque mode, where the command voltage V_{com} is scaled to an output current. In torque mode, the motor torque will not depend on the load, $T_m = K_m I$, so this mode of operation is used to guarantee good tracking of the output force.

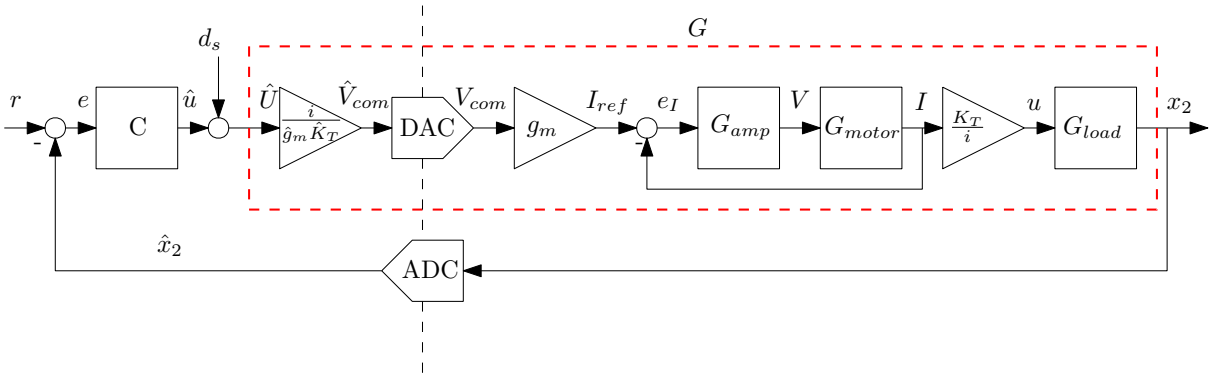

Fig. 2.5. Bottom level control loop, including the various components.

which acts on the mechanical system G_{load}. The actual position is measured and converted back to a digital signal by an analog-to-digital converter (ADC), and is used to close the feedback control loop.

Table 2.1: Signal definitions.

Parameter	**Description**
r	reference position for the load
e	positional error
$\hat{u}$	desired control force
u	actual control force
d_s	disturbance signal
$\hat{V}_{com}$	desired command voltage
V_{com}	actual command voltage
I_{ref}	reference current
e_I	current error
V	actual voltage across the motor
I	current trough the motor
x_2	position of the load
$\hat{x}_2$	estimated position of the load

2.3 Non-parametric system identification

In order to improve the analytical parametric model described in Section 2.2, the system's frequency response function (FRF) between the desired control force $\hat{u}$ and the position of the load x_2, is obtained using non-parametric identification techniques. An FRF consists of transfer function measurements at discrete frequencies, which mathematically describe the relation between the input and the output of a linear system, both in amplitude and in phase. This input-output relation can be used for controller design directly, without specific knowledge of the system parameters. However, doing so, results in the loss of physical understanding of the system characteristics. Therefore, the identification results are used to estimate the stiffness and damping parameters, k and d, respectively, of the analytical model, such that it fits the experimental input-

output behaviour, while maintaining knowledge of the physical characteristics of the system.

In this work, two different system identification methods are used for obtaining the FRF: a standard method using a non-periodic excitation signal, called the indirect three-point method [17,18], and a Local Polynomial approach using a periodic multisine excitation signal [17,19]. The linear dynamics of the system with friction are considered around a non-zero velocity setpoint. The principles of both identification methods are elaborated in Appendix B.

2.3.1 Indirect three-point method

The first method used to identify the plant dynamics G, as given in Fig. 2.5, is the indirect three-point method. This approach enables closed-loop identification of the dynamic input-output behaviour, which is often desired in practical applications. In the case of identifying the dynamic behaviour of the nano-positioning stage, a constant velocity setpoint of 0.1 mm/s is implemented, using a stabilizing PD-controller (which is designed based on the analytical model found in Section 2.2), to exclude, nonlinear, static frictional effects during the measurement. In a closed-loop setting, it is not possible to measure the plant G directly, due to a correlation between input U and the injection signal d_s through the feedback loop. By using the indirect three-point method to estimate the plant dynamics G, this problem is avoided. With this method, a band-limited white noise signal is injected just before the plant (signal d_s in Fig. 2.4), after which the Process Sensitivity PS is divided by the Sensitivity S. Referring to the block diagram in Fig. 2.4, these transfer functions are defined by:

$$S = \frac{1}{1+CG} = \frac{U}{d_s}, \tag{2.4}$$

$$PS = \frac{G}{1+CG} = \frac{e}{d_s}, \tag{2.5}$$

$$G = \frac{-PS}{S}. \tag{2.6}$$

In practice, however, any measurement is inherently disturbed by e.g. system non-

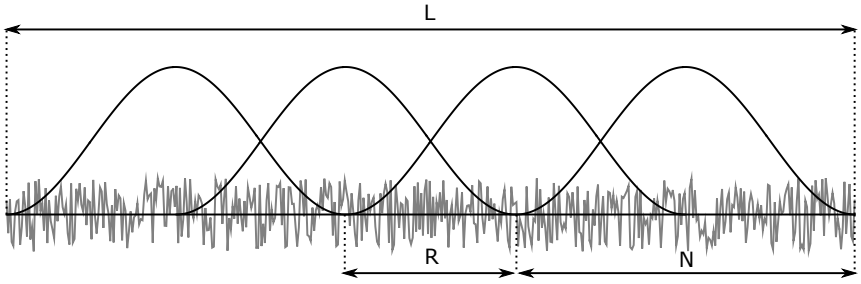

Fig. 2.6. Principle of the windowed overlapped segment averaging: the signal of length L is divided into M (4) windowed segments of length N with an overlap of $N - R$ samples.

linearities (friction, stick-slip, backlash, etc.), stochastic effects (noise, disturbance) and measurement errors. Therefore, to enhance the estimation of G, the entire data set L is divided into separate segments, each of length N. A Hanning window is applied to each frame to reduce leakage caused by the discontinuities as a result of this data segmentation. However, applying a window results in data loss at the frame boundaries. To resolve this, a total of M windowed frames are created with an overlap of $N - R$ samples, see Fig. 2.6. The values of the used parameters are given in Table 2.2. The resulting FRF measurement is shown in Fig. 2.8.

Table 2.2: Parameter values used in the three-point method for system identification.

Parameter	**Symbol**	**Value**	**Unit**
Measurement time	t	40	s
Sampling frequency	f_s	10000	Hz
Data set length	L	400000	samples
Frame length	N	40000	samples
Overlap	R	20000	samples
Number of frames	M	49	frames
Frequency resolution	f_{res}	0.25	Hz

2.3.2 Local Polynomial Method

The standard method of identifying the dynamical behaviour of a system described above, assumes that the plant G is linear. In practice however, the considered system is not linear, due to friction. Since a FRF is a linear relation from the input to the output of a system, the goal is to obtain a Best Linear Approximation (BLA) of the dynamical system behaviour, using a Local Polynomial Method (LPM). By using a periodic excitation signal (a multisine signal with equidistantly spaced frequencies from 1 to 2000 Hz), the LPM enables the separation of noise/transient effects from the systems dynamics, which significantly increases the quality of the plant estimation. The basic idea of the used LPM is as follows:

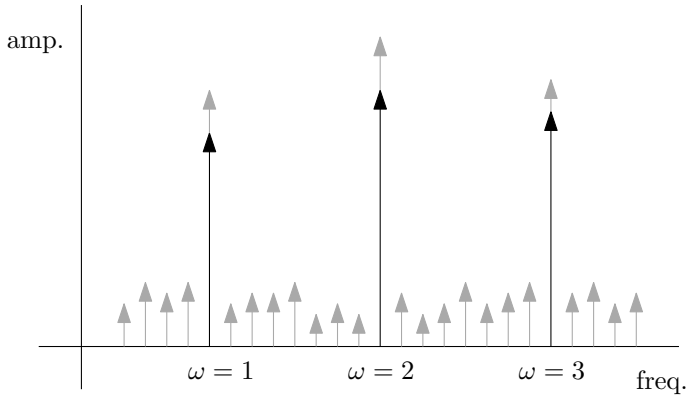

Fig. 2.7. Amplitude of the Fourier transform as a function of frequency. The excited frequencies are given by the black arrows, the transient and the noise contributions on all frequencies are given by the grey arrows.

- Excite the system at a certain known frequencies ω. This results in the schematic discrete Fourier transform (DFT) spectrum shown in Fig. 2.7, where the excited frequencies are clearly present (black arrow), but noise and transient effects are also present at the entire spectrum (grey arrows), also at non-excited frequencies.
- Fit a polynomial through a number of **non-excited** frequency bins around an excited frequency bin. These non-excited frequency bins only contain noise/transient effects.
- Interpolate this polynomial to find an estimate of the noise/transient effect at the **excited** frequency bin ω.
- Subtract this estimate from the excited frequency bin to obtain a 'noise-corrected DFT spectrum'.
- Fit a polynomial through the **excited** frequency bins of the corrected DFT spectrum.
- Interpolate this polynomial to find an estimate for the BLA at every frequency.

For a more detailed explanation, refer to Appendix B. The resulting FRF measurement is shown in Fig. 2.8.

2.4 System identification results

The resulting Bode plot, of the frequency response function from the motor force to the (non-collocated) position of m_2, obtained through both system identification techniques, is shown in Fig. 2.8. For the Bode plot of the frequency response function from the motor force to the (collocated) position of m_1, see Fig. B.5 in Appendix B. Both the three-point method and the LPM show roughly the same system behaviour. At low frequencies, a -10 dB/dec slope in the magnitude plot with corresponding -90 degrees phase can be observed. This decreases to a -20 dB/dec slope with -180 phase, before a resonance peak is observed at around 160 Hz. After the resonance peak, the slope tends towards -40 dB/dec with -360 degrees of phase.

For the three-point method measurement, at frequencies above 500 Hz, the magnitude of the output becomes sufficiently small for noise to become dominant. The measurement result obtained using the LPM remains relatively clear, even at high frequencies. This is partly due to averaging, inherent to the LPM. Two separate experiments have shown repeatable high-frequency behaviour, see Fig. B.6 in Appendix B, suggesting the presence of high-frequency dynamics, accurately measured up to 1000 Hz. These identification results are used to estimate the system parameters in (2.1). This revisited model is discussed in Section 2.6.

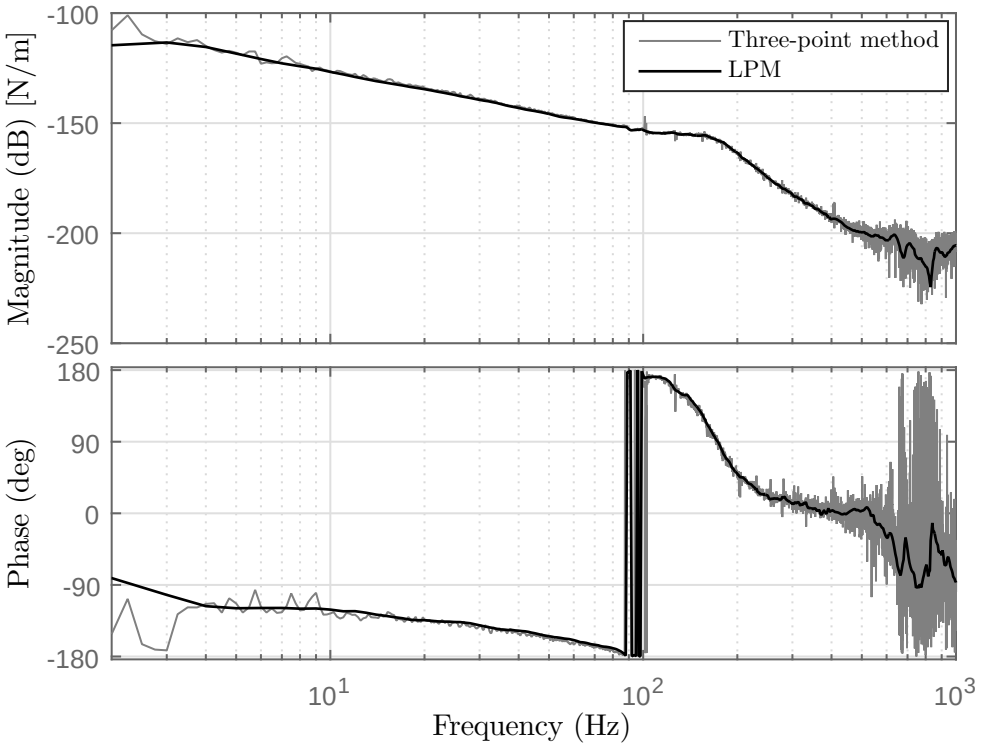

Fig. 2.8. Comparison between the experimentally found Bode plots, of the transfer function from the desired control force $\hat{u}$ to the (non-collocated) position of the carriage x_2, using the three-point method with noise injection (grey) and the LPM with multisine injection (black).

2.5 Friction identification

Friction experiments are performed to identify the friction characteristics. Separate experiments are performed to identify the static and viscous contributions of the friction.

2.5.1 Static friction experiments

The static friction present in the nano-positioning stage is experimentally obtained from breakaway experiments. This is done by gradually increasing the actuator force from zero until the stick-to-slip transition of the carriage is measured. At this point, the input force is approximately equal to the static friction force. An example of such a break-away experiment is shown in Fig. 2.9. It can be seen that defining a single stick-to-slip transition is not always straightforward, since this transition happens in stages. Therefore, two regions of movement are defined: macroscopic movement and microscopic movement.

On a microscopic scale, creep is observed, caused by microscopic frictional effects. On

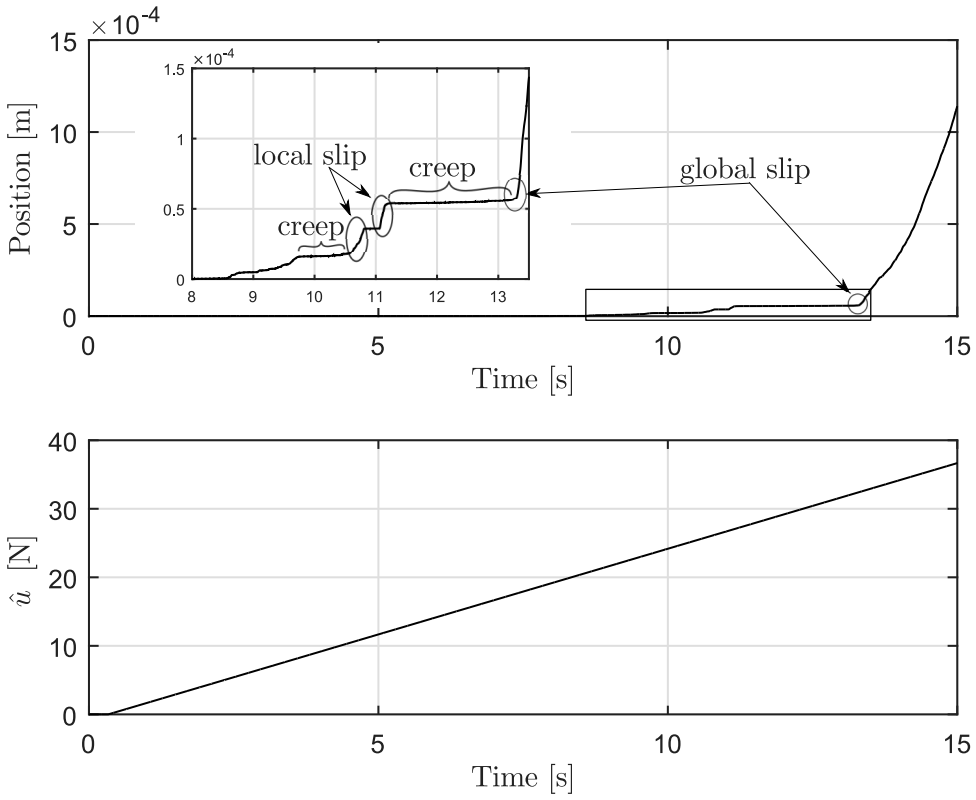

Fig. 2.9. Break-away experiment to obtain the static friction. Initially microscopic creep and stick-slip behaviour is observed, after which the system the system breaks away macroscopically.

this scale, two sliding surfaces can no longer be considered smooth, but instead have to be considered as two rough surfaces sliding over each other, as shown schematically in Fig. 2.10. The spindle and nut typically have a machining tolerance in the order of micrometers, which translates to a relatively rough surface when movement on a similar scale is considered. The contact points, asperities, of the sliding surfaces are constantly deforming, or even breaking (abrasion). This effect can be modelled as two relative moving surfaces connected by springs, see Fig. 2.11 [3]. In case of microscopic relative motions, such as creep, the asperities deform elastically, see Fig. 2.11b. These microscopic frictional effects are shown in Fig. 2.9, and play a significant role on the

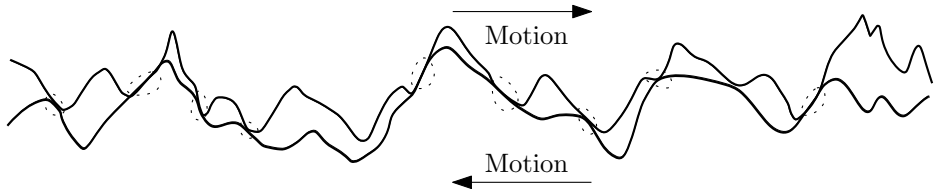

Fig. 2.10. The sliding of two rough surfaces resulting in microscopic creep and stick-slip behaviour.

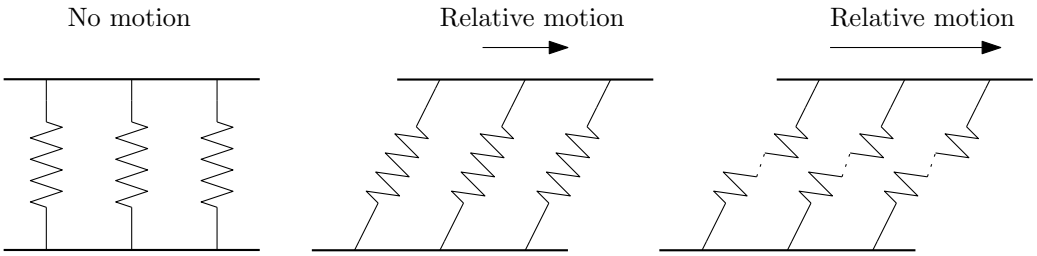

(a) No force applied

(b) Applied force is smaller than the break-away friction

(c) Applied force is larger than the break-away friction

Fig. 2.11. Model representing the finite stiffness of the asperities. For small relative motions, the two surfaces are connected by springs, resulting in microscopic elastic displacement, presliding. For larger relative motions, the springs snap, and macroscopic sliding occurs.

nano-scale in which the experimental setup operates, which will be further elaborated in Section 3.5.

For larger, macroscopic, relative motions, the asperities in Fig. 2.10 move over each other, or break, resulting in slip. This can be modelled as breaking of the springs, shown in Fig. 2.11c. Two variations of slip are defined: local slip, and global slip, shown in Fig. 2.9. With local slip, the spindle visibly rotates, but gets stuck again. These local stick-to-slip moments are due to mechanical imperfections in the setup, for example asymmetry of the spindle, which causes the friction to be dependent on the orientation of the spindle. Also, due to the system being overdetermined (both the duplex bearing and the carriage rail constrain the same sideways DOF), misalignment can amplify this stick-to-slip behaviour significantly. Dirt particles getting stuck between the spindle-nut contact area can also cause a significant increase in position-dependent friction, adding to the problem. Once the actuation force is larger than the static friction, the system slips globally. This experiment is repeated for different positions and for both directions of motion. The friction values for which the system breaks away in a global sense are shown in Fig. 2.12. This figure shows that the variance in static friction levels is minor, for different carriage positions.

2.5.2 Viscous friction experiments

The velocity-dependent part of the friction characteristic is obtained by performing closed-loop experiments where the carriage tracks a constant-velocity setpoint. Since the acceleration of the system is zero in this situation (ideally), and the velocity is non-zero, the EOM of (2.1) can be written as

$$\begin{cases} 0 = k(x_2 - x_1) + d(\dot{x}_2 - \dot{x}_1) + u - \Psi_1, \\ 0 = -k(x_2 - x_1) - d(\dot{x}_2 - \dot{x}_1) - \Psi_2, \end{cases} \tag{2.7}$$

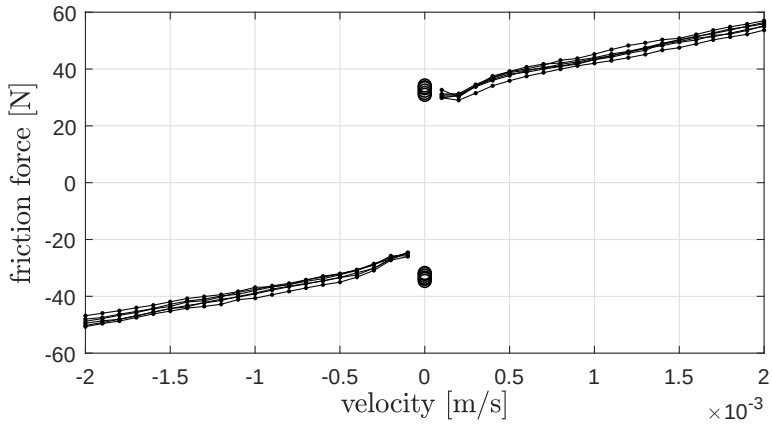

Fig. 2.12. Measured friction characteristic. The circles are static friction values obtained from breakaway experiments in Section 2.5.1, and the solid lines connect velocity-dependent friction values for different initial positions (Section 2.5.2).

which, after substitution, results in the force equilibrium where the total friction force is equal to the actuation force

$$u = \Psi_1 + \Psi_2. \tag{2.8}$$

This experiment is repeated for multiple velocities and for both directions of motion. The combined measurements, resulting in an overall friction characteristic, is given in Fig. 2.12. It consists of a static friction part, a viscous contribution and a slight Stribeck-effect. Note that the overall (combined) friction characteristic $\Psi_1 + \Psi_2$ is identified this way, not the individual contributions. Also note that this friction characteristic is only a momentary recording, since it can change significantly over time, due to factors such as wear, contamination and temperature. These modelling difficulties motivate the use of non-model-based control techniques, which are robust against all these uncertainties, and do not require an accurate (friction) model.

2.6 Parametric model revisited

The parametric model in (2.1) is now revisited. In particular, firstly, the stiffness and damping parameters, k and d, respectively, are estimated using the identification results of Section 2.3. The stiffness k is adjusted such that the resonance peak in the Bode plot presented in Fig. 2.8 occurs at 160 Hz, while the internal damping d is adjusted such that the height of this resonance peak matches the measurements. Secondly, using the knowledge of the friction identification experiments, linear dampers $d_{f,1}$ and $d_{f,2}$ are added between the fixed world and the first- and second mass, respectively, to represent both the back-EMF generated in the motor and the *macroscopic* viscous friction. The microscopic frictional effects in Fig. 2.11 are not included in this model. The resulting linear model is given by

$$\begin{cases} m_1\ddot{x}_1 = k(x_2 - x_1) + d(\dot{x}_2 - \dot{x}_1) + d_{f,1}\dot{x}_1 + u, \\ m_2\ddot{x}_2 = -k(x_2 - x_1) - d(\dot{x}_2 - \dot{x}_1) + d_{f,2}\dot{x}_2, \end{cases} \tag{2.9}$$

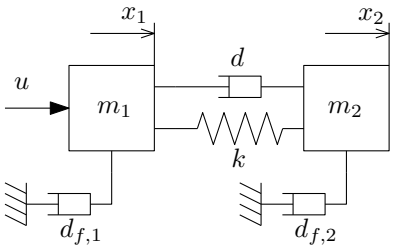

Fig. 2.13. Linear model of the experimental setup.

and is graphically represented by Fig. 2.13. The corresponding parameter values are given in Table 2.3. A comparison between the model-based and the experimentally found Bode plots of the frequency response function from the motor force to the (non-collocated) position of m_2, is shown in Fig. 2.14. The -1 slope in the magnitude plot, and corresponding $-90°$ phase, is a result of the viscous damping $d_{f,1}$ and $d_{f,2}$. At high frequencies, the phase of the experimentally found FRF drops, while the phase of the model-based FRF rises. This is due to the low-pass filter, present in the amplifier, which is not included in the model.

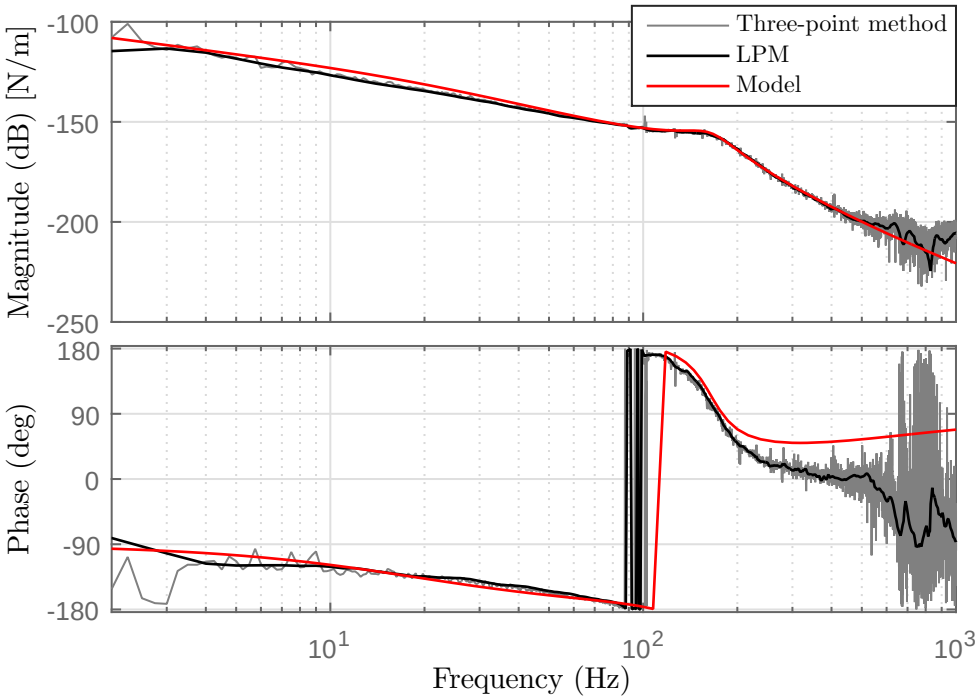

Fig. 2.14. Comparison between the model-based (black) and the experimentally found Bode plots of the frequency response function from the motor force to the (non-collocated) position of m_2, using the three-point method with noise injection (grey) and the LPM with multisine injection (red).

Table 2.3: Adjusted model parameters to fit the experiments.

Parameter	**Value**	**Unit**
m_1	171	kg
m_2	1.6	kg
d	550	N s/m
$d_{f,1}$	20000	N s/m
$d_{f,2}$	10	N s/m
k	1.7e6	N m

2.7 Discussion

A nano-positioning stage is used as an experimental setup to represent the sample manipulation stage in the electron microscope. A linear, non-parametric model of the experimental setup is obtained using two different system identification techniques, i.e., the indirect three-point method, and a Local Polynomial Method (LPM). Both methods give similar results, although the FRF obtained using the LPM is more accurate, especially at higher frequencies.

Separate experiments have been performed to identify the friction present in the experimental setup. On a macroscopic scale, the static friction has been experimentally obtained from breakaway experiments and the viscous friction is obtained by performing closed-loop experiments where the carriage tracks a constant-velocity setpoint, indicating the presence of a slight Stribeck effect. Microscopic frictional effects, causing microscopic creep and stick-to-slip behaviour, have been identified, but (due to the high complexity) not included in the model.

A parametric 2-mass-spring-damper model of the experimental setup is constructed, where linear dampers are added between the fixed world and the first- and second mass, respectively, to represent both the back-EMF generated in the motor, and the macroscopic viscous friction. The stiffness and damping parameters are estimated using the identification results, resulting in a parametric model that fits the experimentally obtained FRF.

CHAPTER 3

Validation of reset control of single-mass motion systems with friction

This chapter focusses on setpoint control of a single mass, subject to set-valued friction, where in particular the settling performance is addressed. First, a model of both the system and the friction is given, after which the control issues associated with PID-control of such a system are demonstrated in simulation. A hybrid control strategy for increasing the settling performance is introduced, based on [1], and experimentally validated on the nano-positioning experimental setup. Based on the experimental results, the achieved performance benefits, the influence of microscopic frictional effects, and repeatability, are elaborated.

3.1 Introduction

The simplest way to model a motion system is as a single-degree-of-freedom mass m, shown in Fig. 3.1. Despite its simplicity, a single inertia model is often a good approximation of a motion system in the low- to medium frequency range. This is the frequency range of interest, due to the low velocities involved in the final settling stage, considered in this section. A single mass model is a good representation for the

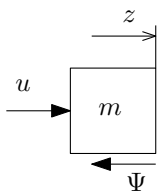

Fig. 3.1. Schematic representation of a single sliding mass subject to friction.

behaviour of the nano-positioning stage up to approximately 160 Hz, see Chapter 2, which will be used as an experimental setup in Section 3.5. This chapter is organized as follows. Section 3.2 introduces the system and friction model of interest. The control issues associated with PID control of single-mass systems subject to friction are demonstrated in simulation in Section 3.3, and a reset PID controller is introduced in Section 3.4 to address these issues specifically. Lastly, the reset controller is validated on the experimental setup in Section 3.5.

3.2 System and friction model

The single-mass system dynamics are given by the differential inclusion

$$\begin{aligned} \dot{z}_1 &= z_2, \\ \dot{z}_2 &= \frac{1}{m}(-\Psi(z_2) + u). \end{aligned} \tag{3.1}$$

Here, z_1 and z_2 represent the position and velocity of the mass, respectively. The mass is subject to a set-valued friction force Ψ, which is induced by a friction model including Coulomb friction, a viscous contribution and a velocity-weakening Stribeck effect, see Fig. 3.2. The friction force complies with the following set-valued force law:

$$\Psi(z_2) \in F_s \mathrm{Sign}(z_2) + \gamma z_2 - f(z_2), \tag{3.2}$$

where the Stribeck contribution is given by

$$f(z_2) = (F_s - F_c)\frac{\delta z_2}{1 + \delta |z_2|}. \tag{3.3}$$

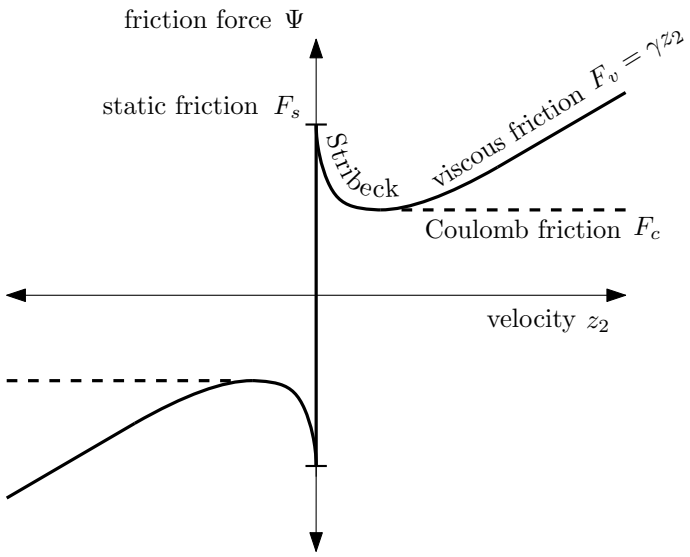

Fig. 3.2. Friction characteristic including the static friction F_s, Coulomb friction F_c, viscous friction $F_v = \gamma z_2$ and a velocity-weakening Stribeck effect.

Here, δ is a Stribeck shape parameter, F_s is the static friction, γz_2 is the viscous friction, F_c is the Coulomb friction, and $\text{Sign}(\cdot)$ denotes the set-valued sign function defined in (2.3). A control input u is used to regulate the position z_1 to a desired setpoint r.

3.3 Classical P(I)D control

Classical, linear, P(I)D control suffers from limitations when used to regulate a system subject to friction to a desired setpoint. First, the settling performance limitation for a PD-controlled system is illustrated. Second, the stability issues of a PID-controlled system, subject to friction containing a velocity-weakening Stribeck effect, are illustrated. Finally, the settling performance issues for a PID-controlled system subject to Coulomb friction are illustrated.

3.3.1 Linear PD control

Consider a linear PD controller for control input u in (3.1), to regulate the mass to a desired setpoint r. The PD controller is given by

$$u_{PD} = -k_p(z_1 - r) - k_d z_2, \tag{3.4}$$

where k_p and k_d represent the proportional and derivative gain, respectively. The closed-loop system can then be written as

$$\begin{aligned} \dot{z}_1 &= z_2, \\ \dot{z}_2 &\in \frac{1}{m}(-\Psi(z_2) - k_p(z_1 - r) - k_d z_2). \end{aligned} \tag{3.5}$$

The response of the closed-loop system (3.5) to a constant position reference, is simulated using a numerical time-stepping method [20]. This is an efficient method to correctly simulate systems with set-valued discontinuities in the right-hand side, in this case set-valued friction, without the need for event detection. Due to the apparent friction, the PD-controlled closed-loop system (3.5) reaches a non-zero steady state error within its equilibrium set, see Fig. 3.3. This equilibrium set is found by evaluating (3.5) at $\dot{z}_1 = \dot{z}_2 = 0$ and solving for z_1 and z_2, resulting in

$$\mathcal{E}_{PD} = \left\{ (z_1, z_2) \mid z_1 \in r + \frac{F_s}{k_p}\text{Sign}(0),\ z_2 = 0 \right\}. \tag{3.6}$$

The steady-state error can be reduced by increasing the proportional gain k_p, but cannot become zero.

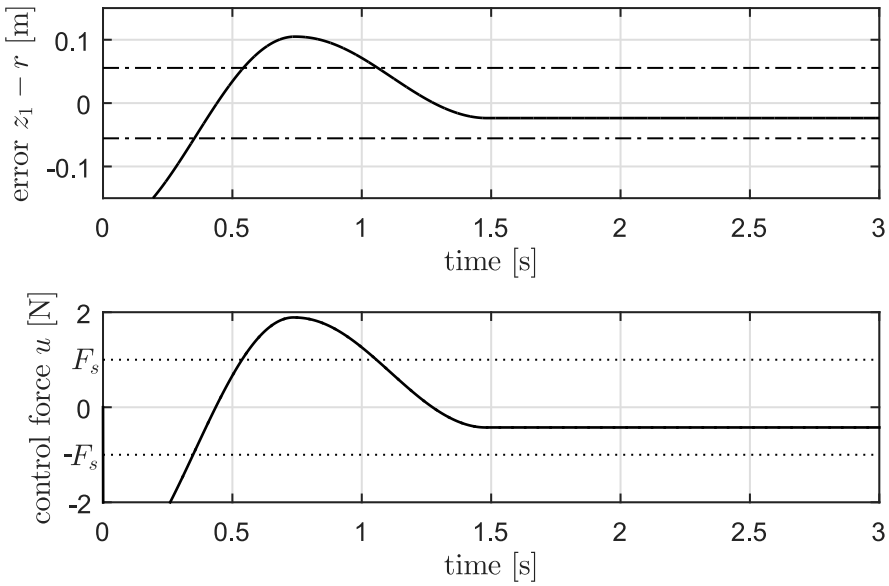

Fig. 3.3. Top: simulated position response (to $r = 0.2$) of a PD-controlled ($k_p = 18$, $k_d = 0.1$) single inertia ($m = 1$), subject to a friction characteristic Ψ including Stribeck effect. A non-zero steady state error occurs, within its stick-set (3.6) occurs (dash-dotted lines). Bottom: corresponding control force and static friction bounds (dotted lines).

3.3.2 Linear PID control

To correct for any steady-state error, a linear PID controller is implemented for control input u in (3.1), given by

$$u_{PID} = -k_p(z_1 - r) - k_d z_2 - k_i z_3, \tag{3.7}$$

where k_p, k_i, and k_d represent the proportional, integral, and derivative gain, respectively, and z_3 denotes the integrator state. The closed-loop system can then be written as

$$\begin{aligned} \dot{z}_1 &= z_2, \\ \dot{z}_2 &\in \frac{1}{m}(-\Psi(z_2) - k_p(z_1 - r) - k_d z_2 - k_i z_3), \\ \dot{z}_3 &= z_1 - r. \end{aligned} \tag{3.8}$$

The equilibrium set is again found by evaluating (3.8) at $\dot{z}_1 = \dot{z}_2 = \dot{z}_3 = 0$ and solving for z_1, z_2 and z_3, resulting in

$$\mathcal{E}_{PID} = \left\{ (z_1, z_2, z_3) \mid z_1 = r,\ z_2 = 0,\ z_3 \in \frac{F_s}{k_i}\mathrm{Sign}(0) \right\}. \tag{3.9}$$

The addition of an integrator allows the system to escape the stick phase, since it eventually compensates for the static friction. However, in the presence of a velocity-weakening Stribeck effect, the friction may be overcompensated in the slip phase, resulting in stick-slip oscilations around the setpoint [3, 21]. This is shown in simulation

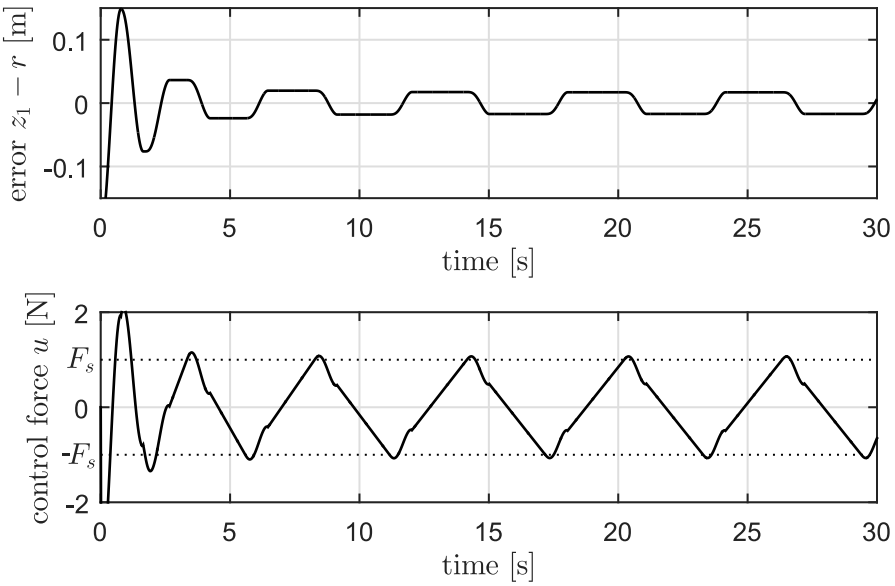

Fig. 3.4. Top: simulated position response (to $r = 0.2$) of a PID-controlled ($k_p = 18$, $k_d = 2.5$, $k_i = 40$) single inertia ($m = 1$), subject to a friction characteristic Ψ *including Stribeck effect*. A limit cycle around the desired setpoint occurs. Bottom: corresponding control force and static friction bounds (dotted lines).

in Fig. 3.4. This *stability* issue has been addressed in [22], where a control strategy is proposed that robustly compensates for this velocity-weakening Stribeck effect.

In the *absence* of a Stribeck effect, limit cycles do not occur for a single-mass system, and the setpoint r is asymptotically stabilized with a PID controller for input u in (3.1), see [23], as long as the following assumption is satisfied.

Assumption 1. *The controller gains k_p, k_d and k_i satisfy $k_i > 0$, $k_p > 0$ and $(k_p k_d)/m > k_i$.*

For the linear system, i.e., $F_s = 0$, Assumption 1 is equivalent to ensuring global exponential stability of the equilibrium $z_1 = r$, $z_2 = z_3 = 0$, by the Routh-Hurwitz stability criterion. However, this closed-loop system suffers from severe settling *performance issues*. PID control may suffer from slow convergence and therefore long settling times, due to the (increasingly) slow depletion and refilling of the integrator buffer (as the position response approaches the setpoint) [23]. When the system gets in stick, the integrator builds up the control force to overcome the static friction. When the static friction is overcome, the system slips and may overshoot its setpoint, after which it sticks again. Now the integrator buffer first has to deplete, before a control force in the opposite direction can be applied. Since the speed in which the integrator buffer is filled and depleted is proportional to the position error, this process takes increasingly more time with a decreasing position error, resulting in long settling times. This slow settling behaviour and increasingly slow filling and depleting of the integrator buffer is illustrated in simulation, in Fig. 3.5.

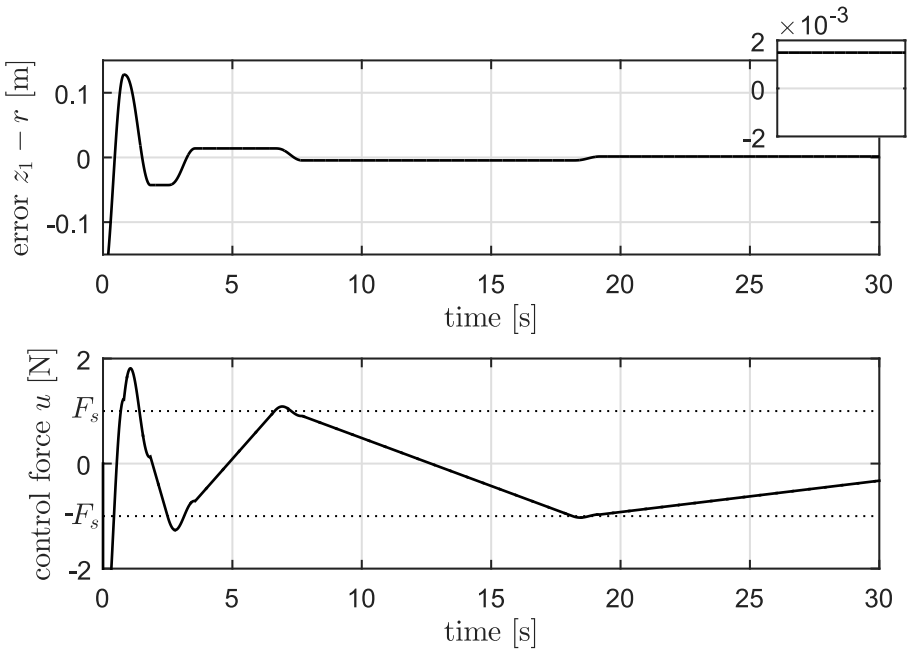

Fig. 3.5. Top: simulated position response for a PID-controlled system subject to Ψ *without Stribeck effect*, with $k_p = 18$, $k_d = 2.5$, $k_i = 40$. The system converges (increasingly) slow towards its setpoint. Bottom: corresponding control force and static friction bounds (dotted lines).

In context of the sample stage used in industrial electron microscopes, described in Section 1.1, long settling times result in significant usability limitations. This is especially the case in the semiconductor industry, where the microscope is used in parallel to the manufacturing process. The pace at which an image can be accurately created by the microscope is crucial to increase throughput and, consequently, reduce costs. In order to improve the settling response, without changing the actual system, non-linear control is investigated in the form of a reset PID controller.

3.4 Reset PID control

In order to improve the settling performance of a single-mass system subject to Coulomb friction, a reset PID controller is proposed in [1]. In this reset controller, the integrator term z_3 in the linear PID-controller, given in (3.8), is replaced by a reset integrator. Resetting the integrator circumvents to a large extend the filling and depletion of the integrator buffer, resulting in shorter periods of stick and thereby significantly faster

settling. The resulting reset PID controller is given by

$$u = -k_p(z_1 - r) - k_d z_2 - k_i z_3, \tag{3.10a}$$
$$\dot{z}_3 = z_1 - r, \tag{3.10b}$$
$$z_1^+ = z_1, \tag{3.10c}$$
$$z_2^+ = z_2, \tag{3.10d}$$
$$z_3^+ = -\alpha z_3 - (1+\alpha)\frac{k_p}{k_i}(z_1 - r). \tag{3.10e}$$

Here, the superscript + denotes the updated value of the state after a reset. The states z_1 and z_2 (the position and velocity, respectively) do not change after a reset, while the integrator state z_3 is updated according to (3.10e). The design parameter $\alpha \in [0,\, 1]$ enables scaling of the reset, to cope with asymmetry in the friction characteristic. Its role is further elaborated in Section 3.5.1. The integrator is reset according to (3.10e) whenever the following four conditions hold simultaneously:

1. The system overshoots the setpoint,

2. The system enters a stick phase,

3. The system has not yet settled within the desired accuracy band,

4. The controller output is larger than a specified value.

In a mathematical description of these four written reset conditions, the integrator is reset according to (3.10e) whenever $z = (z_1, z_2, z_3)$ is such that

$$\begin{aligned} &k_p(z_1 - r)^2 + k_i(z_1 - r)z_3 \leq 0 \\ \wedge\, &- z_2(k_p(z_1 - r) + k_i z_3) \leq 0 \\ \wedge\, &|-k_i(z_1 - r)| \geq \eta_1 \\ \wedge\, &|-k_p(z_1 - r) - k_i z_3| \geq \eta_2. \end{aligned} \tag{3.10f}$$

Here, the parameter η_1 defines a bound such that resets are inhibited when the carriage is within the desired position error accuracy band. The parameter η_2 causes resets to be inhibited when the controller output is small. These last two conditions in (3.10f) are required to ensure the absence of Zeno solutions [24]. The rationale behind the reset map (3.10e) and the reset conditions (3.10f) are clarified in Section 3.4.2.

An essential feature of these reset conditions is that, despite the discontinuity in the control force, the risk of exciting high-frequency system dynamics is not increased, compared to the application of the classical PID controller. This is the case because the system is always in stick when a reset occurs, and remains in stick right after the reset, due to the position-dependent term that is subtracted from the integrator sign change in (3.10e) (an essential feature to still ensure setpoint stability). Since the system is not moving, the *net* force acting on the system remains zero at a reset instant, i.e. the actuation force is fully counteracted by the friction force. The only time a discontinuity in the net force occurs is when the system enters the stick phase. This is, however, inherent to the discontinuous nature of the friction characteristic, and will therefore happen with both the classical PID controller and the reset controller.

For an elaborate analysis and a formal mathematical description of this reset controller, see [1].

3.4.1 Illustrative example

A numerical simulation to illustrate the achievable performance improvements when the reset PID controller in (3.10), is implemented, is shown in Fig. 3.6. A numerical time-stepping method is used to correctly deal with the set-valued friction [20].

First, consider the closed-loop system (3.8), where a classical PID controller is employed to control the mass to the constant position setpoint $r = 0$. For this simulation, $m = 1$ kg, $F_s = 1$ N, $F_v = 0.5$, and $k_p = 18$ N/m, $k_i = 40$ N/(ms) and $k_d = 2.5$ Ns/m. The

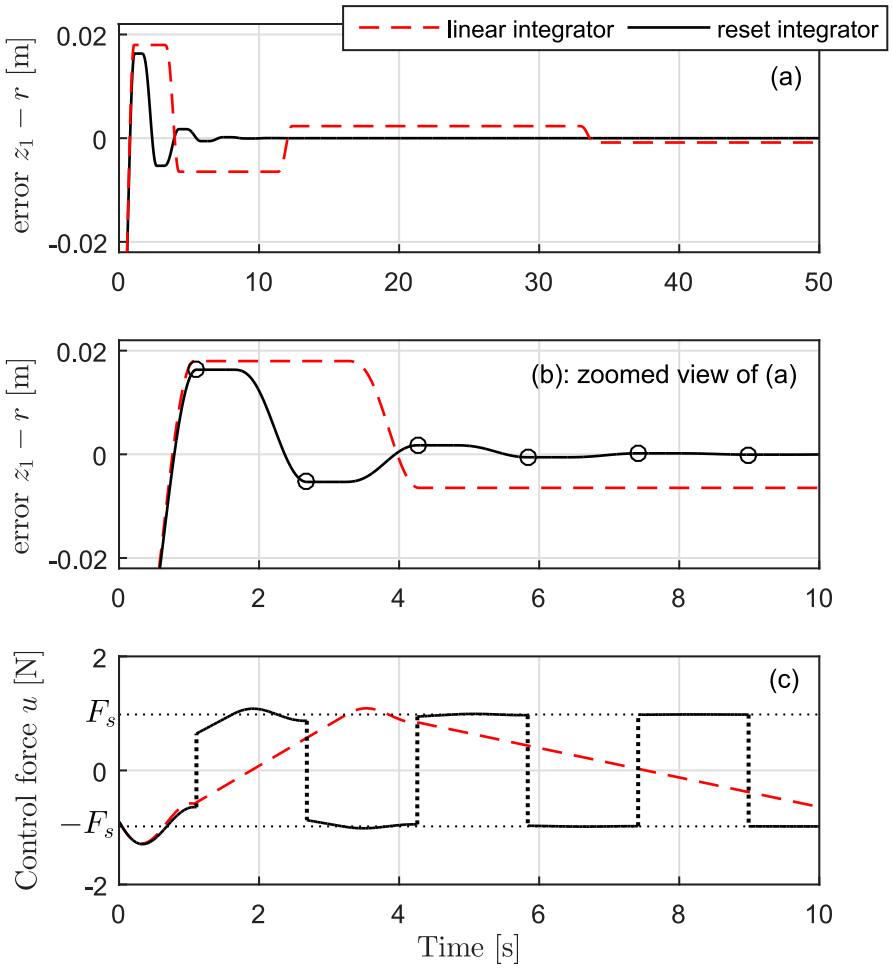

Fig. 3.6. Simulated position response with static and viscous friction (a), zoomed view (b) and control force with static friction bounds (dotted lines) (c). The circles indicate the instants of a controller reset.

controller gains satisfy Assumption 1. The position response is shown in Fig. 3.6a as the red dotted line. It can be seen that the system indeed converges to the constant setpoint $z_1 = 0$, however, long periods of stick result in a long settling time. The control force u for the linear PID controller is shown in Fig. 3.6c as the red dotted line, where the depletion and refilling process of the integrator buffer, causing long periods of stick, is clearly visible. This process takes increasingly more time with a decreasing position error, which results in increasingly longer periods of stick when the position error decreases.

To circumvent these (increasingly) long periods of stick, and increase settling performance, the linear PID controller is replaced by the reset controller, in (3.10), resulting in the closed-loop system (3.8), (3.10d)-(3.10f). The tuning parameters are $\alpha = 1$, $\eta_1 = 10^{-8}$, and $\eta_2 = 1$, resulting in the position response shown as the black line in Fig. 3.6. Here, the circles in Fig. 3.6b indicate the reset instants, which occur when the reset conditions are satisfied. It can be seen in Fig. 3.6c that due to the controller resets, a large part of the depletion/refilling process of the integrator buffer is circumvented, as the control force converges to the (unknown) value of $\pm F_s$ inbetween resets, resulting in a significant decrease of the settling time.

3.4.2 Hybrid system formulation

The closed-loop reset control system (3.8), (3.10d)-(3.10f) is written in the hybrid formalism of [24], to elaborate on the design of the reset conditions. First, the following state transformation is applied, which allows for a simpler description of the system dynamics, in terms of measurable states:

$$q := \begin{bmatrix} \zeta \\ \varphi \\ v \end{bmatrix} := \begin{bmatrix} m\sigma \\ m\phi \\ v \end{bmatrix} := \begin{bmatrix} -k_i(z_1 - r) \\ -k_p(z_1 - r) - k_i z_3 \\ z_2 \end{bmatrix}. \tag{3.11}$$

Here, ζ is the generalized position error, φ contains all non-zero components of the controller state at zero velocity, i.e. the proportional and integral terms and v is the velocity of the mass. The states σ and ϕ are added for completeness, since they are used in the stability analysis in [2]. The stick set can now be defined as

$$\mathcal{E}_{stick} = \left\{ q \in \mathbb{R}^3 \mid v = 0,\ |\varphi| \leq F_s \right\}. \tag{3.12}$$

With state transformation (3.11), the closed-loop dynamics (3.8) and reset law (3.10d) - (3.10e) are rewritten in the hybrid formalism of [24], as follows:

$$\begin{cases} \dot{q} \in \mathcal{F}(q) := \begin{bmatrix} -k_i v \\ \zeta - k_p v \\ \varphi - k_d v - F_s \text{Sign}(v) \end{bmatrix}, & q \in \mathcal{C}, \\ q^+ = g(q) := \begin{bmatrix} \zeta & -\alpha\varphi & v \end{bmatrix}^T, & q \in \mathcal{D}, \end{cases} \tag{3.13a}$$

where $\mathcal{F}$ is the flow map, g is the jump map, $\mathcal{C}$ is the flow set and $\mathcal{D}$ is jump set. Using (3.11), the reset conditions (3.10f) transform into the jump set

$$\mathcal{D} := \left\{ (\zeta, \varphi, v) \in \mathbb{R}^3 \mid \zeta\varphi \leq 0,\ \varphi v \leq 0,\ |\zeta| \geq \eta_1,\ |\varphi| \geq \eta_2 \right\}. \tag{3.13b}$$

Here the condition that the system overshoots its setpoint is given by $\zeta\varphi \leq 0$. To detect the stick phase, the criterion $\varphi v \leq 0$ is used rather then simply $v = 0$, since the latter is difficult to check (i.e., non-robust) in practice due to measurement noise.

The flow set contains all values for the state z, which are not contained by the jump set, and is given by

$$\mathcal{C} := \overline{\mathbb{R}^3 \setminus \mathcal{D}}. \tag{3.13c}$$

For an elaboration on the rationale behind the design of this jump set $\mathcal{D}$, consider Fig. 3.7, which shows the evolution of the states ζ, φ, and v, of the illustrative example in Section 3.4.1. Recall that the integrator is reset when the system satisfies the following two conditions at the same time: 1) it enters a stick phase, and 2) the position overshoots the setpoint, given as the jump set $\mathcal{D}$ in (3.13b), where ζ is the generalized *position error*, φ contains all nonzero components of the *controller state* at zero velocity, and v is the *velocity* of the mass.

1) Suppose the solution has initial condition $\zeta > 0$, $\varphi > 0$, and $v = 0$, and starts in a stick phase (time interval 1 in Fig. 3.7). Due to the dynamics of the integrator, $\varphi > F_s$ will eventually be reached, which results in a slip phase (intervals 2 and 3 in Fig. 3.7). The solution enters a stick phase again (interval 4 in Fig. 3.7) when $v = 0$ is reached and the controller state φ satisfies $0 < \varphi < F_s$. At this point, the condition $\varphi v \leq 0$ is satisfied.

A reset should not take place if the solution enters a stick phase *without* the occurrence of an overshoot, due to, e.g., different initial conditions, tuning, or friction characteristics. In such situations the solution still enters a stick phase and item 1) is satisfied. For this reason, we require the additional condition $\varphi\zeta \leq 0$ in the jump set $\mathcal{D}$ in (3.13b):

2) Before an overshoot of the setpoint (interval 2 in Fig. 3.7), we have positive ζ and φ, and thus $\varphi\zeta > 0$. After an overshoot (interval 3 in Fig. 3.7), ζ changes sign

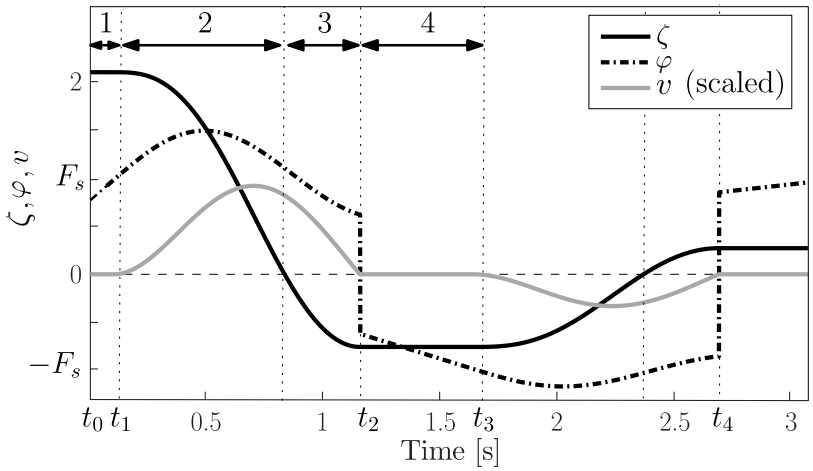

Fig. 3.7. The evolution of the states ζ, φ, and v, with the proposed reset PID controller. The integrator reset via a sign change of φ are clearly visible. This figure is adapted from [2].

so that $\varphi\zeta \leq 0$. Along with item 1), we conclude that the requirement $\varphi\zeta \leq 0$ in $\mathcal{D}$ indeed enforces that a reset only takes place when the solution enters a stick phase *after* an overshoot.

Finally, the conditions $|\zeta| \geq \eta_1$ and $|\varphi| \geq \eta_2$ in (3.13b), for some design parameters $\eta_1 > 0$ and $\eta_2 > 0$, prevent a jump when ζ or φ are zero, so that Zeno behavior is avoided. A formal proof is given in [2], that under Assumption 1, the set of equilibria

$$\mathcal{B} = \left\{ z \in \mathbb{R}^3 \mid \zeta = v = 0,\ |\varphi| \leq \frac{F_s}{m} \right\} \tag{3.14}$$

is asymptotically stable, which means that the system converges asymptotically towards the setpoint. In the next section, the reset PID controller is implemented on the experimental setup.

3.5 Controller validation on the experimental setup

The PID reset controller is implemented on the nano-positioning experimental setup, described in Section 2.1, to investigate the achievable performance benefits in practice. The goal is to control the system towards a desired setpoint within an accuracy of 10 nm. To achieve this, the setup follows a fourth-order reference trajectory to its setpoint, such that is moves with a velocity of 1 mm/s. At the end of this initial transient trajectory, the stage has a non-zero positioning error due to the presence of friction. This is the starting point of the window of interest, and from this point on, the goal is to control the system towards a specified position error accuracy of 10 nm using the proposed PID reset controller. The following experimental results are submitted for journal publication in [2].

The system identification study in Section 2.3, shows that the nano-positioning stage can be approximated by a single-mass model up to 160 Hz, and friction experiments from Section 2.5 show that a Stribeck effect is present in the experimental setup. Despite the small Stribeck effect, the experimental results below show that both the classical and the reset PID controller have some robustness against a Stribeck effect. The controller tuning, settling performance benefits, the effect of microscopic frictional effects, and repeatability are discussed below.

3.5.1 Controller tuning

The PID controller gains are obtained using standard linear loop-shaping techniques, based on the parametric system model found in section 2.6, resulting in $k_p = 10^7$ N/m, $k_d = 2 \cdot 10^3$ Ns/m and $k_i = 10^8$ N/(ms). For these controller parameter values, Assumption 1 holds. The standard robustness margins (for linear controller design) are met, see Appendix C.

The reset controller requires tuning of three additional parameters: α, η_1 and η_2. The tuning parameter $\alpha \in [0,\ 1]$ determines to which value the integrator state resets. For $\alpha = 0$, the integrator state resets to 0. An α closer to 1 results in a larger reset and a

correspondingly shorter stick duration, where an α closer to zero increases robustness for frictional asymmetry. A milder reset allows for increasing levels of asymmetry in static friction, since this prevents overcompensation of friction and maintains its stabilizing properties, see [1] for more details. Experiments are done using various values for α, showing the direct influence of this parameter on the settling performance.

The parameter $\eta_1 = k_i \cdot 10^{-8} = 1$ N/s is chosen, such that resets are inhibited when the carriage is within the desired position error-accuracy band of 10^{-8} m (10 nm). The parameter $\eta_2 = 1$ Nms is chosen to avoid Zeno behaviour, and is experimentally obtained.

3.5.2 Settling performance benefits

The performance benefits of the reset controller with respect to the classical PID controller, on the experimental setup, are demonstrated in Fig. 3.8. In particular, the relative improvement in terms of settling time, compared to classical PID control is shown.

The responses for the position error $z_1 - r$ and the corresponding scaled control force $u/(4k_i)$ are presented in Fig. 3.8 for the classical PID and the reset PID (with different values of α). All experiments are performed with the same initial conditions. Variations in the position errors and time instants of the initial stick phases between the presented responses are due to the fact that the friction characteristic is slightly different for each experiment, due to, e.g., small temperature changes as a result of continued system operation. Since the setup operates on a nano-scale, even minor changes in the friction may have a significant impact on the response. It can be observed in Fig. 3.8 that the application of the reset controller (see the four bottom plots for different values for α) results in generally shorter stick periods and hence decreased settling times, as compared to the classical PID controller (see the top plot). In particular, in the presented responses, the desired accuracy is achieved at respectively, 95, 72, 25 and 8 seconds corresponding to values for α of 0, 0.3, 0.8 and 1. In contrast to the reset controller, the classical PID controller (with the same controller gains), did not reach the desired accuracy within the maximal measurement window of 120 seconds.

Finally, it is emphasized that false resets are not triggered due to the robust design of the jump set $\mathcal{D}$ in (3.13b), with respect to velocity measurement noise, as pointed out in Section 3.4.2.

3.5.3 Microscopic frictional effects

Microscopic frictional effects play a non-negligible role on the considered setup, due to the low positional error levels the setup operates in. These microscopic frictional effects, discussed in Section 2.5, can clearly be observed as the small stick-to-stick jumps in the position error response upon resets, see the inset in the fourth subplot of Fig. 3.8. Macroscopically, the system *should* not move upon reset, as is claimed in Section 3.4, since the actuation force to which the controller resets, is always smaller then the static friction. However, due to a finite stiffness of the asperities, microscopic

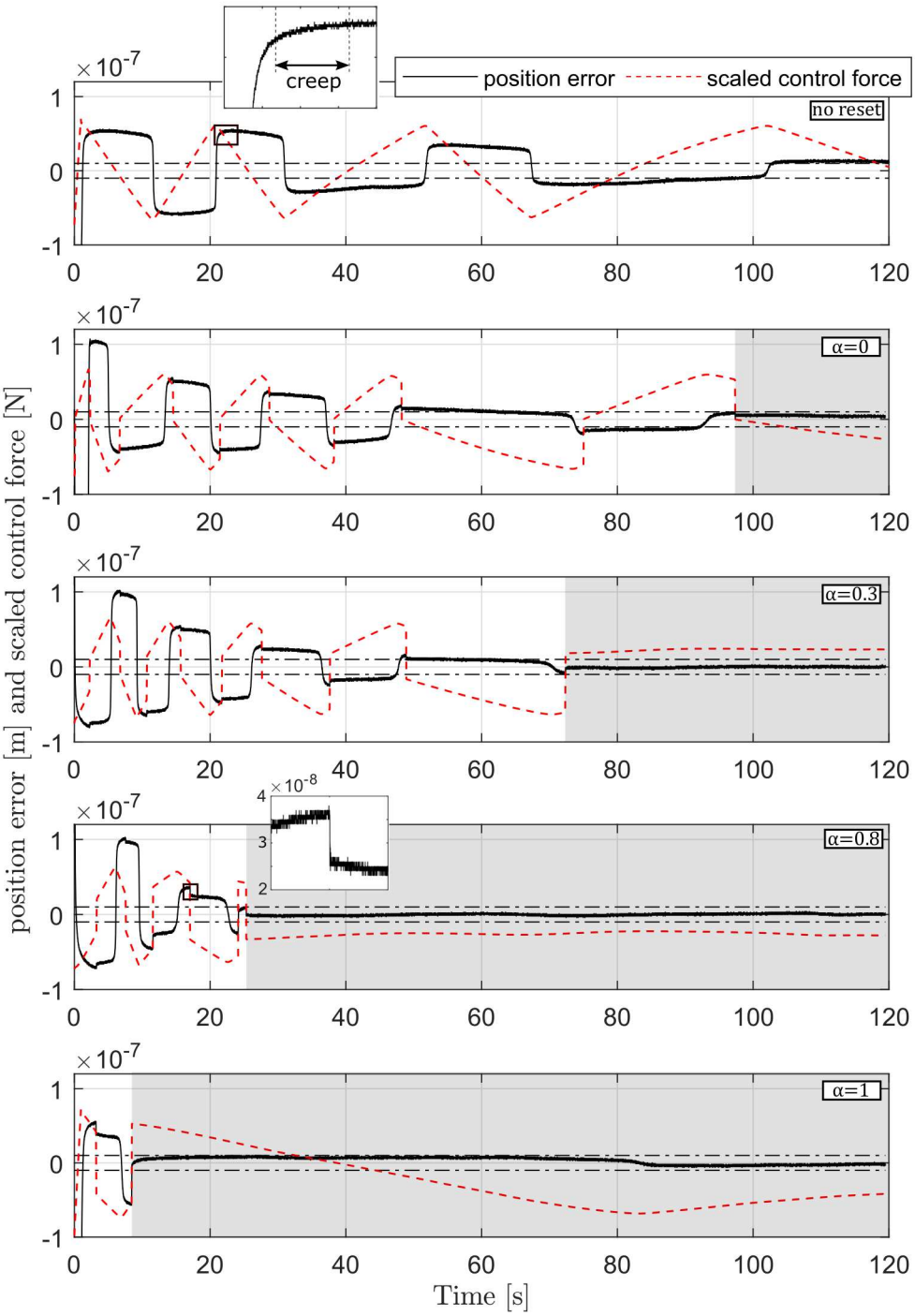

Fig. 3.8. Experimental results of various values of α. Black: position error $z_1 - r$; red: total control force scaled by $4k_i$. The accuracy band of 10 nm is indicated by the dashed lines. The gray patches indicate when the system has settled within its accuracy band of 10 nm.

stick-to-stick jumps can be observed. The measured stiffness of the asperities have values between $8 \cdot 10^8$ and $7 \cdot 10^9$ N/m, determined by dividing the change in force by the resulting microscopic displacement. Although these estimated stiffness coefficients are very large, the associated effect is significant due to the low position errors in the operating conditions. In this case, these microscopic elastic effects are not unfavourable, as they force the system towards the setpoint. Microscopic stiffness effects can, however, also have a negative contribution to the settling response. When the stiffness of the asperities is low, or the size of the reset is large, the positional jump will be large, which may result in the system overshooting its setpoint. A new reset occurs almost immediately after, since the reset conditions in $\mathcal{D}$ are again satisfied. These consecutive resets due to large positional jumps, which are a result of large resets for $\alpha = 0.75$, are shown in Fig. 3.9, resulting in a deterioration of the settling performance.

A second effect that affects the settling performance is microscopic creep. As compared to the response in the example of Section 3.4.1, a controller reset occurs some time after the beginning of a macroscopic stick instant, instead of at the beginning of the stick instant. This effect is caused by microscopic creep, first mentioned in Section 3.5.3, at the start of (and during) a macroscopic stick instant (see the first inset in the first subplot of Fig. 3.8), thereby not allowing for a discrete jump because of the nonzero velocity. Hitting $v = 0$ (so that $\phi v \leq 0$ in $\mathcal{D}$ is satisfied) can be detected only when the microscopic creep stops. The reset delay associated to creep allows then the integrator buffer to deplete, which, in turn causes a milder reset. This milder reset decreases the achievable performance benefits, but increases the robustness against asymmetry in the friction characteristics, mentioned in Section 3.5.1.

3.5.4 Repeatability

On this nano-scale, slight variations in the friction characteristic, or in the initial conditions, have a significant influence on the settling response. This is demonstrated by performing 8 repeated settling experiments to a step reference of 10^{-6} m, with a minimal variation in initial conditions (carriage position within $1 \cdot 10^{-6}$ m, spindle orientation within $(2\pi)/100$ rad), shown in Fig. 3.9. The blue line represents the measured system response of the experiment with the smallest settling time, whereas the grey lines show the response of the other experiments.

The top plot, where a classical, linear PID controller is used, displays significant variation in the settling response. The duration of the first moment of stick is proportional to the size of the initial overshoot, since the position error determines the time it takes for the integrator to compensate for the static friction. Despite the long initial moment of stick, however, a small initial overshoot is beneficial for the settling response, which makes sense intuitively. Furthermore, one response seems to exhibit a limit cycle, instead of converging to the setpoint, which is either a result of the (slight) Stribeck effect, or due to the mechanical flexibility in the system. Limit cycles in flexible, 4th-order system, are investigated in Chapter 4.

The bottom plots in Fig. 3.9 show the settling response of the experimental setup when the reset controller is implemented, for increasing values of α. The first three plots, for $\alpha = 0$, $\alpha = 0.25$ and $\alpha = 0.5$, respectively, show relatively repeatable behaviour. The

variation in initial overshoot is similar to the linear PID case, since both controllers are identical up to the first moment of stick. The settling time is, *generally*, decreased significantly, compared to the linear PID controller, where the largest α results in the shortest settling time. Limit cycles are now avoided for all measurements. This may suggest that, although not specifically considered during the design, the implemented reset controller also has a stabilizing functionality in the case of friction-induced limit cycles. For $\alpha = 0.75$, however, robustness issues can be observed, in the form of large variations in settling performance. Here, the system either converges quickly, or shows oscillatory behaviour, which is a result of microscopic elastic jumps upon reset, which significantly overshoot the setpoint, due to the microscopic friction effects discussed in Section 2.5.

The elastic jumps upon reset are shown in a zoomed-in plot in Fig. 3.10, for $\alpha = 0$, $\alpha = 0.25$ and $\alpha = 0.75$. It can be clearly observed that the *size* of the elastic jump is *generally* related to the size of the reset. There is no clear linear relation between the size of the reset and the size of the elastic jump, however, since the jump-size is position-dependent. The *moment* on which the first reset occurs does not depend on α, but instead varies due to slight variations in initial conditions, or friction characteristics.

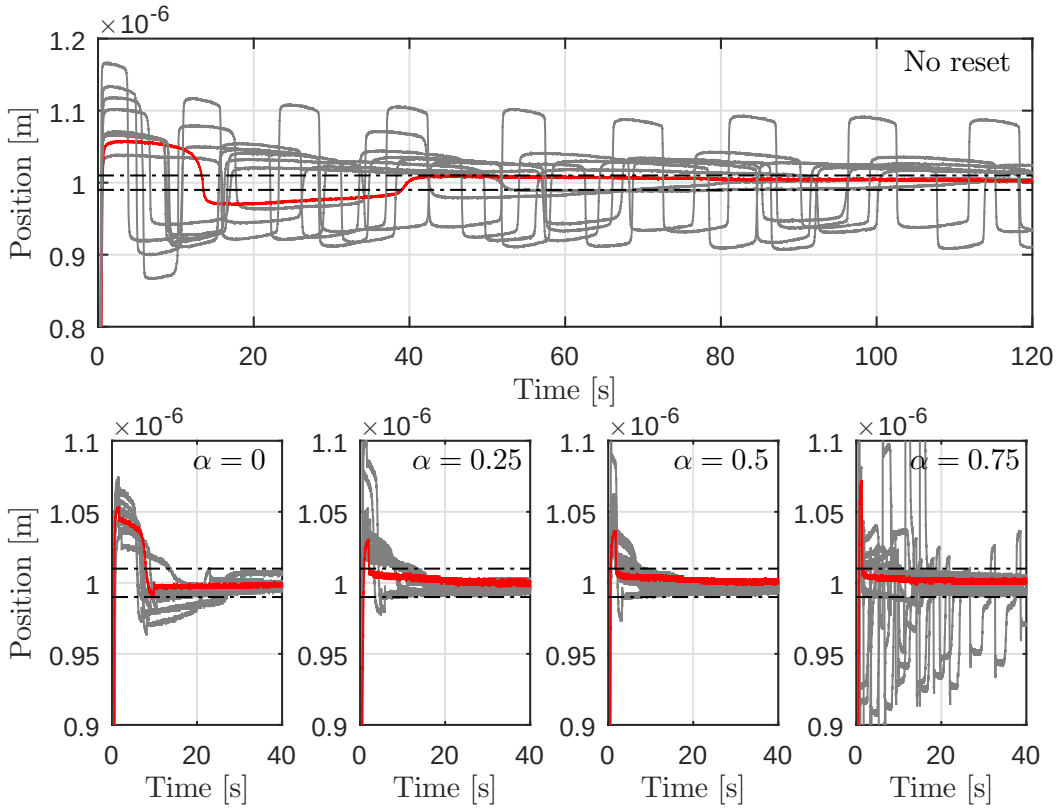

Fig. 3.9. Comparison of multiple, independent measurements of the settling response to a step reference of $1 \cdot 10^{-6}$ m. Grey: measured settling response of each individual experiment, red: measured system response of the experiment with the smallest settling time, black: accuracy bound of 10 nm.

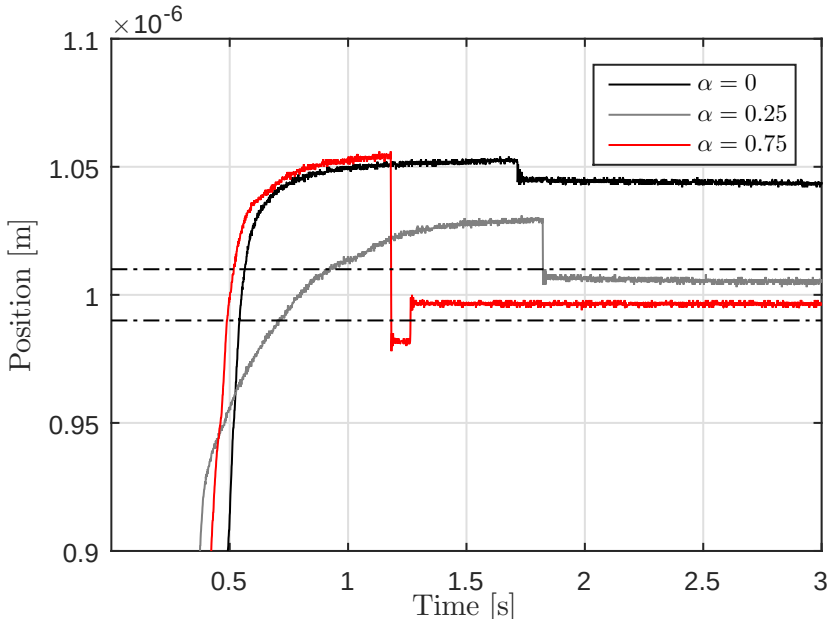

Fig. 3.10. Zoomed-in plot, showing the elastic jumps upon reset for $\alpha = 0$ (black), $\alpha = 0.25$ (grey) and $\alpha = 0.75$ (red).

3.6 Discussion

In this chapter, the PID reset controller proposed in [1] is discussed and implemented on the nano-positioning experimental setup, described in Section 2.1. The experimental results show significant performance improvement in terms of settling time, when employing the proposed reset PID controller, as compared to its classical PID counterpart. Increasing the scaling factor α, and consequently the size of the reset, generally increases the performance in terms of settling time.

However, microscopic frictional effects play a non-negligible role on the considered setup, due to the low positional error levels the setup operates in. Firstly, these effects result in microscopic elastic stick-to-stick jumps upon an integrator reset. Larger controller resets result in larger elastic microscopic jumps, which may induce oscillatory behaviour around the setpoint, thereby limiting the size of the reset. Secondly, microscopic creep results in a delayed controller reset, as compared to a simulated response. This is because the microscopic creep results in a non-zero velocity, thereby inhibiting a controller reset.

On this nano-scale, slight variations in the friction characteristic, or in the initial conditions, have a significant influence on the settling response. For certain initial conditions, robustness issues can be observed when applying larger resets. It is therefore emphasized that the experimental results show the *potential* improvement in settling performance when the reset PID controller is employed, but these improvements are not guaranteed for all initial conditions. Applying a lower scaling factor α increases the robustness against frictional uncertainties, but at the cost of longer settling times. Improving the mechanical design of the experimental setup, by decreasing the machin-

ing tolerances of the sliding surfaces (e.g., smooth the spindle-nut contact, which is the dominant friction source), can reduce the position-dependency of the frictional effects. This can result in repeatable settling behaviour, for different initial conditions, which would allow for a more general application (i.e., independent of initial conditions) of the proposed reset controller.

CHAPTER 4

Setpoint control of flexible motion systems

This chapter expands the setpoint control problem from a 1 DOF case, to a flexible 2-mass-spring-damper system subject to non-collocation of friction and actuation. Adding this additional DOF to the model enables the modeling of (anti-)resonances and the notion of (non-)collocation of, e.g., sensing and actuation or actuation and friction, which are often essential for accurate system modeling and controller design. The model for this system is given in Lur'e-type form, after which an illustrative simulation example is used to identify the control problems regarding stability and settling performance. These control problems are analysed through a simulation-based bifurcation analysis and a more general Linear Matrix Inequality (LMI) approach. Subsequently, two control strategies for setpoint control are proposed, which address these stability- and performance issues.

4.1 Introduction

Consider a 2-mass-spring-damper system as depicted in Fig. 4.1, given by the EOM

$$\begin{cases} m_1\ddot{x}_1 = u + k(x_2 - x_1) + d(\dot{x}_2 - \dot{x}_1), \\ m_2\ddot{x}_2 = -k(x_2 - x_1) - d(\dot{x}_2 - \dot{x}_1) - \Psi. \end{cases} \tag{4.1}$$

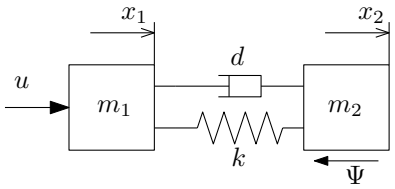

Fig. 4.1. Model of a general 2-mass-spring-damper system with non-collocation of friction and actuation.

Here, x_1 and x_2 are the position of the first and the second mass, respectively, $\dot{x}_1$ and $\dot{x}_2$ are the velocities of the first and the second mass, respectively, $\ddot{x}_1$ and $\ddot{x}_2$ are the accelerations of the first and the second mass, respectively, and m_1 and m_2 are the masses of the first and second mass, respectively. The two masses are connected via a flexible link with stiffness k and damping d. The friction force Ψ, acting on the second mass, is induced by a Coulomb friction model with static friction F_s, see Fig. 4.2, and is given by

$$\Psi \in F_s \text{Sign}(\dot{x}_2), \tag{4.2}$$

where the set-valued Sign$(\cdot)$ function is given in (2.3). The control goal is to regulate the second mass to a desired position ($x_2 = r$), by applying a control input u to the first mass. A linear P(I)D controller is employed for this regulatory task, given by

$$\begin{aligned} u &= K_c\bigg((r - x_2) - T_d\dot{x}_2 - \frac{1}{T_i}\xi\bigg), \\ \xi &= \int_0^\tau (r(\tau) - x_2(\tau))d\tau, \end{aligned} \tag{4.3}$$

where r is the reference position, and ξ is the integrator state. The controller parameters T_i and T_d represent the integrator- and derivative time constant, respectively, and K_c is the overall gain.

This 2 DOF model can represent a wide range of (motion) systems, e.g., flexible servo systems, robots or nano-positioning motion stages, see, e.g., Section 2.2. Adding this additional DOF to the model increases its usability significantly, as it enables the modelling of (anti-)resonances and the notion of (non-)collocation of, e.g., sensing and actuation or actuation and friction. Both these phenomena are often essential for accurate system modelling and controller design. In this chapter, modelling and setpoint control of such a 2 DOF system is investigated. To this end, the system dynamics is

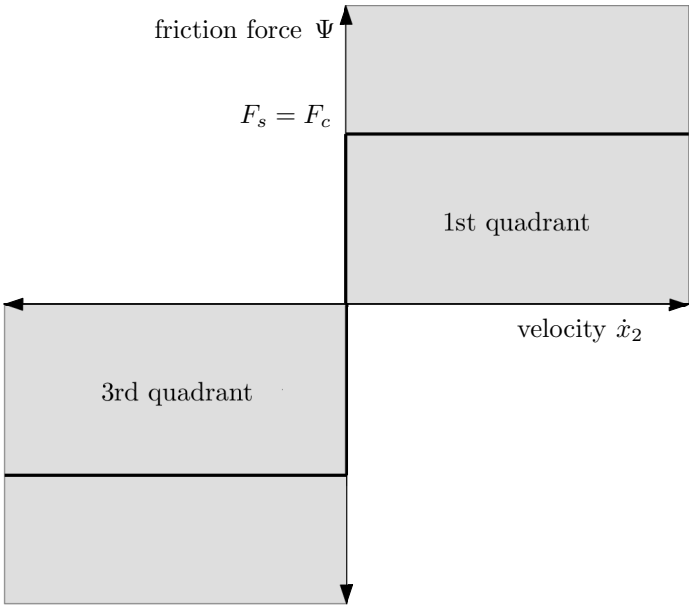

Fig. 4.2. Coulomb friction characteristic.

first modelled as a Lur'e-type system in Section 4.2. The control issues associated with P(I)D control of 2 DOF systems subject to non-collocated friction are illustrated in Section 4.3. The identified control issues are investigated through a simulation-based bifurcation analysis in Section 4.4, after which two LMI-based stability analysis tools are presented in Section 4.5. Finally, two control strategies to deal with the identified control issues are presented in Section 4.6.

4.2 Lur'e-type model

The system in Fig. 4.1, described by the dynamics (4.1), can be represented as a Lur'e-type system [25]. This class of systems consists of a linear time invariant (LTI) part, where a (set-valued) nonlinearity is added through a feedback loop. The Lur'e-type system is described by the following differential inclusion (see Fig. 4.3a).

$$\begin{aligned} \dot{x} &= Ax + Bu + Hw, \\ y &= Cx, \\ w &\in -\Psi(y), \end{aligned} \tag{4.4}$$

where x is the system state, y is both the input of the set-valued friction function $\Psi(y)$ and the system output, and u is the control input. The set-valued friction law Ψ satisfies a $[0, \infty]$ sector condition, which means the friction characteristic is bounded within the first and third quadrant of the Ψ-$\dot{x}_2$-plane in Fig. 4.2. The friction characteristic only consists of Coulomb friction, i.e., no Stribeck effect. The linear state-feedback control law is written as

$$u = Kx, \tag{4.5}$$

where K is the controller gain matrix representing the P(I)D controller given in (4.3). Substituting (4.5) in (4.4) gives the following closed-loop system, described by the differential inclusion (see Fig. 4.3b):

$$\begin{aligned} \dot{x} &= (A + BK)x + Hw, \\ y &= Cx, \\ w &\in -\Psi(y). \end{aligned} \tag{4.6}$$

The transfer function $G(s)$ of the linear part of (4.6) from the input w to the output y is given by

$$G(s) = C(sI - (A + BK))^{-1}H. \tag{4.7}$$

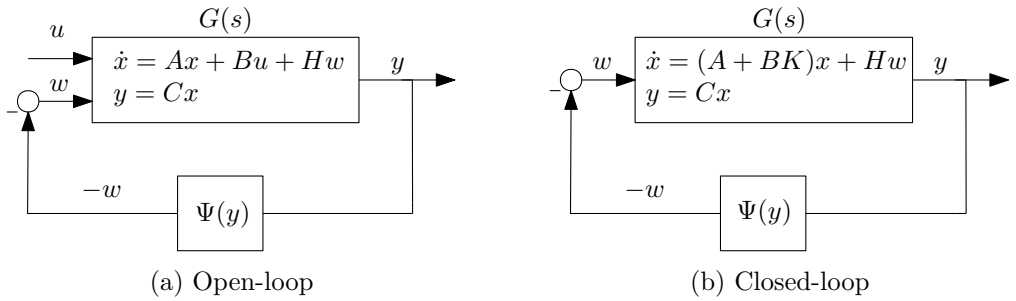

(a) Open-loop (b) Closed-loop

Fig. 4.3. Lur'e representation of the open-loop and closed-loop system.

The matrices A, B, C, H and K in (4.6) for both PD- and PID-control are given below.

PD control

For PD control, the state vector x in (4.6) is defined as: $x_{PD} = \begin{bmatrix} x_1 & x_2 & \dot{x}_1 & \dot{x}_2 \end{bmatrix}^T$. The system matrices in (4.6) and feedback gain matrix K in (4.5) are given by:

$$A_{PD} = \begin{bmatrix} 0 & 0 & 1 & 0 \\ 0 & 0 & 0 & 1 \\ -\frac{k}{m_1} & \frac{k}{m_1} & -\frac{d}{m_1} & \frac{d}{m_1} \\ \frac{k}{m_2} & -\frac{k}{m_2} & \frac{d}{m_2} & -\frac{d}{m_2} \end{bmatrix}, \quad B_{PD} = \begin{bmatrix} 0 \\ 0 \\ -\frac{1}{m_1} \\ 0 \end{bmatrix}, \tag{4.8a}$$

$$C_{PD} = \begin{bmatrix} 0 & 0 & 0 & 1 \end{bmatrix}, \qquad H_{PD} = \begin{bmatrix} 0 \\ 0 \\ 0 \\ \frac{1}{m_2} \end{bmatrix}, \tag{4.8b}$$

$$K_{PD} = \begin{bmatrix} 0 & K_c & 0 & T_d K_c \end{bmatrix}. \tag{4.8c}$$

PID control

For PID control, the state vector x in (4.6) is defined as: $x_{PID} = \begin{bmatrix} x_1 & x_2 & \dot{x}_1 & \dot{x}_2 & \xi \end{bmatrix}^T$. The system matrices in (4.6) and feedback gain matrix K in (4.5) are given by:

$$A_{PID} = \begin{bmatrix} 0 & 0 & 1 & 0 & 0 \\ 0 & 0 & 0 & 1 & 0 \\ -\frac{k}{m_1} & \frac{k}{m_1} & -\frac{d}{m_1} & \frac{d}{m_1} & 0 \\ \frac{k}{m_2} & -\frac{k}{m_2} & \frac{d}{m_2} & -\frac{d}{m_2} & 0 \\ 0 & 1 & 0 & 0 & 0 \end{bmatrix}, \quad B_{PID} = \begin{bmatrix} 0 \\ 0 \\ -\frac{1}{m_1} \\ 0 \\ 0 \end{bmatrix}, \tag{4.9a}$$

$$C_{PID} = \begin{bmatrix} 0 & 0 & 0 & 1 & 0 \end{bmatrix}, \qquad H_{PID} = \begin{bmatrix} 0 \\ 0 \\ 0 \\ \frac{1}{m_2} \\ 0 \end{bmatrix}, \tag{4.9b}$$

$$K_{PID} = \begin{bmatrix} 0 & K_c & 0 & T_d K_c & T_i K_c \end{bmatrix}. \tag{4.9c}$$

In the following section, the PD- and PID controlled systems given above are used to illustrate the stability- and performance issues related to setpoint control of flexible systems subject to friction.

4.3 Illustrative example

The issues regarding stability and settling performance of a closed-loop, flexible, 2 DOF system, subject to set-valued friction, as given in (4.6), are demonstrated in an illustrative simulation example. The parameters used for these simulations are given in Table 4.1 and 4.2. Here, the controller integrator- and derivative time constant are fixed, resulting in a single controller design variable K_c, see (4.3). In terms of a practical application, this situation and parameter choice can represent a well-mounted and lubricated motor with negligible friction and high equivalent mass, driving a load with low mass, subject to friction.

The position response of the closed-loop system (4.6), with parameter values given in Table 4.1 and 4.2, to a step reference of $5 \cdot 10^{-4}$ m, is simulated and depicted in Fig. 4.4. The first plot shows the position response of the PD-controlled system without friction, with $K_c = 8000$. This PD-controller stabilizes the linear closed-loop system and converges to the desired setpoint. In the second plot, non-collocated friction (at the second inertia) is added to the *same* PD-controlled system, resulting in limit cycling. In contrast to the 1 DOF case in Section 3.3, a limit cycle occurs *without* the presence of a Stribeck effect, and *without* integral action. The controller gain K_c is reduced to $K_c = 4000$, resulting in the disappearance of the limit cycle, shown in the third plot. However, the system settles at a steady-state error due to the presence of friction and the absence of integral action, similar to the 1 DOF case in Section 3.3.1. Therefore, an integrator is added to escape the stick phase, but doing so results in the re-occurrence of limit cycles, shown in the fourth plot. This limit cycle can be attenuated again by decreasing the gain K_c even further, shown in the last plot of Fig. 4.4.

As can be seen from the oscillations of the position response in the top plot of Fig. 4.4, the robustness margins are low. The reason this example is used, is that the bifurcation plots in Fig. 4.5 and 4.6 are created using these system values, enabling direct comparison between this illustrative example and these two figures. Examples have been found, however, in which a system with standard robustness margins also displayed the same limit cycling behaviour.

Table 4.1: System parameters.

Parameter	**Value 1**	**Unit**
m_1	1	[kg]
m_2	0.1	[kg]
k	1000	$[\mathrm{N\,m^{-1}}]$
d	10	$[\mathrm{N\,s\,m^{-1}}]$
F_s	0.5	[N]

Table 4.2: Controller parameters.

Parameter	**Value 1**
T_d	0.02
T_i	1/15

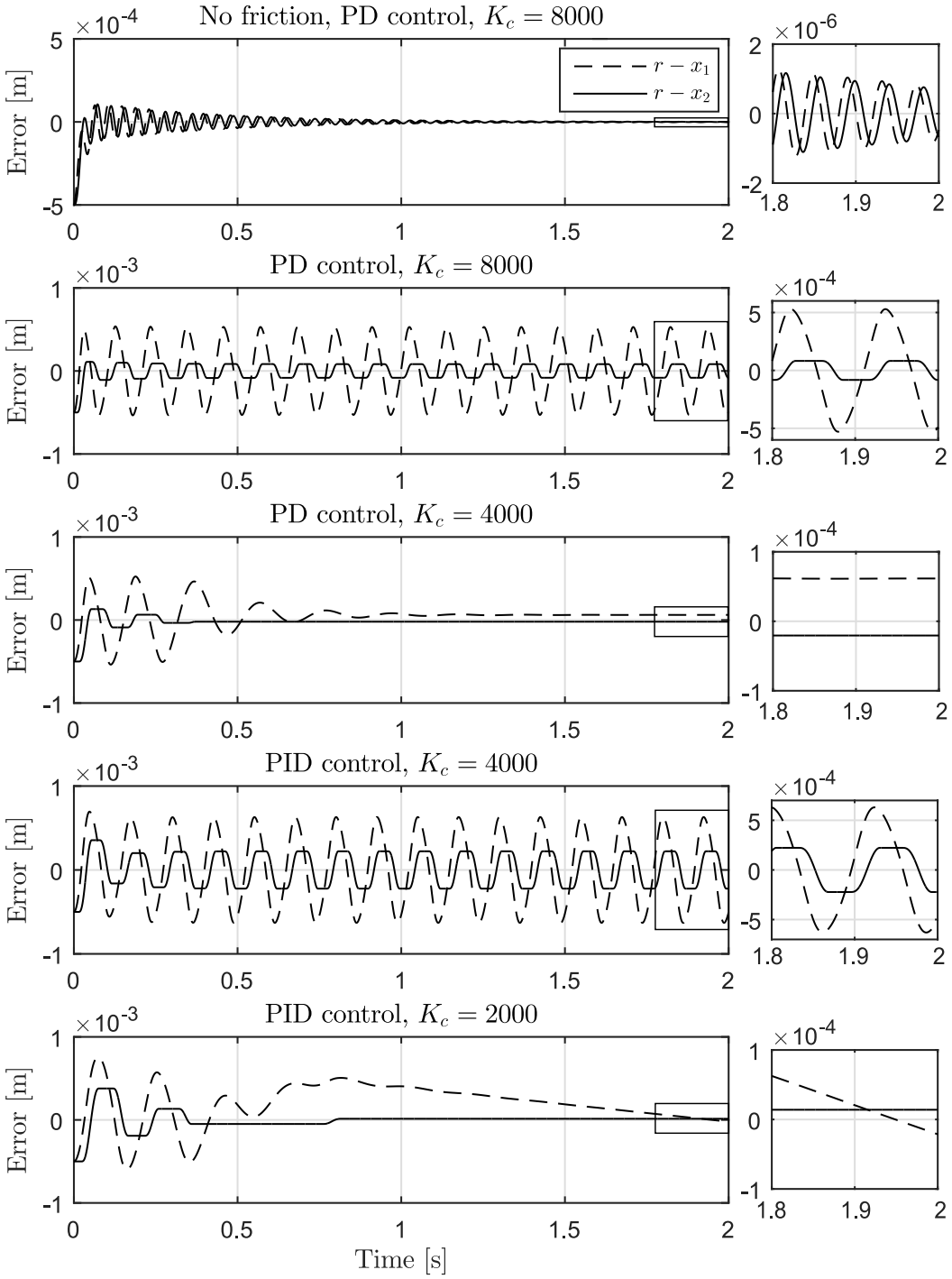

Fig. 4.4. Illustrative example showing the possibility of limit cycles, depending on the controller gain K_c.

The main observation from this illustrative example is that a P(I)D-controlled, flexible, 2-mass-spring-damper system with non-collocated Coulomb friction *can* exhibit limit cycling, without a Stribeck effect in the friction. This is an essential difference between a 1 DOF and a 2 (or multiple) DOF system. For P(I)D-controlled 1 DOF systems, limit cycles are only possible when $F_s > F_c$, i.e., the static friction is larger then the Coulomb friction, e.g., when the friction characteristic contains a Stribeck effect (see Fig. 3.2). For P(I)D controlled 2 DOF systems with flexible dynamics, this is not the case, since limit cycles may occur even when only Coulomb friction is present, i.e., $F_s = F_c$. This has previously been concluded in [26] for friction acting solely on the motor side, but not for non-collocation of friction and actuation, as the above simulations indicate.

4.4 Simulation-based bifurcation analysis

The illustrative example in Section 4.3 shows that in some cases, a flexible system subject to non-collocated Coulomb friction exhibits limit cycling, even without an integrator. In this section, the limit cycling behaviour is investigated through a simulation-based bifurcation analysis. In particular, the goal is to find the controller gains K_c for which the closed-loop system (4.6) does not exhibit limit cycling.

The equilibrium set of the closed-loop system is found by evaluating (4.6) at $\dot{x}_1 = \ddot{x}_1 = \dot{x}_2 = \ddot{x}_2 = 0$, and, additionally, $\dot{\xi} = 0$ for the integral case, and algebraically solve for x_1 and x_2. This results in the following two equilibrium sets, for a PD-controlled or PID-controlled closed-loop system respectively:

$$\begin{aligned}\mathcal{E}_{PD} = \Big\{ &(x_{PD} \in \mathbb{R}^4) \mid \\ &\dot{x}_1 = \dot{x}_2 = 0, x_1 \in \left[\tfrac{k-K_c}{K_c k} F_s \quad \tfrac{k-K_c}{K_c k} F_s\right], x_2 \in \left[-\tfrac{1}{K_c} F_s \quad \tfrac{1}{K_c} F_s\right] \Big\},\end{aligned} \tag{4.10}$$

$$\begin{aligned}\mathcal{E}_{PID} = \Big\{ &(x_{PID} \in \mathbb{R}^5) \mid \\ &\dot{x}_1 = \dot{x}_2 = 0, x_1 \in \left[-\tfrac{F_s}{k} \quad \tfrac{F_s}{k}\right], x_2 = 0, \xi \in \left[-\tfrac{F_s}{K_c T_i} \quad \tfrac{F_s}{K_c T_i}\right] \Big\}.\end{aligned} \tag{4.11}$$

Now it is of interest to find all controller gains K_c that stabilize the *linear* part of the closed-loop system, i.e., without friction[1]. The equilibrium of a linear system is asymptotically stable if all the roots of the characteristic polynomial lie in the open left-half of the complex plane. The Routh-Hurwitz stability criterion is used to determine the number of closed-loop poles in the right-half complex plane. Applying the Routh-Hurwitz stability condition to the example system results in the following sets of controller gains K_c that stabilizes the linear part of a PD- and PID-controlled system respectively:

$$\mathcal{A}_{PD} = \{K_c \in \mathbb{R}_{>0} \mid 1 < K_c < 10084\} \tag{4.12}$$

$$\mathcal{A}_{PID} = \{K_c \in \mathbb{R}_{>0} \mid 798 < K_c < 9917\} \tag{4.13}$$

[1]Only the set of controller gains that stabilize the linear part of the system are investigated. Simulations have shown that adding friction actually increases this stability range, but designing a controller which does not stabilize the linear plant is not recommended and hardly ever done in practice.

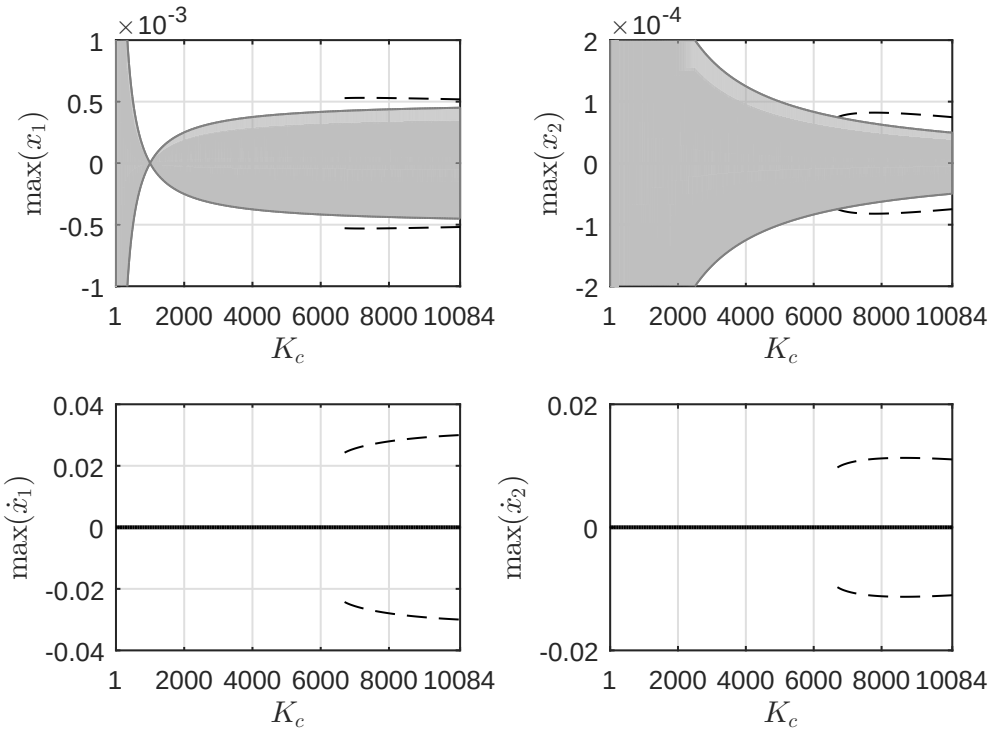

Fig. 4.5. Bifurcation plots of the PD-controlled system. The maximum value of the states (x_1, x_2, $\dot{x}_1$, $\dot{x}_2$) are plotted against the controller gain K_c. The dotted lines represent limit cycles, the thick lines represent equilibrium points and the grey areas represent an equilibrium set.

Note again that the overall controller gain K_c is the only controller design parameter, as T_i and T_d in (4.3) are kept fixed. An elaboration on finding the bounds (4.12) and (4.12) is given in Appendix F.

For $K_c \in \mathcal{A}_{PD}$ or $K_c \in \mathcal{A}_{PID}$ for the PD- or PID controlled system, respectively, the set of controller gains for which limit cycling can occur is sought through a bifurcation analysis. A bifurcation is a qualitative change in system behaviour, e.g., a change from an equilibrium point to a limit cycle. It is identified by evaluating the simulated position response of the closed-loop system (4.6) using various controller gains within the linear stability ranges (4.12) and (4.13), with various various initial conditions. The resulting bifurcation plots are shown in Fig. 4.5 and Fig. 4.6 for a PD- and PID-controlled system, respectively. Here the solutions of the analytical equilibrium points/sets, given by (4.10) and (4.11), are shown as the black solid lines (equilibrium points) and gray areas (equilibrium sets). The dashed lines represent the difference between the maximum- and minimum value of the periodic limit cycle solution for the considered state, after a certain amount of time (steady-state solution), indicated with $\max(\cdot)$.

The bifurcation diagrams in Fig. 4.5 and 4.6 show that limit cycles do not occur for lower controller gains. Consequently, for the PID-controlled system, stability of the setpoint is guaranteed when a sufficiently low gain is employed, since the only solution is the equilibrium point $x_2 = 0$. However, transient performance issues must now be considered, since a low gain may result in slow or inaccurate trajectory tracking. Increasing the controller gain K_c, eventually leads to a bifurcation. In this particular

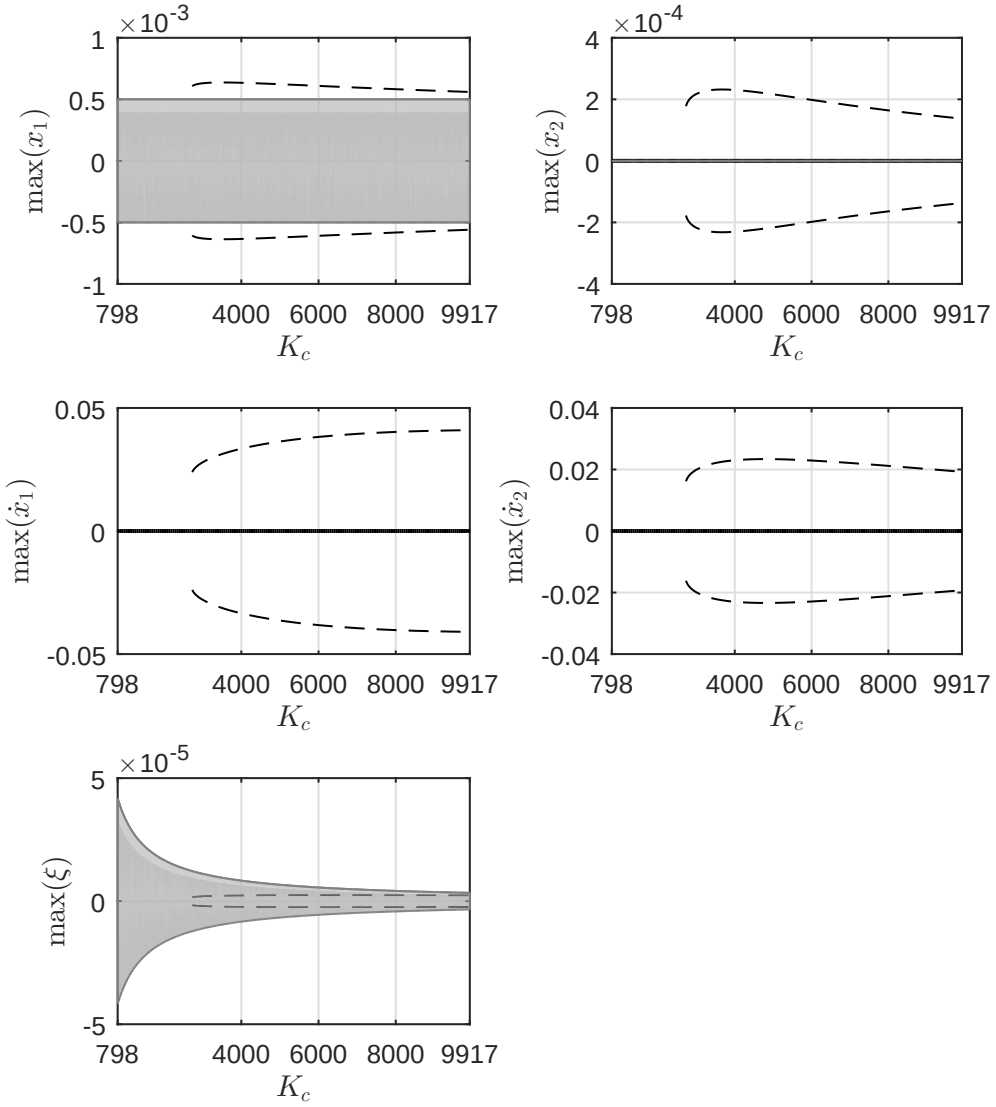

Fig. 4.6. Bifurcation plots PID-controlled system. The maximum value of the states (x_1, x_2, $\dot{x}_1$, $\dot{x}_2$, ξ) are plotted against the controller gain K_c. The dotted lines represent limit cycles, the solid lines represent equilibrium points and the grey areas represent an equilibrium set.

case study, a fold bifurcation occurs at $K_c = 6700$ for a PD-controlled system, and at $K_c = 2730$ for a PID-controlled system. This means that including an integrator in the controller significantly decreases the maximum gain below which limit cycles are guaranteed to be absent. This confirms the observation from the illustrative example, where including an integrator induced limit cycling. It can also be observed that the maximum value of the limit cycle shown in Fig. 4.5 and 4.6 corresponds to the values from the illustrative example in Fig. 4.4.

In order to better visualize the limit cycles, the $x_1 - x_2$ plane is visualized in Fig. 4.7 and Fig. 4.8, for the PD- and PID-controlled system respectively. Although the actual 4- or 5-dimensional problem (for PD- and PID-controlled system respectively) cannot

be visually represented in a single figure, the phase planes still give clear insight in the size and shape of the limit cycles and the influence of the initial conditions.

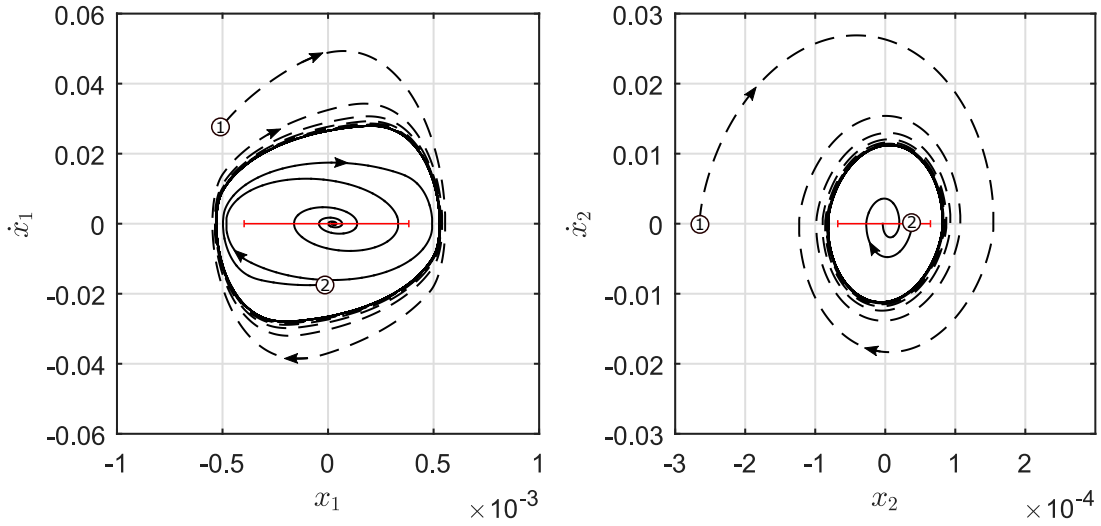

Fig. 4.7. Phase plane of the PD-controlled system with $K_c = 8000$. Depending on the initial condition (two initial conditions are plotted), the system either converges to an equilibrium set with a steady-state error (trajectory 2, solid lines) or converges to a stable limit cycle (trajectory 1, dashed lines). The red line represents the equilibrium set.

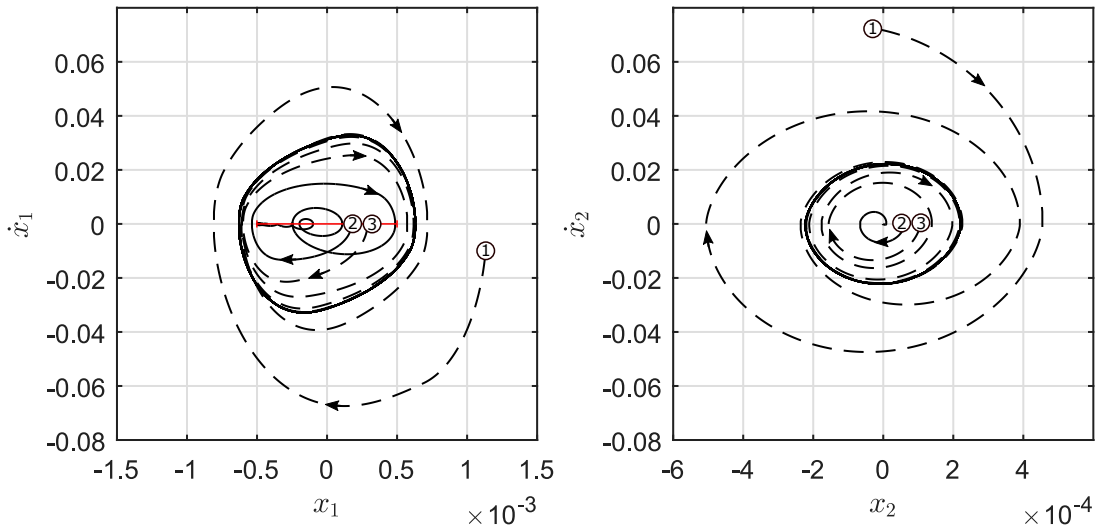

Fig. 4.8. Phase plane of the PID-controlled system with $K_c = 4000$. Depending on the initial condition (three initial conditions are plotted), the system either converges to an equilibrium set with a steady-state error (trajectory 2, solid lines) or converges to a stable limit cycle (trajectory 1 and 3, dashed lines). The red line represents the equilibrium set.

In both phase plane plots, the stable limit cycle is sketched as the bold line and the equilibrium set is shown as the red interval. Trajectory 1 starts outside the stable limit cycle and spirals inwards to the stable limit cycle. Trajectory 2 starts 'inside' the limit cycle and spirals towards the equilibrium set. Trajectory 3 in Fig. 4.8 also starts 'inside' the stable limit cycle, but spirals towards the stable limit cycle. The fact that a trajectory can either spiral towards the equilibrium set or towards the limit cycle means that there must exist a boundary in the region of attraction between the two attracting sets. This boundary is the unstable branch of the limit cycle and determines whether a trajectory is attracted to the limit cycle or to the equilibrium, depending on which side of the unstable branch of the limit cycle the states are.

4.4.1 Discussion

This section highlights the importance of considering friction-induced limit cycling for flexible 2 DOF systems, in controller design. Namely, limit cycles can occur without the presence of a Stribeck effect in the friction characteristic, or the presence of an integrator in the controller. This is unlike the 1 DOF case, where at least one of those aspects is required for limit cycles to occur.

Furthermore, it is found that limit cycles can be avoided by sufficiently decreasing the controller gain. Consequently, stability of the setpoint is guaranteed when PID-control with sufficiently low gain is employed. However, transient performance issues must now be considered, since low gain may result in slow or inaccurate trajectory tracking.

The following figures in this section are created using the same system values, enabling direct comparison between them. The position response in Fig. 4.4 shows the limit cycling behaviour for a specific case. The bifurcation plots in Figs. 4.5 and 4.6 indicate the existence of periodic and/or equilibrium solutions for all controller gains within the linear stability range. The phase planes presented in Figs. 4.7 and 4.8 give a visual representation of the solution based on the initial conditions, for a specific controller gain.

4.5 Stability analysis tools

The bifurcation analysis of Section 4.4 gives good insight in the dynamical behaviour of the system, but it is generally a time-consuming procedure, which makes it not particularly suitable for controller design. Therefore, it is desired to use a more general approach to determine asymptotic stability of the solution corresponding to the setpoint, suitable for controller design. To this end, two conditions are investigated which address this issue: one based on *absolute stability* of the system, the other based on a *Bendixson-like criterion*, which guarantees the absence of limit cycles.

4.5.1 Absolute stability

A well-known analysis tool for non-linear systems is the Circle criterion, stated as Theorem 7.1 in [25], which gives sufficient conditions for absolute stability, as defined in the Kalman-Yakubovich-Popov (KYP) lemma, see Lemma 6.3 in [25]. However, based on the bifurcation plots in Fig. 4.5 and 4.6, resulting from the simulation analysis in Section 4.4, it can be concluded that absolute stability of the closed-loop system (4.6), with matrices given in (4.8) or (4.9), is not possible. This fact can be concluded because for some states, any controller gain K_c, result in an equilibrium *set*, while absolute stability requires that all states converge to an isolated equilibrium *point*. Consequently, this condition cannot be used for checking the feasibility of a controller of the form (4.8c) or (4.9c) for the particular case study considered in this chapter.

Expanding the controller K in (4.5) to a full-state feedback controller $K_{full} \in \mathbb{R}^{1x6}$, with the 6-dimensional state $x_{full} = \begin{bmatrix} x_1 & x_2 & \dot{x}_1 & \dot{x}_2 & \xi_1 & \xi_2 \end{bmatrix}$, where ξ_1 is an additional integrator term acting on the first mass, and adjusting the system matrices in (4.9) accordingly, also can not render the closed-loop absolutely stable. Solving the KYP criterion for both $K = K_{full}$ and P results in a non-linear problem due to the multiplication of the two decision variables, see Appendix G. A well-known approach to convert this problem to an LMI, is to apply a change in variables, see, e.g., Example 4 in [27]. However, the resulting LMI has been checked to be infeasible, concluding that the design of a controller based on absolute stability is too restrictive for this particular case study.

4.5.2 Bendixson-like criterion

A less restrictive requirement compared to absolute stability is the *Bendixson-like criterion* presented in [28]. This is an LMI-based criterion for Lur'e-type systems that ensures the absence of limit cycles for nonsmooth dynamical systems. This criterion does not exclude quasi-periodic behaviour or chaos and hence asymptotic stability of the setpoint can not be verified with this criterion. However, these kinds of solutions are not observed in simulation, so despite the lack of actually guaranteeing global asymptotic stability of the setpoint, this Bendixson-like criterion can serve as a useful basis for controller design. The criterion is stated as follows.

(Bendixson-like criterion) *Suppose there exists μ and positive definite matrix P such that the following inequality*

$$\begin{bmatrix} P((A+BK)-\mu I_n)+((A+BK)-\mu I_n)^T P & * & * \\ H^T P - C & 0 & 0 \\ H^T(P(A+BK)+(A+BK)^T P)+\kappa C & 0 & 0 \end{bmatrix} \geq 0 \tag{4.14}$$

is satisfied for some $\kappa \geq 0$. Then if

$$tr(A) - (n-2)\mu < 0$$

the system (4.6) *does not have periodic solutions.*

The proof for this condition is provided in [28]. For known system matrices A, B, C, H and a known controller K, the condition (4.14) can be verified using standard

LMI techniques, to rule out the possibility of limit cycles. For this, μ is varied in an external loop, while searching for feasible solutions for P satisfying (4.14), for given μ, in each iteration. The existence of a feasible solution cannot be ruled out, based on the bifurcation plots in Fig. 4.5 and Fig. 4.6, as was the case with the absolute stability criterion. This is true because these figures clearly show that there exist controller gains K_c for which limit cycles are avoided. Despite this fact, however, a feasible solution could not be found for (4.14) for the considered closed-loop system. Therefore, it is concluded that this criterion is also too conservative to serve as a basis for controller design in this particular case.

4.5.3 Discussion

Attempts to verify absolute stability, or the absence of limit cycles, for the closed-loop system (4.6) with matrices (4.9), have resulted in infeasible problems. An attempt to find a full-state feedback controller which renders the closed-loop system (4.6) absolutely stable based on the Circle criterion, have also resulted in an infeasible problem. Controller synthesis based on the Bendixson-like criterion (4.14) is not achieved since this involves solving a non-linear matrix inequality, which is not solvable with standard LMI solving techniques.

4.6 Proposed control strategies

In this section, two alternative control strategies for setpoint control of the closed-loop system (4.6) are proposed. The goal is to regulate the non-collocated mass m_2, which is subject to set-valued friction, to a desired setpoint, by applying a control input u in (4.4) to the first mass m_1. First, the stability- and performance issues related to this control goal are briefly reiterated. Secondly, a switching control strategy is proposed for improving the transient behaviour towards to setpoint. After this, a reset control strategy is proposed, which aims on improving the settling performance similar to the reset controller presented in Section 3.4 and [2], but taking the flexible dynamics into account. The achievable performance benefits for both control strategies are illustrated in simulation.

The first, *stability*-related control problem is illustrated in the simulation example in Section 4.3. Here, it is shown that employing a PD- or PID controller for setpoint control of a flexible system subject to non-collocated friction, induces the risk of experiencing limit cycling. To address this issue, i.e., achieve the absence of limit cycles, the results of the bifurcation analysis in Section 4.4 are used for controller design. These results confirm that a PD-controlled system subject to friction converges to a non-zero steady-state error and therefore the setpoint is never asymptotically stable. Therefore, PID-control is employed instead, which can asymptotically stabilize the second mass to its setpoint. However, PID-control is limited by a low gain, since a larger gain may result in limit cycles, as Fig. 4.6 illustrates. High-gain feedback (high bandwidth) is generally preferred over low-gain feedback, for its performance benefits in terms of input tracking and robustness against uncertainties and disturbances. The *ability* for a high-gain when PD control is employed, but the *necessity* for PID control to achieve

asymptotic stability, motivates a PD-to-PID switching control strategy in the next section.

4.6.1 PD-to-PID switched control

The intuition behind the switching control strategy proposed below is as follows. A high-gain PD-controller is used to bring the system close to its setpoint. When the PD-controlled system gets in the stick phase and is unable to escape this stick-set indefinitely, a switch to low-gain PID-control is performed, to achieve convergence to its setpoint, while avoiding the occurrences of limit cycles.

To determine the switching instant, consider again the equations of motion of the system (4.6), first introduced in (4.1):

$$\begin{cases} m_1\ddot{x}_1 = u + k(x_2 - x_1) + d(\dot{x}_2 - \dot{x}_1), \\ m_2\ddot{x}_2 \in -k(x_2 - x_1) - d(\dot{x}_2 - \dot{x}_1) - F_s\text{Sign}(\dot{x}_2). \end{cases} \tag{4.15}$$

Here, $k(x_2 - x_1) + d(\dot{x}_2 - \dot{x}_1)$ represents the internal force between m_1 and m_2, due to the flexibility connecting the two masses, see Fig. 4.9a. Elimination by substitution results in

$$m_2\ddot{x}_2 \in -m_1\ddot{x}_1 + u - F_s\text{Sign}(\dot{x}_2). \tag{4.16}$$

Evaluating (4.16) at $\dot{x}_2 = \ddot{x}_2 = 0$ gives

$$0 \in -m_1\ddot{x}_1 + u - F_s\text{Sign}(0), \tag{4.17}$$

which is written as an inequality to give the condition for m_2 to be in the stick phase:

$$|u - m_1\ddot{x}_1| \leq F_s. \tag{4.18}$$

Here, the expression $u - m_1\ddot{x}_1$ is the *internal force acting on the second mass*, see Fig. 4.9b, which is defined from here on as

$$\begin{aligned} F_{int} &:= k(x_2 - x_1) + d(\dot{x}_2 - \dot{x}_1) \\ &:= u - m_1\ddot{x}_1. \end{aligned} \tag{4.19}$$

Note that the internal force in (4.19) can either be written in terms of relative position and velocity between the first and second mass, or in terms of control input u and

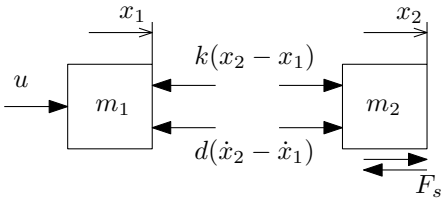

(a) Internal force in terms of relative position and velocity of the first and second mass.

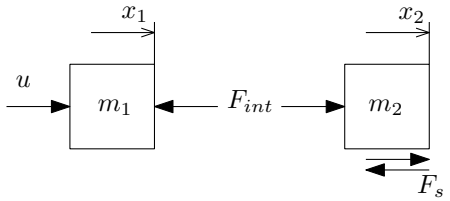

(b) Internal force as defined in (4.19).

Fig. 4.9. Free-body-diagram of a flexible 2 DOF system.

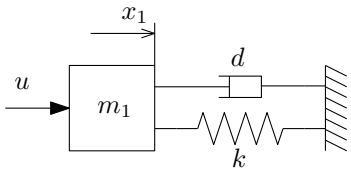

Fig. 4.10. Free-vibrating model of m_1, representing the situation when m_2 is in the stick phase.

the acceleration of the first mass $\ddot{x}_1$. The first formulation requires exact knowledge of the stiffness and damping parameters between the two masses, which are often not accurately known in practice. The acceleration, on the other hand, may be measured with an accelerometer, which makes the second formulation of (4.19) the preferred choice in practice. Irrespective of the formulation, the key conclusion is that whether the second mass resides in stick, depends on the state of the first mass.

For the second mass to remain in stick indefinitely, (4.18) has to hold for all future time. At the moment the second mass m_2 sticks, the (frictionless) first mass m_1 can be considered as a single vibrating mass, as in Fig. 4.10. In this situation, the actuation force u remains constant, due to the lack of integrator action in the PD-controller and the fact that x_2 is constant and $\dot{x}_2 = 0$. The internal damping between the first and second mass, which is always present in a practical system, causes the (PD controlled) position response of m_1 to behave as a damped, decaying oscillation. Consequently, the resulting internal force F_{int}, defined in (4.19), behaves as a decaying oscillation as well, see Fig. 4.11 for the time interval indicated by the grey area. This means that whenever the oscillating internal force reaches a maximum that is smaller than the friction force F_s, the internal force will never exceed the friction force in the future, and consequently, the second mass will stick indefinitely. To detect the moment at which the oscillating internal force is at a maximum, its time derivative must be zero, indicated as the red bars in Fig. 4.11. The following three conditions embed these criteria, at which a switch to PID control occurs, such that convergence to the setpoint is achieved.

$$\dot{x}_2 = 0, \tag{4.20a}$$

$$\frac{d}{dt}F_{int} = 0, \tag{4.20b}$$

$$|F_{int}| \leq F_s, \tag{4.20c}$$

with F_{int} defined in (4.19). The grey patches in Fig. 4.11 indicate when all three switching conditions (4.20) hold. These switching conditions enable the definition of the switching control strategy as follows.

(PD-to-PID switching control strategy) *Start with high-gain*[2] *PD-control, to control the system close to the setpoint. When the PD-controlled system gets in stick and is unable to escape this stick-set indefinitely, i.e., the conditions* (4.20) *hold, switch to low-gain PID-control, to guarantee convergence to the setpoint, while avoiding limit cycles.*

[2]But low enough to avoid limit cycles.

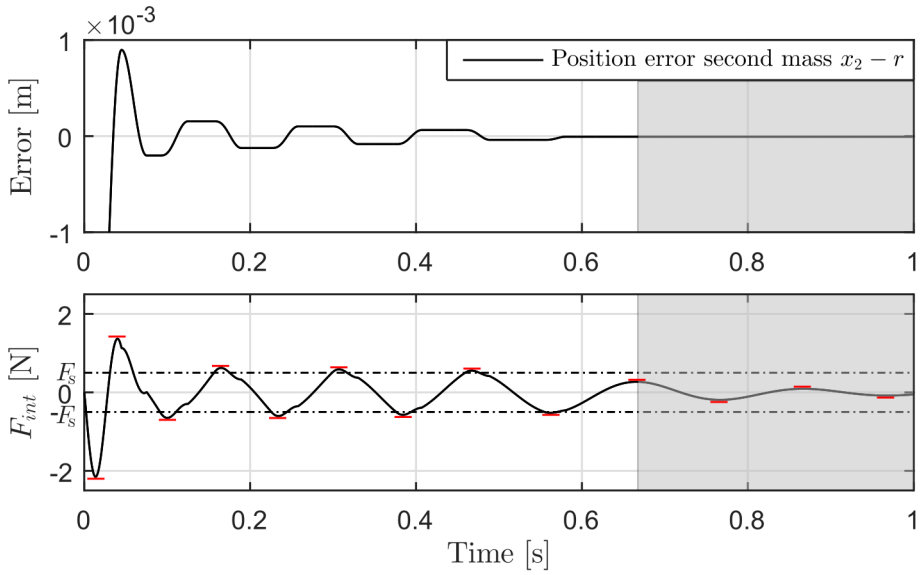

Fig. 4.11. Decaying internal force as a result of a PD controlled step reference. The grey area indicates when the second mass is in stick and the switching conditions in (4.20) are satisfied.

Illustrative example

The following illustrative example shows the achievable performance benefits of the proposed switching control strategy, compared to classical PD- and PID control. Based on the bifurcation plots in Fig. 4.5 and 4.6, limit cycles are avoided for $1 < K_c < 6700$ for PD-control, and $798 < K_c < 2730$ for PID-control. In this example, a PD-controller with $K_c = 5000$ is used to bring the system close to the setpoint, after which an integrator is added and the gain is decreased to $K_c = 2500$, thereby avoiding limit cycling also for the PID controller.

The simulated position response of the PD-, PID- and PD-to-PID-controlled system (4.6) to a step reference of 0.01 m, is shown in Fig. 4.12. Here, system matrices (4.8) and (4.9) are used, with parameter values given in Table 4.1 and 4.2. It can clearly be observed that the PID-controlled system suffers from significantly more overshoot, compared to the PD-controlled system. This large initial overshoot results in large oscillations around the setpoint. The PD-controlled system gets in stick indefinitely after around 1 second, i.e., conditions (4.20) hold. At this moment, the controller switches to low gain PID control, to regulate the system further towards the setpoint. The transient performance benefits of the proposed switched control technique is clearly demonstrated in this illustrating example.

4.6.2 Reset control

As an addition to the switched control strategy, a reset PID control strategy is proposed. Again, a 2 DOF system with non-collocation of actuation and sensing, and non-collocation of actuation and friction is considered, as in Fig. 4.1. For the control

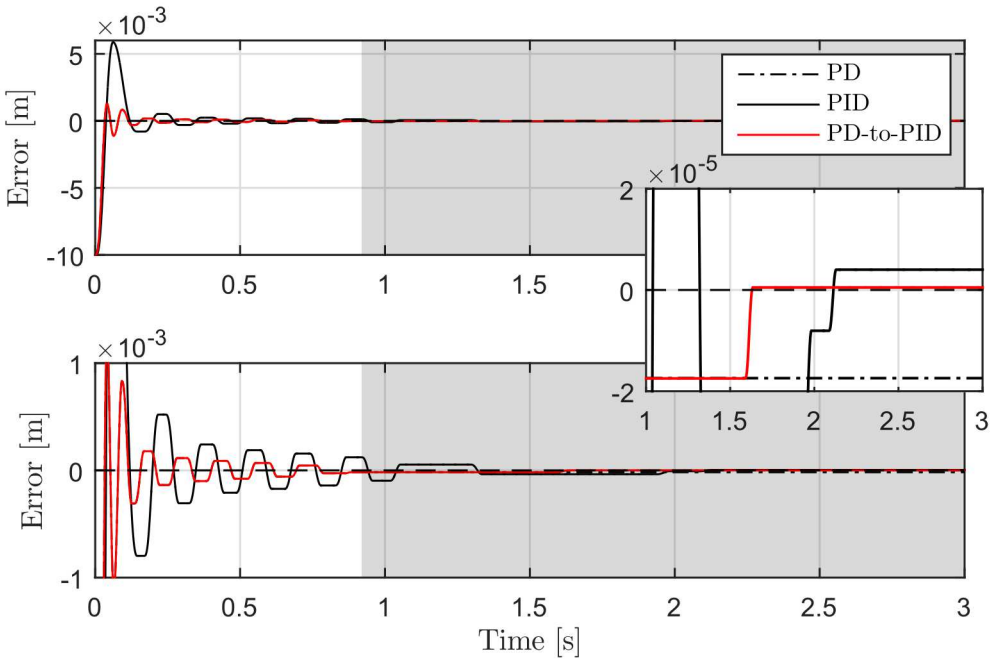

Fig. 4.12. Simulated position response of x_2 to a step of 0.01 m for a PD (black dash-dot), PID (black) or switched (red) system. The bottom plot is a vertically zoomed in version of the top plot. The white/grey areas represent the switch from PD (white) to PID (grey).

strategy proposed in the previous section, once the PD-controlled system is regulated close towards the setpoint, the controller switches to PID control. This PID-controlled system, however, suffers from similar performance issues as discussed for the 1 DOF case in Section 3.3. Namely, the system suffers from slow convergence and therefore long settling times as a result of the (increasingly) slow depletion and refilling of the integrator buffer.

In order to improve the settling performance of a flexible system subject to non-collocated set-valued friction, a reset controller is proposed. The motivation behind this reset controller is similar to the motivation for the reset PID controller presented in Section 3.4. That is, resetting the integrator circumvents large portions of the filling and depletion of the integrator buffer, resulting in shorter periods of stick and thereby significantly faster settling. However, the mechanical flexibility in the system results in a decoupling of the applied control input and the force acting on the non-collocated mass, i.e., the point on which the friction acts. This decoupling is not taken into account in the original reset PID control strategy from Section 3.4, but is essential for effective control.

To illustrate the influence of the mechanical flexibility, consider the simulated position response in Fig. 4.13. Here, a reset PID controller, given in (3.10), with $\alpha = 0$, analogous to an integrator reset to zero, is used to regulate the system to a setpoint of $5 \cdot 10^{-5}$ m using a step reference. The position response of both the first (actuated) and second (sensed) mass are shown in the top plot. The internal force F_{int}, defined in

(4.19), and the integrator control force $u_{nonl} = K_c/T_i\xi$, where ξ is defined in (4.3), are shown in the bottom plot. In the first 0.2 seconds, the actuation force increases and the position of the first, actuated, mass follows correspondingly. After the internal force F_{int} becomes larger than the friction force, the second mass slips, see (4.18). In this case, the system overshoots its setpoint after which the reset conditions (3.10f) hold and the integrator is reset according to (3.10e). Since $\alpha = 0$, the integrator resets to zero. The core feature upon which the reset PID controller in Section 3.4 is designed, is the fact that, despite a discontinuous jump in the control force, a 1 DOF system always remains in stick, right after the reset. This design feature, however, is lost for a flexible 2 DOF system with only non-collocated friction. This is clearly seen in Fig. 4.13 in the position response and the oscillatory behaviour of the first (frictionless) mass. Consequently, due to the oscillation of the first mass, the internal force F_{int} in the bottom plot, also displays oscillatory behaviour, with a peak force significantly exceeding the integrator reset value. The peak force does, however, remain lower than

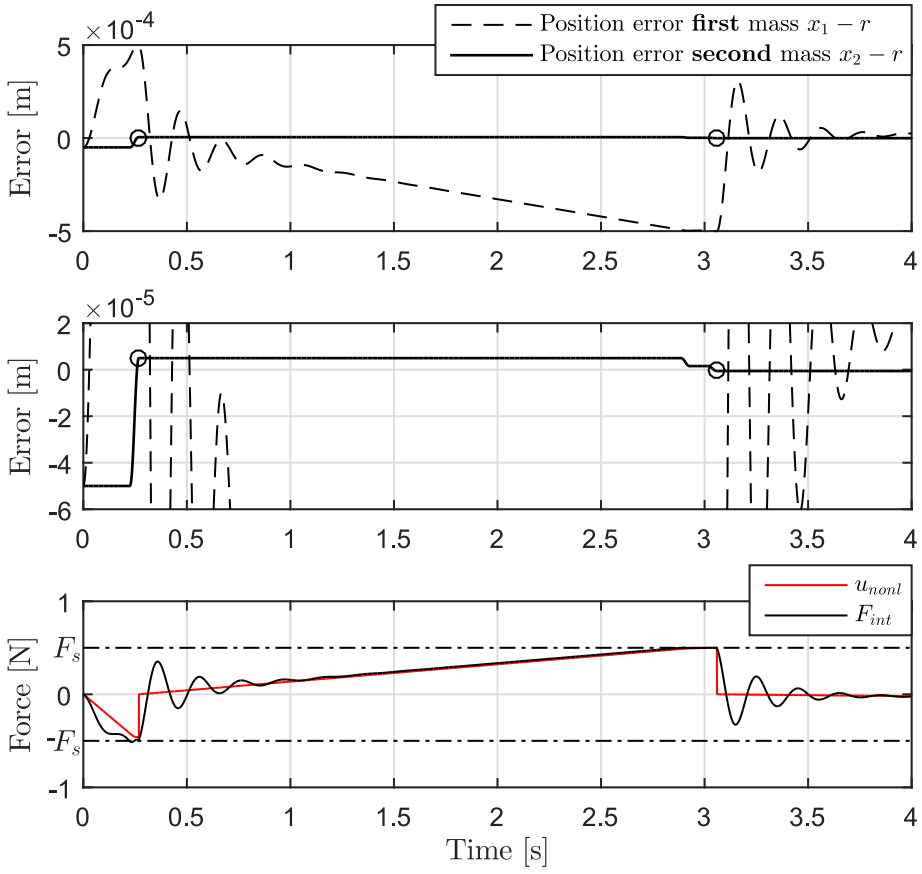

Fig. 4.13. Closed-loop simulation with reset control. Top: simulated position response x_1 (dashed) and x_2 (solid) to a step reference of $5 \cdot 10^{-5}$ m. A reset scaling factor $\alpha = 0$ is implemented. The reset instants are indicated by the black circles. Middle: zoomed in position response. Bottom: internal force acting on m_2, F_{int} (black) and the integrator force u_{nonl} (red).

the friction force and eventually converges towards the integrator control force. After the internal force exceeds the friction force, the second mass slips again, exceeds its setpoint, and another reset occurs.

For the case shown in Fig. 4.13, with $\alpha = 0$, the internal force does not exceed the friction force upon reset, and therefore does not influence the position response of the second mass. In Fig. 4.14, the results of a reset PID controller with $\alpha = 0.3$ are presented. In this case, the internal force *does* exceed the friction force upon reset, which causes the system to slip, overshoot the setpoint, enters a stick phase and, subsequently, triggers the reset conditions (3.10f) again.

This example shows that the PID reset controller proposed in [2] is not robust against flexible dynamics. A key intuition is that the state of the first mass is unknown and uncompensated for, while it does influence the stick-to-slip moments of the second mass. Therefore, the following alternative control strategy is proposed,

(Reset control strategy) *Employ full-state feedback to regulate the internal force F_{int} such that it resembles the reset integrator force, i.e., $F_{int} = u_{nonl}$.*

This is achieved by adding a derivative control action to the first mass, with gain $T_{d,1}K_c$, to suppress the oscillations of the first mass upon reset. This results in the closed-loop system (4.6) with controller

$$K_{PID} = \begin{bmatrix} 0 & K_c & T_{d,1}K_c & T_dK_c & T_iK_c \end{bmatrix} \tag{4.21}$$

The achievable performance benefits of this proposed reset control strategy are illustrated in Fig. 4.15. Here, the dashed lines represent the position response to a step

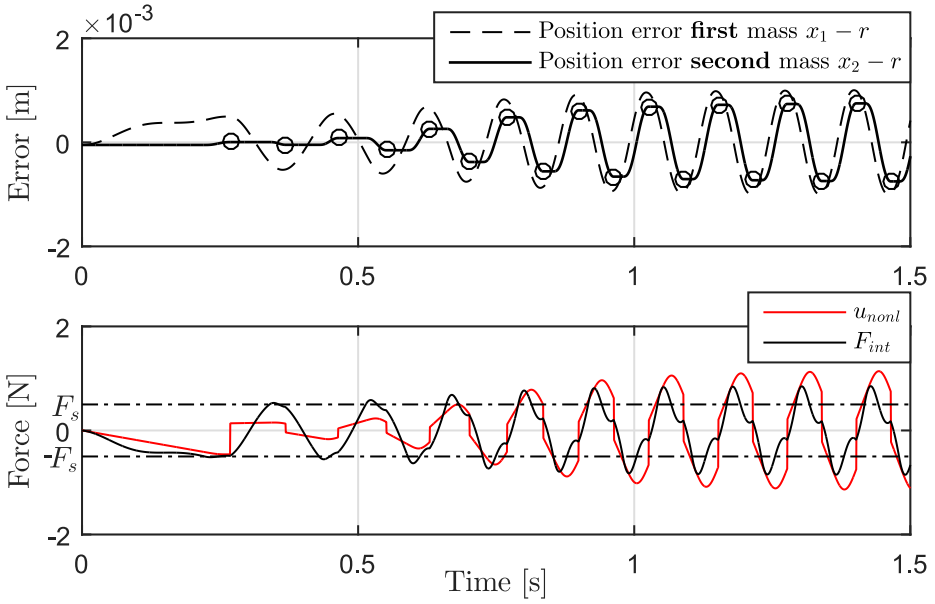

Fig. 4.14. Top: simulated position response x_1 (dashed) and x_2 (solid) to a step reference of $5 \cdot 10^{-5}$ m. A reset scaling factor $\alpha = 0.3$ is implemented, resulting in limit cycles. The reset instants are indicated by the black circles. Bottom: internal force acting on m_2, F_{int} (black) and the integrator force u_{nonl} (red).

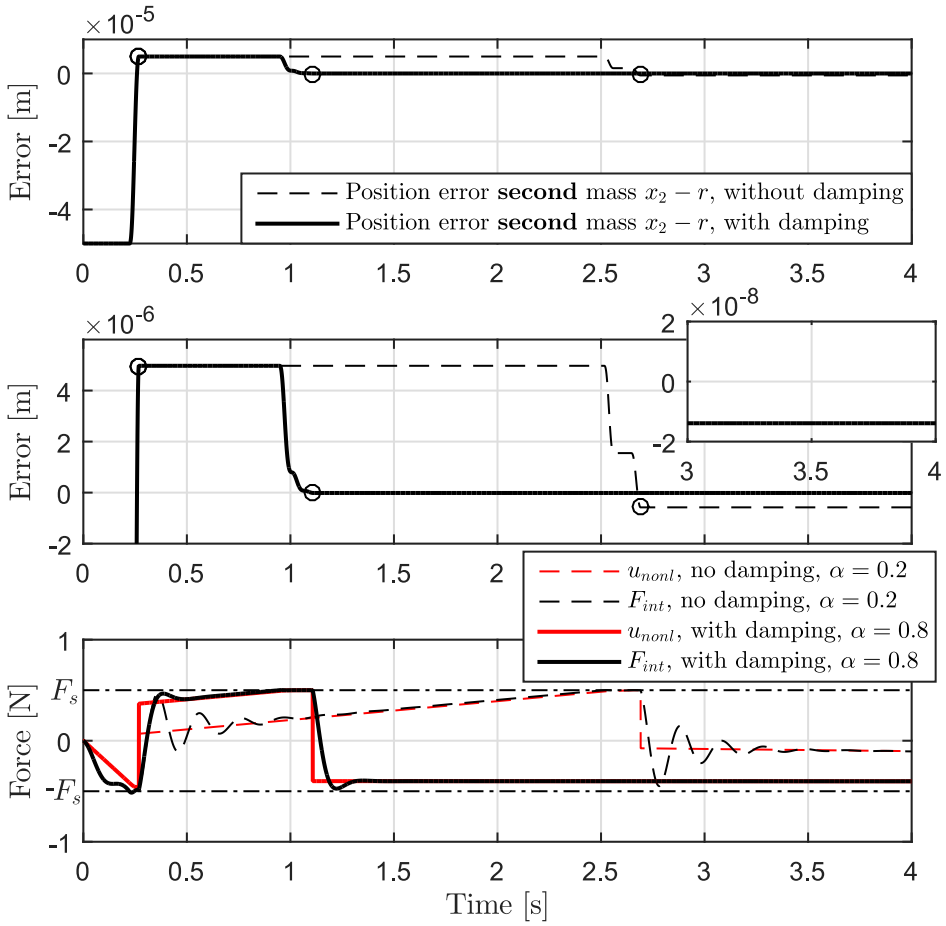

Fig. 4.15. Top: simulated position response x_2 (dashed) and x_2 (solid) to a step reference of $5 \cdot 10^{-5}$ m. A reset scaling factor $\alpha = 0.3$ is implemented, resulting in limit cycles. The reset instants are indicated by the black circles. Middle: a vertically zoomed in version of the top plot. Bottom: internal force acting on m_2, F_{int} (black) and the integrator force u_{nonl} (red).

reference of $5 \cdot 10^{-5}$ m with the originally proposed reset controller from Section 3.4. Here, $\alpha = 0.2$ is the maximum value which does not result in limit cycling, as in Fig. 4.14. The oscillatory behaviour of the first mass can clearly be seen upon reset. The solid lines represent the reset PID controller with added damping to the first mass through a derivative controller action. Now, $\alpha = 0.8$ can be employed, while still avoiding limit cycling. This higher α results in significantly shorter stick moments, and therefore increased settling performance.

4.6.3 Discussion

The results of the bifurcation study in Section 4.4 are used as a basis for the proposal of two performance-increasing control strategies. A switching control strategy is proposed,

for improving the transient behaviour towards the setpoint. Here, a high-gain PD controller is employed to bring the system close to the setpoint, after which a switch to low-gain PID control is performed, to achieve convergence, while avoiding limit cycles. To improve the settling performance in terms of settling time, also a reset control strategy is proposed, which employs full-state feedback to regulate the system such that the force acting on the controlled mass, resembles the reset behaviour of the reset PID controller, proposed in Section 3.4. This allows for employing a larger α, without re-introducing limit cycles. This consequently results in shorter stick moments and therefore increased settling performance. Simulation examples of both control strategies show significant achievable performance benefits, compared to classical PID control.

CHAPTER 5

Conclusions and recommendations

Electron microscopy plays an essential role in the research to new, innovative materials, in drug development, and in the manufacturing process of the semiconductor industry. A high-precision sample manipulation stage is employed to position the sample under the electron beam. In such high-precision positioning systems, friction is a performance limiting factor in terms of positioning accuracy and settling time, as it can induce non-zero steady-state positioning errors, limit cycling, and large settling times. These performance limitations are inherent to classical PID control, which is still employed in the vast majority of industrial applications. In this thesis, a reset PID controller is validated on an experimental setup, representative for the sample manipulation stage in an industrial electron microscope, to increase the performance in terms of settling times. Secondly, the effects of flexible dynamics on stability and settling performance of a system subject to set-valued, non-collocated friction are investigated analytically. This chapter presents general conclusions of the thesis and recommendations for future research.

5.1 Conclusions

The nano-positioning motion stage described in Chapter 2, representing the motion stage of an industrial electron microscope, is used as an experimental setup. The setup can be approximated by a single-mass model in the low- to medium-frequency range. At high frequencies (above 160 Hz), decoupling due to non-collocation of actuation and sensing requires a 2 DOF model to accurately describe the dynamics. The parameters of this 2 DOF model are estimated based on system identification results. Friction experiments showed the presence of macroscopic static- and viscous friction, as well as microscopic frictional effects.

Chapter 3 addresses the issues regarding setpoint control of a single mass, subject to

set-valued friction. Employing PD control to regulate a system subject to friction to a desired setpoint, results in a steady-state error. In the presence of a Stribeck effect, PID control can result in limit cycling, which is addressed in [22]. A system subject to Coulomb friction (with potentially a viscous contribution), suffers from (increasingly) slow convergence due to the refilling and depletion of the integrator buffer, resulting in long settling times. A reset PID controller is presented and experimentally implemented on the nano-positioning motion stage described in Chapter 2, to address this control problem specifically. The experimental results show significant performance improvement in terms of settling time, when employing the proposed reset PID controller, as compared to its classical PID counterpart. Increasing the size of the reset, generally increases the performance in terms of settling time. However, microscopic frictional effects result in elastic positional jumps upon an integrator reset. Larger controller resets result in larger elastic microscopic jumps, which may induce oscillatory behaviour around the setpoint, thereby limiting the size of the reset.

Chapter 4 provides an analytical study of setpoint control of flexible 2 DOF systems, subject to non-collocated friction. A simulation-based bifurcation analysis illustrates the possibility of limit cycling of a PD- and PID controlled system, subject to Coulomb friction without Stribeck effect. Limit cycling can be avoided by sufficiently decreasing the controller gain. Attempts to verify absolute stability, or design a full-state feedback controller which renders the closed-loop system absolutely stable, have resulted in infeasible problems. The attempt to verify the absence of limit cycles using an LMI-based Bendixson-like criteria, also gave no feasible solutions. Consequently, the results of the bifurcation study are used as a basis for the proposal of two performance-increasing control strategies. A switching control strategy is proposed, for improving the transient behaviour towards the setpoint. Here, a high-gain PD controller is employed to bring the system close to the setpoint, after which a switch to low-gain PID control is performed, to achieve convergence, while avoiding limit cycles. To increase the settling performance in terms of settling time, also a reset control strategy is proposed, which employs full-state feedback to regulate the system such that the force acting on the controlled mass, resembles the reset behaviour of the reset PID controller, proposed in Section 3.4. Simulation examples of both control strategies show significant achievable performance benefits, compared to classical PID control.

5.2 Recommendations

In this section, a few open problems and possible extensions for future research are listed.

- Friction has proven to limit the performance of a high-precision motion system in terms of accuracy and settling time. In particular, microscopic frictional effects cannot be neglected on the nanometer-positioning scale. Therefore, the frictional model can be expanded to include these microscopic (pre-sliding) frictional effects, allowing for model-based (feed-forward) friction compensation. However, obtaining an accurate model which is suitable for model-based friction compensation, may be challenging.

- Further research in non-model-based control techniques, which do not rely on accurate knowledge of the friction characteristic, such as dithering-based techniques and impulsive control, may be promising. In particular, the microscopic elastic effects, experimentally observed in Fig. 3.9 in Chapter 3, in the form of positional jumps upon controller reset, can potentially be exploited to improve the settling performance. This would require further research in the microscopic elastic behaviour of the system, since there is currently no linear relation between the size of the controller input and the size of the microscopic elastic jump.

- An alternative, or addition, to the proposed PD-to-PID switched control in Section 4.6, is to take initial conditions into account. When the positional error is sufficiently small, limit cycles do not occur, as indicated in the simulation-based analysis of Section 4.4. This would allow for high-gain PID control, while still avoiding limit cycles. Increasing the integrator gain, speeds up the filling/depletion of the integrator buffer, resulting in shorter moments of stick and, consequently, increased settling performance. This control strategy requires finding the switching surface, i.e., the unstable bifurcation branch, to determine for which initial conditions the system converges to its setpoint, instead of converging towards a limit cycle.

- To improve the performance in terms of accuracy and settling times of the experimental setup, or a general flexible 2-DOF system as considered in Chapter 4, a second actuator can be added to control the second mass directly, resulting in a long-stroke/short-stroke control strategy. The experimental setup is equipped with a piezoelectric actuator, which can be used for this purpose. A sequential- and dual-axis control strategy has been investigated in [16], but this research does not consider the effects of friction. Therefore, this research can be expanded to investigate the effect of friction on fully-actuated (flexible) systems.

- Currently, the reset control strategy strategy proposed in Section 4.6 only adds a derivative term to attenuate the oscillations of the first mass upon a controller reset. By expanding this to full-state feedback control, the internal force F_{int} can be better regulated to follow the reset integrator profile.

- A learning algorithm integrated with extremum seeking control can be implemented to improve the settling performance, without the need for a friction- or system model. Industrial motion systems often execute repetitive tasks. In the case of an electron microscope, for example, the sample stage makes repetitive movements to create a full image of a sample. This motivates the investigation of a learning control strategy, to improve the performance of the experimental setup, integrated with extremum seeking control, which is robust against disturbances such as (time-varying) friction effects.

- An extension to the friction-induced limit cycling analysis in Section 4.4, is to include collocated friction. Additionally, the friction characteristic can be expanded to contain a Stribeck effect and, potentially, microscopic frictional effects. The exact influence of system parameters, specifically damping, on limit cycling behaviour needs further investigation, since this is still not fully understood [29].

- An even further extension to the friction-induced limit cycling analysis in Section 4.4, is to consider a N DOF system, with friction acting on all N masses. This would enable analysis of friction-induced limit cycles in complex, multibody systems.

- The limit cycling behaviour in flexible systems, observed in simulation in Section 4.4, can be investigated experimentally. For proper investigation, a setup is required in which the damping and stiffness parameters are adjustable. If this limit cycling behaviour is observed experimentally, the control strategies proposed in Section 4.6 can be implemented and experimentally validated.

- Before implementing the proposed control strategies in Section 4.6, a stability proof is required to prove that the setpoint is asymptotically stable. The simulation study in Section 4.4 *suggests* asymptotic stability of the setpoint, but this has not yet been proven.

- For improving the settling performance of the industrial R_x motion stage (described in Section 1.1), the reset control strategy presented in 3.4 can be directly implemented, as this control strategy has proven to be effective in reducing settling times on the experimental setup (which represents the industrial motion stage). However, since microscopic frictional effects are not compensated for, and may induce robustness issues in a practical application, a low scaling factor α should be employed. This increases the robustness against unknown frictional effects, at the cost of settling performance.

Bibliography

[1] R. Beerens, L. Zaccarian, N. van de Wouw, M. Heemels, and H. Nijmeijer, "Hybrid PID control for transient performance improvement of mechanical systems with friction," *Proc. American Control Conference*, 2017.

[2] R. Beerens, A. Bisoffi, L. Zaccarian, W. Heemels, H. Nijmeijer, and N. van de Wouw, "Reset integral control for improved settling of motion systems with friction," *submitted to Automatica*, 2018.

[3] B. Armstrong-Helouvry, P. Dupont, and C. C. De Wit, "A survey of models, analysis tools and compensation methods for the control of machines with friction," *Automatica*, vol. 30, no. 7, pp. 1083–1138, 1994.

[4] L. Freidovich, A. Robertsson, A. Shiriaev, and R. Johansson, "LuGre-model-based friction compensation," *IEEE Transactions on Control Systems Technology*, vol. 18, no. 1, pp. 194–200, 2010.

[5] D. Rijlaarsdam, P. Nuij, J. Schoukens, and M. Steinbuch, "Frequency Domain Based Friction Compensation - Industrial Application to Transmission Electron Microscopes -," *Proc. American Control Conference*, pp. 4093–4098, 2011.

[6] N. Mallon, N. van de Wouw, D. Putra, and H. Nijmeijer, "Friction compensation in a controlled one-link robot using a reduced-order observer," *IEEE Transactions on Control Systems Technology*, vol. 14, no. 2, pp. 374–383, 2006.

[7] V. van Geffen, *A study of friction models and friction Compensation.* MSc thesis, Eindhoven University of Technology, 2009.

[8] Y. F. Liu, J. Li, Z. M. Zhang, X. H. Hu, and W. J. Zhang, "Experimental comparison of five friction models on the same test-bed of the micro stick-slip motion system," *Mechanical Sciences*, vol. 6, no. 1, pp. 15–28, 2015.

[9] A. Amthor, S. Zschaeck, and C. Ament, "High precision position control using an adaptive friction compensation approach," *IEEE Trans. Autom. Control*, vol. 55, no. 1, pp. 274–278, 2010.

[10] J. Na, Q. Chen, X. Ren, and Y. Guo, "Adaptive prescribed performance motion control of servo mechanisms with friction compensation," *IEEE Transactions on Industrial Electronics*, vol. 61, no. 1, pp. 486–494, 2014.

[11] L. Iannelli, U. T. Jönsson, and F. Vasca, "Averaging of nonsmooth systems using dither," *Automatica*, vol. 42, no. 4, pp. 669–676, 2006.

[12] A. A. Pervozvanski and C. Canudas-de Wit, "Asymptotic analysis of the dither effect in systems with friction," *Automatica*, vol. 38, no. 1, pp. 105–113, 2002.

[13] Y. Orlov, R. Santiesteban, and L. T. Aguilar, "Impulsive control of a mechanical oscillator with friction," *Proceedings of the American Control Conference*, no. 4, pp. 3494–3499, 2009.

[14] N. Van De Wouw and R. Leine, "Impulsive control of mechanical motion systems with uncertain friction," *Proceedings of the IEEE Conference on Decision and Control*, pp. 4176–4182, 2011.

[15] M. Ruderman, "Impulse-Based Hybrid Motion Control," *IEEE Conference of Industrial Electronics Society*, vol. 43, 2017.

[16] R. van Hulst, *Dual Stage Actuator Test Setup.* BSc, Fontys Hogeschool Eindhoven, 2017.

[17] P. E. Wellstead, "Non-parametric methods of system identification," *Automatica*, vol. 17, no. 1, pp. 55–69, 1981.

[18] R. van der Maas, *Advanced Geometric Calibration and Control for Medical X-Ray Systems.* Ph. D. thesis, Eindhoven University of Technology, 2016.

[19] A. van Rietschoten, *Open-Loop Non-Parametric Identification.* MSc thesis, Eindhoven University of Technology, 2015.

[20] N. van de Wouw, "An introduction to Time-Stepping: a Numerical Technique for Mechanical Systems with Unilateral Constraints," tech. rep., Eindhoven University of Technology.

[21] R. H. A. Hensen, M. J. G. van de Molengraft, and M. Steinbuch, "Friction induced hunting limit cycles: A comparison between the LuGre and switch friction model," *Automatica*, vol. 39, no. 12, pp. 2131–2137, 2003.

[22] R. Beerens, H. Nijmeijer, M. Heemels, and N. van de Wouw, "Set-point Control of Motion Systems with Uncertain Set-valued Stribeck Friction," *IFAC-PapersOnLine*, vol. 50, no. 1, pp. 2965–2970, 2017.

[23] A. Bisoffi, M. Da Lio, A. Teel, and L. Zaccarian, "Global Asymptotic Stability of a PID Control System with Coulomb Friction," *IEEE Transactions on Automatic Control*, no. 1, 2017.

[24] R. Goebel, R. G. Sanfelice, and T. R. Andrew, *Hybrid Dynamical Systems: Modeling, Stability and Robustness.* Princeton, New Jersey: Princeton University Press, 2012.

[25] H. K. H. Khalil, *Nonlinear Systems.* Prentice Hall, Inc., third ed., 1996.

[26] D. Putra, *Control of limit cycling in frictional mechanical systems.* Ph. D. thesis, Eindhoven University of Technology, 2004.

[27] C. W. Scherer and S. Weiland, "Linear Matrix Inequalities in Control," tech. rep., Eindhoven University of Technology, 2005.

[28] A. Pogromsky, H. Nijmeijer, and J. Rooda, "A negative Bendixson-like criterion for a class of hybrid systems," *IEEE Transactions on Automatic Control*, vol. 52, no. 4, pp. 586–595, 2007.

[29] J. J. Sinou and L. Jézéquel, "Mode coupling instability in friction-induced vibrations and its dependency on system parameters including damping," *European Journal of Mechanics*, vol. 26, no. 1, pp. 106–122, 2007.

Appendices

APPENDIX A

Model reduction

The full dynamic model is given in Figure A.1. This model is reduced in a number of steps by eliminating the small masses and high stiffness components.

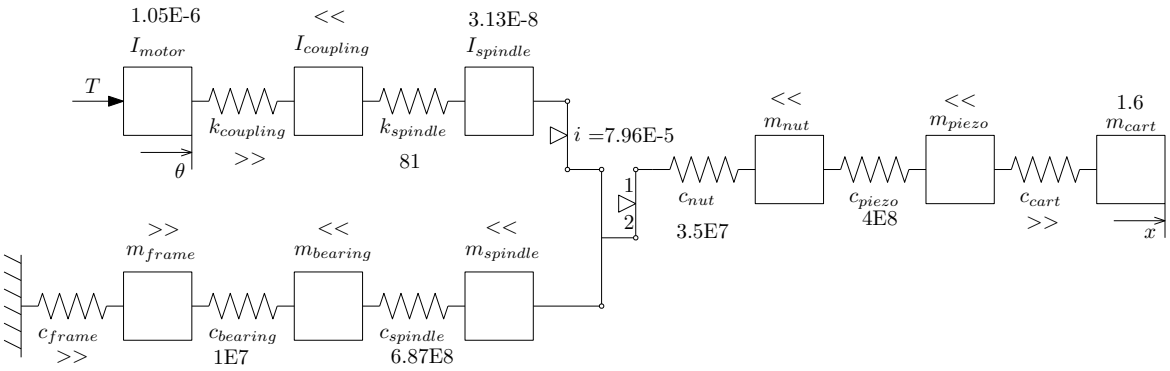

Fig. A.1. Step 1: full model.

The frame is considered infinitely stiff and orders of magnitude heavier than both the bearing and the spindle. Combining the stiffness of the spindle, the bearing and the nut, results in the reduced model given in Figure A.2.

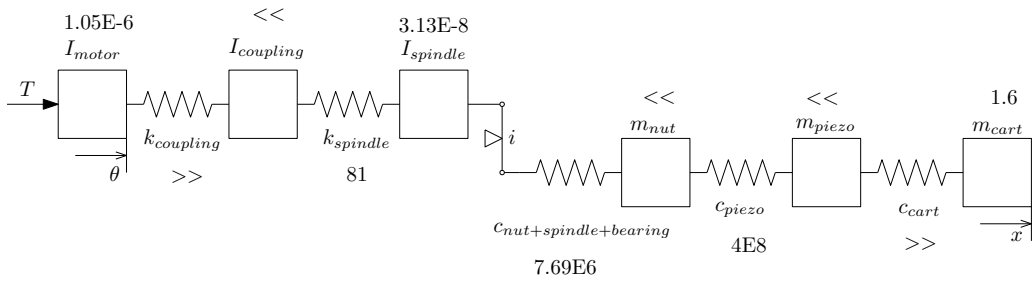

Fig. A.2. Step 2.

The mass of the piezo and nut is orders of magnitude smaller than the mass of the carriage. Similarly, the inertia of the coupling is orders of magnitude smaller than the inertia of the motor and the spindle. Both the stiffness of the carriage and the radial stiffness of the coupling are considered infinitely stiff. This result in the reduced model given in Figure A.3.

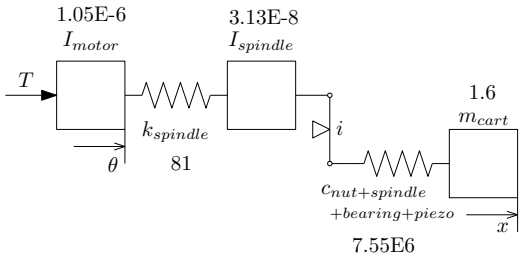

Fig. A.3. Step 3.

Removing the transmission is done by dividing the inertia and stiffness by i^2, dividing the input torque T by i and multiplying the angle of the motor by i, resulting in the model shown in Figure A.4.

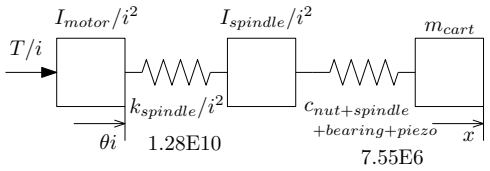

Fig. A.4. Step 4.

The last step is to combine the inertia of the motor and the spindle, since the radial stiffness of the spindle divided by i^2 is orders of magnitude larger than the combined stiffness of the nut, spindle, bearing and piezo. A damper is added to represent any internal damping and friction components. This results in the reduced 4th order model shown in Figure A.5.

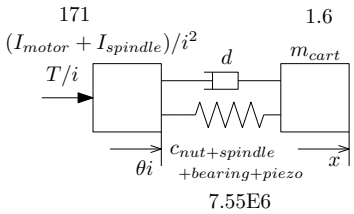

Fig. A.5. Step 5.

A.1 Parameter estimation

Table A.1: System parameter estimation of the experimental setup

Mechanical part	**Parameter**	**Symbol**	**Equation**	**Value**	**Unit**
Motor	Motor inertia	J		1.05e−6	$\mathrm{kg\,m^2}$
Transmission	Pitch	p		5e−4	m
	Transfer ratio	i		7.96e−5	
Bearing	Bearing stiffness	$C_{bearing}$		1e7	$\mathrm{N\,m^{-1}}$
Spindle	Radius	r		2.5e−3	m
	Mass	$m_{spindle}$		1e−2	kg
	Inertia	I	$\frac{1}{2}mr^2$	3.13e−8	$\mathrm{kg\,m^2}$
	Modulus of elasticity	E		2.1e11	
	Area	A		1.96e−5	$\mathrm{m^2}$
	Max. length	L_{max}		6e−3	m
	Moment of inertia	I_p	$(\pi D^4)/32$	6.14e−11	$\mathrm{m^4}$
	Modulus of rigidity	G		7.93e10	$\mathrm{N\,m^{-2}}$
	Axial stiffness	C_{axial}	$(EA)/L_{max}$	6.87e8	$\mathrm{N\,m^{-1}}$
	Torsional stiffness	C_{radial}	$(GI_p)/L_{max}$	1.28e10	$\mathrm{N\,rad^{-1}}$
Piezo	Piezo stiffness	C_{piezo}		4e8	$\mathrm{N\,m^{-1}}$
Nut	Nut stiffness	C_{nut}		3.5e7	$\mathrm{N\,m^{-1}}$
Carriage	Carriage mass	m_{car}		1.6	kg

A.2 Model reduction bode plots

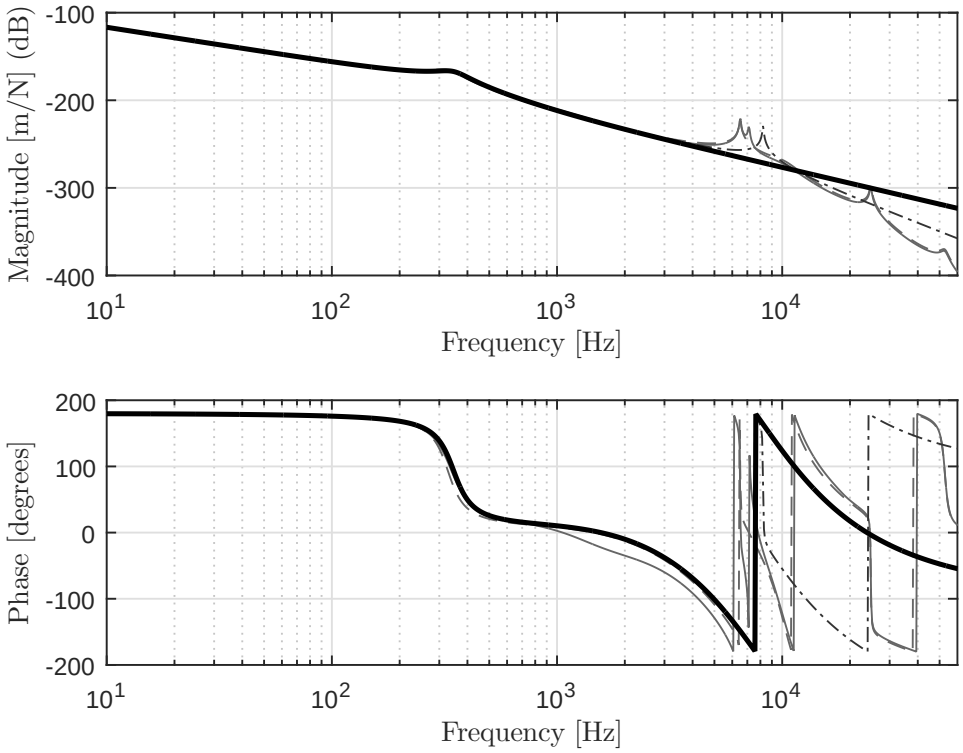

Fig. A.6. Bode plots of the transfer function from motor force [N] to resulting carriage position [m], for each model reduction step. Here the estimated stiffness, damping, and mass parameters are used.

APPENDIX B

System identification

B.1 FRF measurements using non-periodic excitation: the standard method

Direct open loop method

Consider an open loop system shown in Figure B.1.

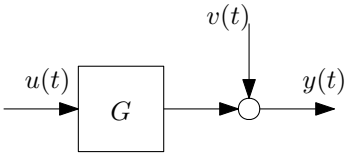

Fig. B.1. Block diagram of an open loop system.

Here G is the unknown plant that needs to be identified and $v(t)$ is an unkown disturbance noise. The output behaviour in the time domain can be written as

$$y(t) = G(f) * u(t) + v(t), \tag{B.1}$$

where $*$ indicates a convolution. The continuous time domain signals $u(t)$, $v(t)$ and $y(t)$ are measured at $t = nT_s$, $\forall n = [0, 1, \ldots, N-1]$, with T_s the sampling time and N is the number of samples. These discretized time domain signals can be transformed to the frequency domain using the Discrete Fourier Transform (DFT):

$$X(k) = \frac{1}{\sqrt{N}} \sum_{t=0}^{N-1} x(nT_s) e^{-j2\pi kn/N}, \tag{B.2}$$

with k the discrete time index and where $x(nT_s)$ can be replaced by $u(nT_s)$, $v(nT_s)$ or $y(nT_s)$ to obtain the DFT's $U(k)$, $V(k)$ and $Y(k)$ respectively. Now the DFT of the

input-output behaviour is given by:

$$Y(k) = G(k)U(k) + V(k), \tag{B.3}$$
$$Y(k)U^*(k) = G(k)U(k)U^*(k) + V(k)U^*(k), \tag{B.4}$$
$$S_{yu}(k) = G(k)S_{uu}(k) + S_{vu}(k), \tag{B.5}$$

where S_{yu} is the Cross Power Spectral Density (CPSD) of the input and the output, S_{vu} the CPSD of the input and the noise and S_{uu} the Auto PSD of the input. By making sure that the input and the noise are uncorrelated (e.g. by choosing $u(t)$ as white noise), the CPSD S_{vu} becomes zero, and an estimate of the plant G can be calculated by

$$G(k) \approx \frac{S_{yu}}{S_{uu}}. \tag{B.6}$$

Enhancing the spectral estimation

In practice, any measurement is inherently disturbed by e.g. system non-linearities (friction, stick-slip, backlash etc.), stochastic effects (noise, disturbance) and measurement errors. To improve plant estimate in (B.6), the results are averaged over M data series:

$$G(k) \approx \frac{\sum_{i=1}^{N} S_{yu}^i(k)}{\sum_{i=1}^{N} S_{uu}^i(k)}. \tag{B.7}$$

The most used method is Welch's averaged modified periodogram method. With this method, the entire data set of length L is split into M frames, each of length N samples. A window (e.g. Hanning window) is applied to each frame to prevent leakage caused by the discontinuities as a result of this cutting. However applying a window results in data loss at the frame boundaries. To resolve this, more frames are created by overlapping the M frames by $N-R$ segments and apply the window to these overlapping frames. See Figure B.2. This procedure is automated in MATLAB with the function `tfestimate`.

Coherence

A measure to quantify the quality of the obtained FRF is the coherence $C(k)$. It measures how much of the output power is coherent (linearly related) with the input power. To motivate this, consider again the open loop block diagram shown in Figure B.1. The DFT of the input-output behaviour can be written as

$$\begin{aligned} Y(k) &= G(k)U(k) + V(k), \\ Y(k)Y^*(k) &= G(k)U(k)Y^*(k) + V(f)Y^*(k), \\ S_{yy}(k) &= G(k)S_{uy}(k) + S_{vy}(k). \end{aligned}$$

Here it is again assumed that the input $u(t)$ and the disturbance on the output $v(t)$ are uncorrelated, so $S_{uv}(k) = 0$.

The quality of the measurement is determined by $S_{vy}(k)$. For a reliable measurement $S_{vy}(k)$ should be small, such that $|S_{yy}(k)| = |G(f)S_{uy}(k)|$, which means that the output

power is directly related to the plant. This ratio defines the coherence function $C(k)$

$$C(k) = \left| \frac{G(k)S_{uy}(k)}{S_{yy}(k)} \right| = \left| \frac{S_{yu}(k)S_{uy}(k)}{S_{uu}(k)S_{yy}(k)} \right|. \tag{B.8}$$

Or, when averaging is used:

$$C(k) = \left| \frac{\sum_{i=1}^{N} S_{yu}^{i}(k) \sum_{i=1}^{N} S_{uy}^{i}(k)}{\sum_{i=1}^{N} S_{uu}^{i}(k) \sum_{i=1}^{N} S_{yy}^{i}(k)} \right|. \tag{B.9}$$

The measurement is reliable when each data series in N yields the same PSD's, i.e. when $S_{\cdot\cdot}^{i}(k) \approx S_{\cdot\cdot}^{j}(k)$, $\forall i \neq j$. Then the coherence $C(k) \approx 1$ which means that the relation from u to y is mostly linear for that frequency. So when $C(k) < 1$ at a certain frequency, it indicates the presence of:

- Non-linearities in $G(k)$
- Dominant (measurement) noise sources
- Leakage errors of the DFT
- Other inputs or disturbances contributing to the output

The coherence can be calculated with MATLAB by using the function `mscohere.m`

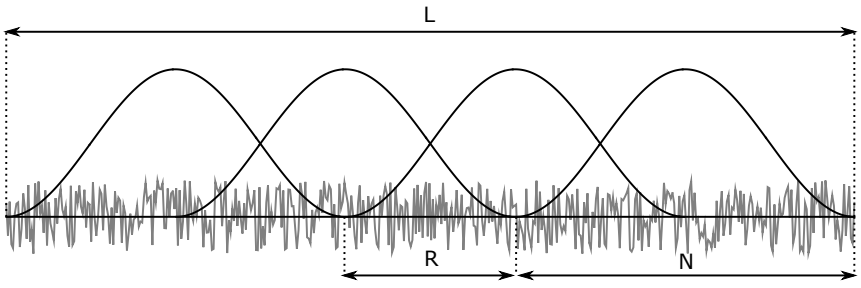

Fig. B.2. Principle of the windowed overlapped segment averaging: the signal of length L is divided into M (4) windowed segments of length N with an overlap of R samples.

Indirect closed loop method

In many practical applications it is desired to identify the dynamics of the system in closed loop. Consider a standard unity feedback system as shown in Figure B.3.

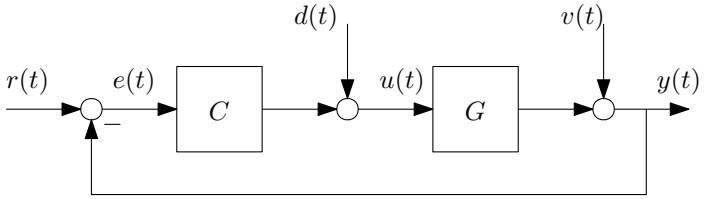

Fig. B.3. Block diagram of a closed loop system with unity feedback.

In the closed loop case, it is no longer possible to simply use (B.6), since now the noise $v(t)$ is added to the input $u(t)$ through the feedback loop, resulting in a correlation between $u(t)$ and $v(t)$. A possible solution is to use the so-called indirect three-point method. With this method, a disturbance $d(t)$ is applied and both $u(t)$ and $e(t)$ are measured. Now the Sensitivity S and Process Sensitivity PS can be calculated by:

$$S = \frac{1}{1+CG} \approx \frac{\sum_{i=1}^{N} S_{ud}^{i}}{\sum_{i=1}^{N} S_{dd}^{i}} \tag{B.10}$$

$$, -PS = \frac{G}{1+CG} \approx \frac{\sum_{i=1}^{N} S_{ed}^{i}}{\sum_{i=1}^{N} S_{dd}^{i}}, \tag{B.11}$$

where averaging is used to increase the spectral estimation, similar as done above. Dividing PS by S gives an estimate for the plant G:

$$\frac{PS}{S} = \frac{G}{1+CG} \cdot \frac{1+CG}{1} = G. \tag{B.12}$$

The coherence of both d $\rightarrow$ u and d $\rightarrow$ e can be checked to quantify the quality of both measurements. Care has to be taken that the reference $r(t)$, the disturbance $d(t)$ and the noise $v(t)$ are uncorrelated, otherwise biases could deteriorate the plant estimation significantly.

B.2 FRF measurements using periodic excitations: the Local Polynomial Method

The standard method of identifying the dynamical behaviour of a system described above assumes that the plant G is linear. In practice however, no system is completely linear, e.g. due to friction. Since a FRF is a linear mapping from the input to the output of a system, the goal is to obtain a Best Linear Approximation (BLA) of the dynamical behaviour using a Local Polynomial Method.

The Local Polynomial Method (LPM) is a procedure for nonparametric estimation of the FRF of a nonlinear system based on the Best Linear Approximation (BLA). Compared with other nonparametric FRF estimates based on windowing techniques (e.g. noise injection, see the method above), it has proved to be remarkably efficient in reducing the leakage errors caused by the application of Fourier Transform techniques to non-periodic data. The LPM can estimate FRF models of systems excited by both periodic and arbitrary signals. Here a periodic multisine signal will be used.

Multisine signal

A generalized multisine $u(t)$ is a signal consisting of F sine waves with different frequencies f_k, amplitudes A_k and phase shifts ϕ_k:

$$u(t) = \frac{1}{\sqrt{F}} \sum_{k=1}^{F} A_k \sin(2\pi f_k t + \phi_k). \tag{B.13}$$

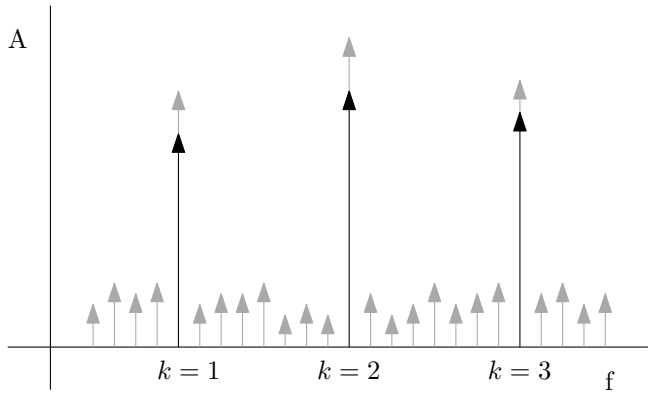

Fig. B.4. Amplitude of the Laplace transform as a function of frequency. The excited frequencies are given by the black arrows, the transient and the noise contributions on all frequencies are given by the grey arrows.

Random-phase multisines are used, which means that ϕ_k is the outcome of an uniform random process over $[0,\ 2\pi]$. The frequency grid $\{f_1, f_2, \ldots, f_F\}$ and amplitudes at these frequencies have to be specified and can be chosen in such a way that a more dense frequency grid with higher amplitudes is present in the range where resonance peaks are expected. The period of the complete multisine, $T_{u(t)}$, is the least common multiple of the periods of its individual components

$$T_{u(t)} = \text{lcm}\{T_1, T_2, \ldots, T_F\} = \text{lcm}\{f_1^{-1}, f_2^{-1}, \ldots, f_F^{-1}\}, \tag{B.14}$$

if a common multiple exists, i.e. $T_{u(t)} = n_1 T_1 = \ldots = n_F T_F$ with $n_i \in N_0$ for $i \in \{1, \ldots, F\}$.

The Local Polynomial Method

Consider again a SISO system G that is excited by a known input signal $u(t)$ and whose output is the sum of the input contribution and of a disturbance term $v(t)$ where the input-output system can be represented as

$$Y(k) = G_k U_k + T_k + V_k. \tag{B.15}$$

The basic idea of the LPM is, based on the smoothness of the transfer function G and the transient term T as functions of frequency, to approximate these functions in a narrow frequency band around a central frequency Ω_k by a polynomial. The polynomial parameters are estimated from the experimental data collected in this frequency band. Next G_k, at the central frequency Ω_k, is retrieved from this local polynomial model as the estimate of the FRF at that frequency.

For the excitation with periodic signals it is key to exploit excited and non-excited frequency bins within the total input spectrum. The non-excited frequencies $k \neq \varepsilon P$ will contain the measurement noise and other non-periodic disturbances such as leakage/transient effects. These perturbations are also present on the excited frequencies, in combination with the periodic content, see Figure B.4. Because a periodic excitation

signal is used, it is possible to separate the transient and plant estimation. For this, start with an estimation of the transient effects at the non-excited frequencies. This output spectrum is defined as

$$Y(\varepsilon P + \rho) = T(\Omega_{\varepsilon P+\rho}) + \widetilde{V}(\varepsilon P + \rho),$$

with $\rho = -d, -(d-1), \ldots, -1, 1, \ldots, d-1, d$ a local frequency window **over the non-excited frequencies** and $\widetilde{V}(\varepsilon P+\rho)$ the non-periodic disturbances to the measurement. Note that ρ does not include the excited frequency, so the plant dynamics are not included in this output spectrum.

Now write this transient as a polynomial M:

$$T(\Omega_{\varepsilon P+\rho}) = M(\varepsilon P + \rho).$$

This polynomial $M(\varepsilon P + \rho)$ is parametrized using a Taylor series expansion and the resulting set of equations can be solved using a least squares optimization. The optimal solution of this optimization results in the estimation of the transient **at the excited frequency** $\widehat{T}(\Omega_{\varepsilon P})$.

Doing this around each excited frequency gives an estimate of the transient effects at each excited frequency, $\widehat{T}(\Omega_{\varepsilon P})$. Now the transient effects can be decreased significantly in the output spectrum by subtracting the estimated transient effect at the excited frequency, from the output spectrum at that frequency:

$$\widehat{Y}(\varepsilon P) = Y(\varepsilon P) - \widehat{T}(\Omega_{\varepsilon P}). \tag{B.16}$$

So now (B.15) can be simplified, resulting in the **noise-corrected output spectrum**:

$$\widehat{Y}(\varepsilon P) = G(\Omega_{\varepsilon P})U(\varepsilon P) + V(\varepsilon P), \tag{B.17}$$

with $V(\varepsilon P)$ the remaining transient effects and all disturbances. Now this noise-corrected output spectrum can be used to calculate the plant dynamics.

B.3 FRF measurements

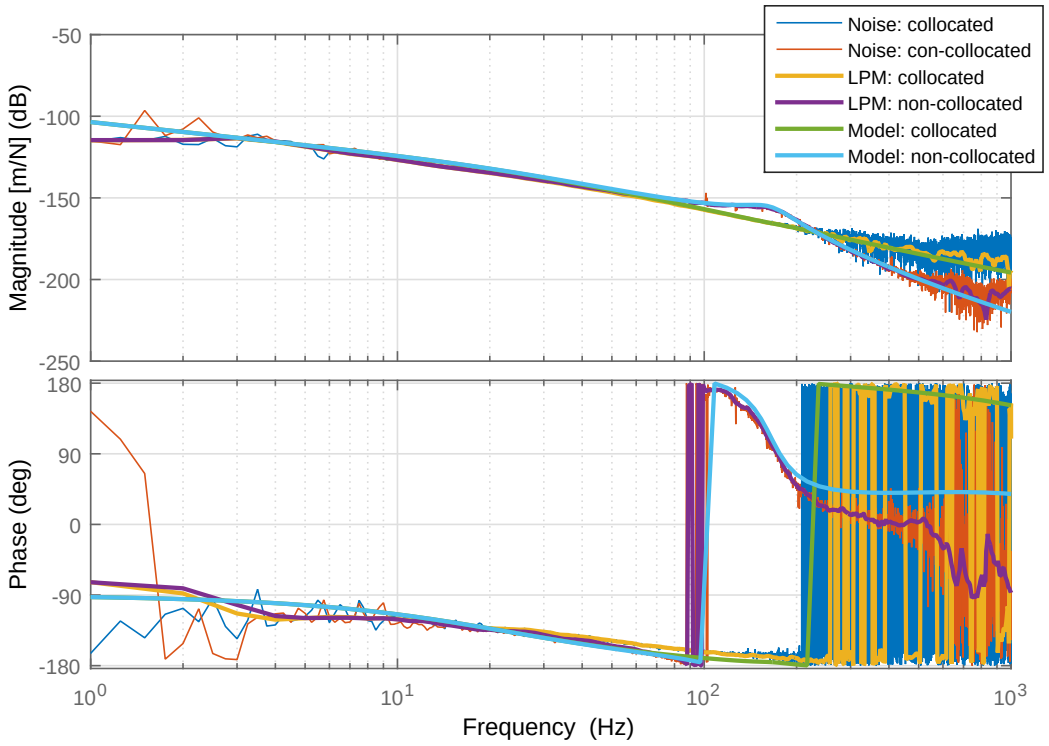

Fig. B.5. Comparison between the model-based and the experimentally found bode plots of both the transfer function from the motor force to the (non-collocated) position of m_2, and the transfer function from the motor force to the (collocated) position of m_1, using the three-point method with noise injection and the LPM with multisine injection.

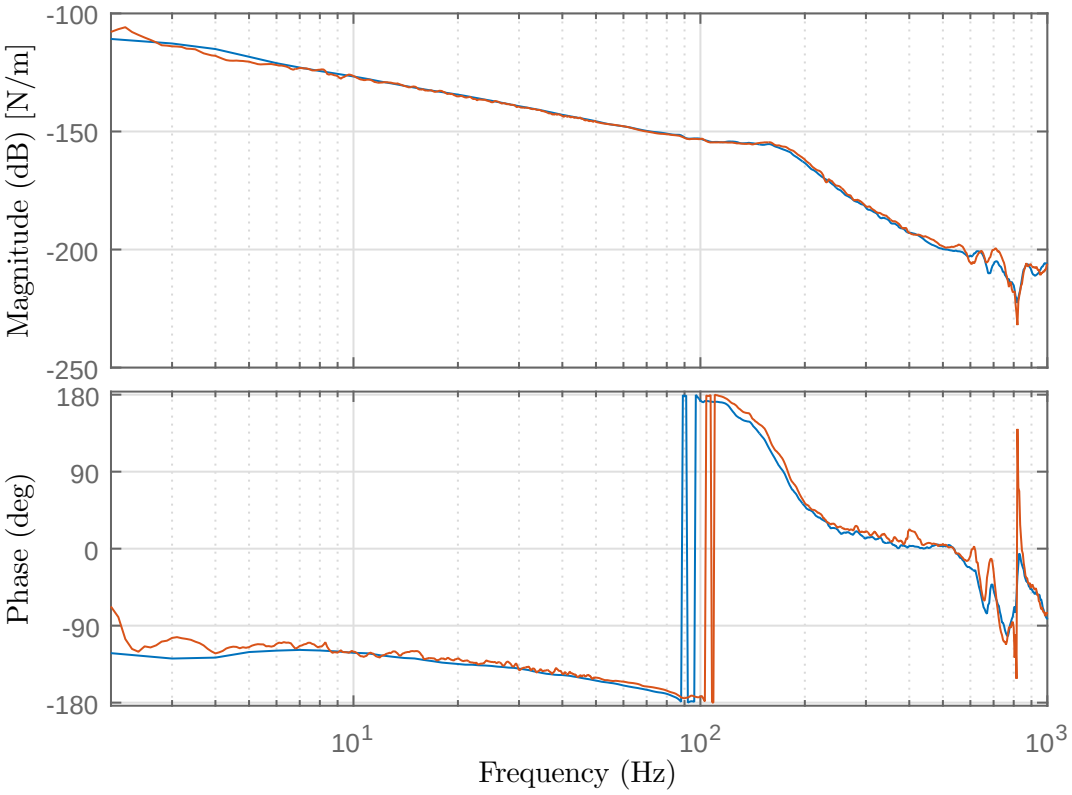

Fig. B.6. Bode plot of the transfer function from the motor force to the (non-collocated) position of m_2, using the LPM with multisine injection. A comparison of two separate measurements shows similar high-frequency behaviour.

APPENDIX C

Robustness margins

The resulting robustness margins for the closed-loop system using the classical tuned PID controller are given in Tab. C.1. The open-loop bode plot, the Nyquist plot and the Sensitivity plot, including graphical representations of the robustness margins are given in Fig. C.1, Fig. C.2 and Fig. C.3, respectively.

Table C.1: Control margins

Parameter	**Value**
Crossover frequency	36 Hz
Gain margin (GM)	14 dB
Phase margin (PM)	31°
Modulus margin (MM)	6.2 dB

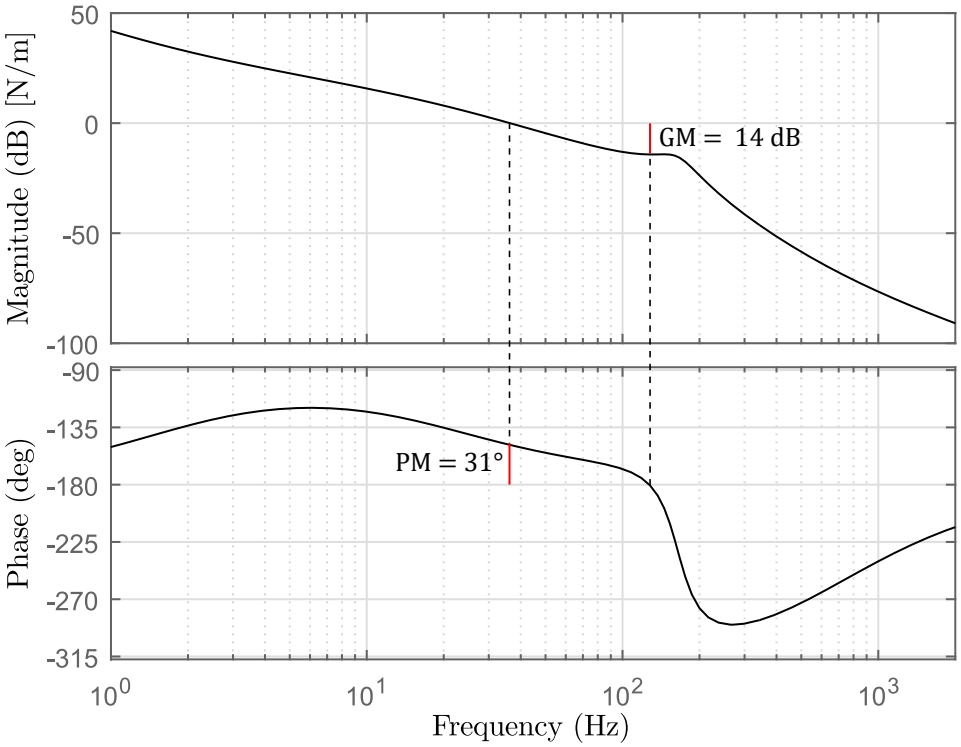

Fig. C.1. Bode plot: open loop $G \cdot C$.

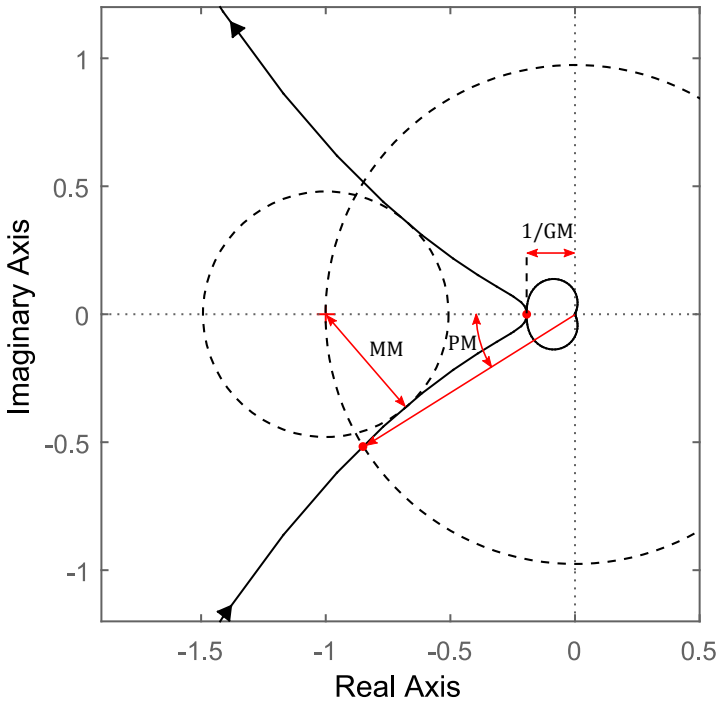

Fig. C.2. Nyquist plot: open loop $G \cdot C$.

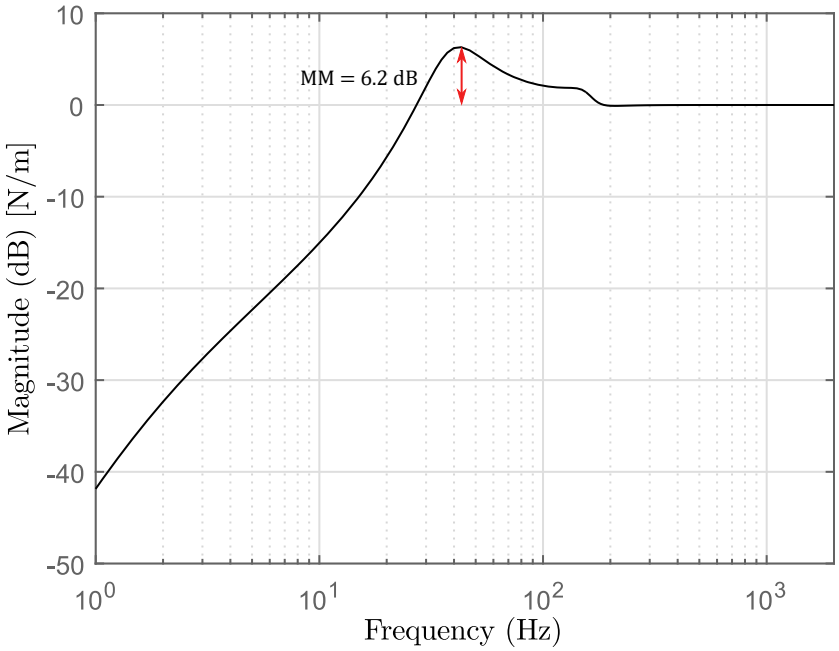

Fig. C.3. Sensitivity plot: $\frac{1}{1+G \cdot C}$.

APPENDIX D

Position dependency

D.1 Spindle orientation

To elaborate on the spindle orientation dependency, consider Fig. D.1. Here a setpoint is given such that the spindle rotates 45°, or 1/8 rotation, and the system is given 30 seconds to settle. The carriage is kept, approximately, in the same position, only moving 0.5 mm due to a single rotation of the spindle. This way, the settling response at 8 different spindle orientations is investigated. This is repeated 3 times and the settling response is shown in Fig. D.1. Comparing different spindle orientations, shows different settling behaviour. A (relative) spindle orientation of 135° results in much more oscillations, compared to for example a (relative) spindle orientation of 225°. Comparing the four separate experiments done for each spindle orientation, shows (generally) repeatable settling behaviour, confirming the claim that the orientation of the spindle does indeed influence the settling behaviour significantly.

D.2 Carriage position

The carriage position also influences the settling response, see Fig. D.2. Here, the spindle is rotated $8 \cdot 360°$, resulting in a carriage displacement of 4 mm and a constant final spindle orientation, comparable to the relative spindle orientation of 135° in Fig. D.1. This movement is repeated 10 times, covering the entire 4 cm long workspace. This entire set of 10 movements is repeated in three separate experiments.

The first two movements in Fig. D.2 are related to a carriage position close to the bearing (refer to the description of experimental setup in Fig. 2.2), and have a different settling response compared to the rest.

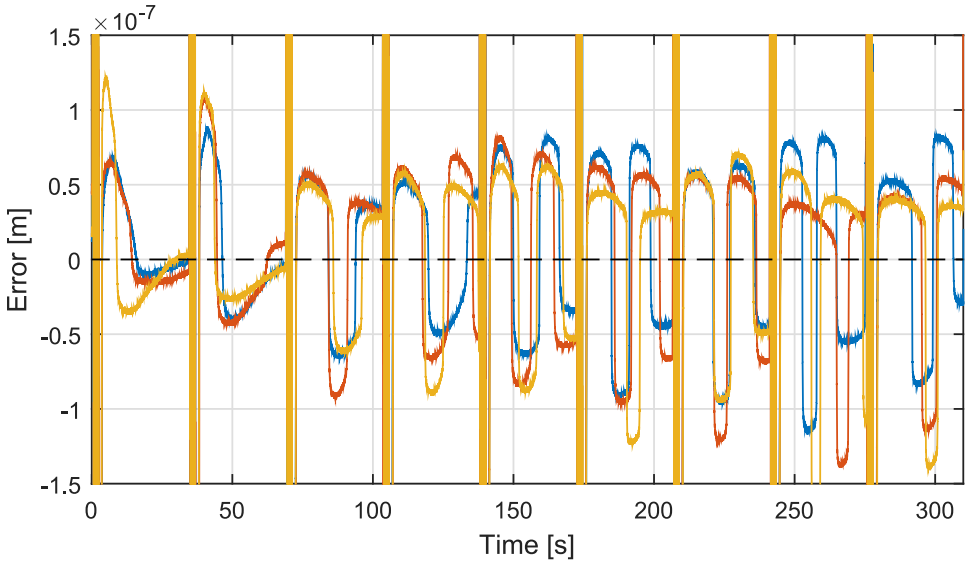

Fig. D.2. Three identical experiments, each consisting of 10 spindle rotations where the spindle end-orientation is kept the same. Therefore this shows the effect of the carriage position on the settling response.

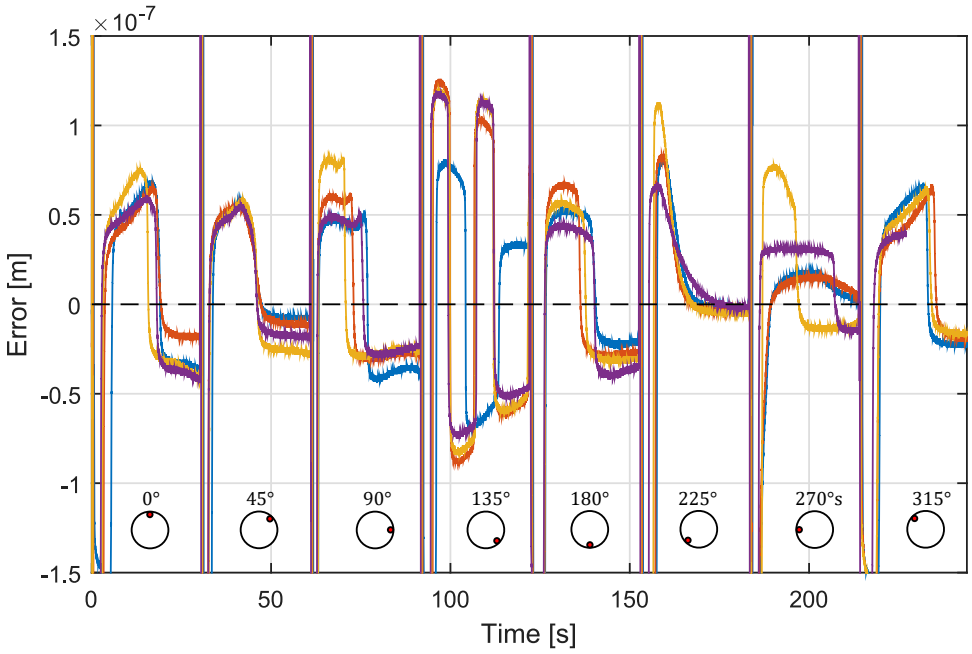

Fig. D.1. Repeated settling experiments for 8 different spindle orientations, showing the effect of the spindle orientation on the settling response. The spindle relative spindle orientation is shown in the bottom part of the plot.

APPENDIX E

Equilibrium set

The closed-loop equation of motion can be written as

$$\dot{x} = (A + BK)x + Gw. \tag{E.1}$$

E.1 PD-controlled system

Filling in the system matrices corresponding to PD-control in (E.1) gives

$$\begin{bmatrix} \dot{x}_1 \\ \dot{x}_2 \\ \ddot{x}_1 \\ \ddot{x}_2 \end{bmatrix} = \left(\begin{bmatrix} 0 & 0 & 1 & 0 \\ 0 & 0 & 0 & 1 \\ -\frac{k}{m_1} & \frac{k}{m_1} & -\frac{d}{m_1} & \frac{d}{m_1} \\ \frac{k}{m_2} & -\frac{k}{m_2} & \frac{d}{m_2} & -\frac{d}{m_2} \end{bmatrix} + \begin{bmatrix} 0 \\ 0 \\ -\frac{1}{m_1} \\ 0 \end{bmatrix} \begin{bmatrix} 0 \\ K_c \\ 0 \\ T_d K_c \end{bmatrix}^T \right) \begin{bmatrix} x_1 \\ x_2 \\ \dot{x}_1 \\ \dot{x}_2 \end{bmatrix} + \begin{bmatrix} 0 \\ 0 \\ 0 \\ -1 \end{bmatrix} F_s \text{Sign}(\dot{x}_2). \tag{E.2}$$

The equilibrium set of (E.2) is found by setting the state derivatives to zero, $\dot{x}_1 = \dot{x}_2 = \ddot{x}_1 = \ddot{x}_2 = 0$, resulting in

$$\begin{bmatrix} 0 \\ 0 \\ 0 \\ 0 \end{bmatrix} = \left(\begin{bmatrix} 0 & 0 & 1 & 0 \\ 0 & 0 & 0 & 1 \\ -\frac{k}{m_1} & \frac{k}{m_1} & -\frac{d}{m_1} & \frac{d}{m_1} \\ \frac{k}{m_2} & -\frac{k}{m_2} & \frac{d}{m_2} & -\frac{d}{m_2} \end{bmatrix} + \begin{bmatrix} 0 \\ 0 \\ -\frac{1}{m_1} \\ 0 \end{bmatrix} \begin{bmatrix} 0 \\ K_c \\ 0 \\ T_d K_c \end{bmatrix}^T \right) \begin{bmatrix} x_1 \\ x_2 \\ 0 \\ 0 \end{bmatrix} + \begin{bmatrix} 0 \\ 0 \\ 0 \\ -1 \end{bmatrix} F_s \text{Sign}(0). \tag{E.3}$$

This can also be written as

$$\begin{cases} -\frac{k}{m_1} x_1 + \frac{k - K_c}{m_1} x_2 = 0, \\ \frac{k}{m_2} x_1 - \frac{k}{m_2} x_2 - \frac{1}{m_2} F_s \text{Sign}(0) = 0. \end{cases} \tag{E.4}$$

Solving (E.4) for x_1 and x_2 results in the equilibrium sets

$$\begin{cases} x_1 \in -\frac{k-K_c}{kK_c} F_s \text{Sign}(0), \\ x_2 \in -\frac{F_s}{K_c} \text{Sign}(0), \\ \dot{x}_1 = 0, \\ \dot{x}_2 = 0. \end{cases} \tag{E.5}$$

E.2 PID-controlled system

Filling in the system matrices corresponding to PID-control in (E.1) gives

$$\begin{bmatrix} \dot{x}_1 \\ \dot{x}_2 \\ \ddot{x}_1 \\ \ddot{x}_2 \\ \dot{\xi} \end{bmatrix} = \left(\begin{bmatrix} 0 & 0 & 1 & 0 & 0 \\ 0 & 0 & 0 & 1 & 0 \\ -\frac{k}{m_1} & \frac{k}{m_1} & -\frac{d}{m_1} & \frac{d}{m_1} & 0 \\ \frac{k}{m_2} & -\frac{k}{m_2} & \frac{d}{m_2} & -\frac{d}{m_2} & 0 \\ 0 & 1 & 0 & 0 & 0 \end{bmatrix} + \begin{bmatrix} 0 \\ 0 \\ -\frac{1}{m_1} \\ 0 \\ 0 \end{bmatrix} \begin{bmatrix} 0 \\ K_c \\ 0 \\ T_d K_c \\ T_i K_c \end{bmatrix}^T \right) \begin{bmatrix} x_1 \\ x_2 \\ \dot{x}_1 \\ \dot{x}_2 \\ \xi \end{bmatrix} + \begin{bmatrix} 0 \\ 0 \\ 0 \\ -1 \\ 0 \end{bmatrix} F_s \text{Sign}(\dot{x}_2). \tag{E.6}$$

The equilibrium set of (E.6) is found by setting the states derivatives to zero, $\dot{x}_1 = \dot{x}_2 = \ddot{x}_1 = \ddot{x}_2 = \dot{\xi} = 0$ resulting in

$$\begin{bmatrix} 0 \\ 0 \\ 0 \\ 0 \\ 0 \end{bmatrix} = \left(\begin{bmatrix} 0 & 0 & 1 & 0 & 0 \\ 0 & 0 & 0 & 1 & 0 \\ -\frac{k}{m_1} & \frac{k}{m_1} & -\frac{d}{m_1} & \frac{d}{m_1} & 0 \\ \frac{k}{m_2} & -\frac{k}{m_2} & \frac{d}{m_2} & -\frac{d}{m_2} & 0 \\ 0 & 1 & 0 & 0 & 0 \end{bmatrix} + \begin{bmatrix} 0 \\ 0 \\ -\frac{1}{m_1} \\ 0 \\ 0 \end{bmatrix} \begin{bmatrix} 0 \\ K_c \\ 0 \\ T_d K_c \\ T_i K_c \end{bmatrix}^T \right) \begin{bmatrix} x_1 \\ x_2 \\ 0 \\ 0 \\ \xi \end{bmatrix} + \begin{bmatrix} 0 \\ 0 \\ 0 \\ -1 \\ 0 \end{bmatrix} F_s \text{Sign}(0). \tag{E.7}$$

This can also be written as

$$\begin{cases} -\frac{k}{m_1} x_1 + \frac{k - K_c}{m_1} x_2 - \frac{K_c T_i}{m_1} \xi = 0, \\ \frac{k}{m_2} x_1 - \frac{k}{m_2} x_2 - \frac{1}{m_2} F_s \text{Sign}(0) = 0, \\ x_2 = 0. \end{cases} \tag{E.8}$$

Solving (E.8) for x_1, x_2 and ξ results in the equilibrium sets

$$\begin{cases} x_1 \in -\frac{F_s}{k} \text{Sign}(0) \\ x_2 = 0, \\ \dot{x}_1 = 0, \\ \dot{x}_2 = 0, \\ \xi \in -\frac{F_s}{K_c T_i} \text{Sign}(0). \end{cases} \tag{E.9}$$

APPENDIX F

Routh-Hurwitz criteria

The Routh-Hurwitz criteria gives necessary and sufficient conditions for all of the roots of the characteristic polynomial to lie in the left half of the complex plane, and is defined as follows.

Routh-Hurwitz Criteria. *Given the polynomial*

$$P(\lambda) = \lambda^n + a_1\lambda^{n-1} + \cdots + a_{n-1}\lambda + a_n,$$

where the coefficients a_i are real constants, $i = 1, \cdots, n$, define the n Hurwitz matrices using the coefficients a_i of the characteristic polynomial:

$$H_1 = (a_1),\ H_2 = \begin{bmatrix} a_1 & 1 \\ a_3 & a_2 \end{bmatrix},\ H_3 = \begin{bmatrix} a_1 & 1 & 0 \\ a_3 & a_2 & a_1 \\ a_5 & a_4 & a_3 \end{bmatrix},$$

and

$$H_n = \begin{bmatrix} a_1 & 1 & 0 & 0 & \cdots & 0 \\ a_3 & a_2 & a_1 & 1 & \cdots & 0 \\ a_5 & a_4 & a_3 & a_2 & \cdots & 0 \\ \vdots & \vdots & \vdots & \vdots & \cdots & \vdots \\ 0 & 0 & 0 & 0 & \cdots & a_n \end{bmatrix},$$

where $a_j = 0$ if $j > n$. All of the roots of the polynomial $P(\lambda)$ are negative or have negative real part iff the determinants of all Hurwitz matrices are positive:

$$\det H_j > 0,\ j = 1, 2, \ldots, n.$$

Consider the system (4.4) without friction. The transfer function from input u to position of the second mass x_2 is given by:

$$G(s) = \frac{X_2(s)}{U(s)} = \frac{ds + k}{s^2(m_1m_2s^2 + (m_1 + m_2)ds + (m_1 + m_2)k)} \tag{F.1}$$

The transfer functions of a PD- and PID-controller respectively are given by

$$C_{PD}(s) = K_c(1 + T_d s), \tag{F.2}$$

$$C_{PID}(s) = K_c(1 + T_d s + \frac{T_i}{s}) = \frac{K_c(T_d s^2 + s + T_i)}{s}. \tag{F.3}$$

The closed-loop transfer function is given by

$$G_{CL}(s) = \frac{GC}{1 + GC}, \tag{F.4}$$

where C is either C_{PD} or C_{PID} and which denominator is the characteristic polynomial $\Phi_{CL}(s)$. Or the characteristic polynomial can be found directly by

$$\Phi_{CL}(s) = C_{den}(s)G_{den}(s) + C_{num}(s)G_{num}(s) = 0, \tag{F.5}$$

where the subscripts den and num represent the denominator and numerator of the transfer functions respectively.

Filling (F.1) and (F.2) or (F.3) in (F.5) give the characteristic equations for a PD- or PID-controlled system respectively, resulting in the following coefficients a_i for which the Routh-Hurwitz criteria can be checked.

PD: $a_1 = \frac{m_1+m_2}{m_1 m_2}$, $a_2 = \frac{(m_1+m_2)k+dK_cT_d}{m_1 m_2}$, $a_3 = \frac{kK_cT_d+dK_c}{m_1 m_2}$, $a_4 = \frac{kK_c}{m_1 m_2}$.

PID: $a_1 = \frac{m_1+m_2}{m_1 m_2}$, $a_2 = \frac{(m_1+m_2)k+dK_cT_d}{m_1 m_2}$, $a_3 = \frac{kK_cT_d+dK_c}{m_1 m_2}$, $a_4 = \frac{dK_cT_i+kK_c}{m_1 m_2}$, $a_5 = \frac{kK_cT_i}{m_1 m_2}$.

The overall controller gain K_c is the only varying parameter, so the closed-loop stability of the system can now be checked, depending on this parameter.

APPENDIX G

Absolute stability

G.1 Feasibility check

The system (4.6) is said to be absolutely stable if it has a globally uniformly asymptotically stable equilibrium point at the origin for any nonlinearity in a given sector [25]. In the case of Coulomb friction, this is the $[0, \infty]$ sector, which means that the friction characteristic is bounded within the first and third quadrant in Fig. 3.2. The circle criterion is stated as follows [25]:

(Circle criterion) *The system* (4.6) *is absolutely stable if* $\Psi \in [0, \infty]$ *and* (4.7) *is strictly positive real.*

The strictly positive real part is expressed in an LMI form based on the Kalman-Yakubovich-Popov lemma [25]:

(Kalman-Yakubovich-Popov) *Consider system* (4.4)*, with* $\Psi \in [0, \infty]$ *and the linear feedback law* (4.5)*. Then* (4.7) *is strictly positive real if and only if there exist a matrix* $P = P^T > 0$ *such that*

$$\begin{aligned} P(A + BK) + (A + BK)^T P &< 0 \\ PH &= C^T. \end{aligned} \tag{G.1}$$

A strictly positive real, minimal realization, LTI system is equivalent to a strictly passive system [25]. Consequently, by designing a controller K such that the KYP criterion (G.1) is fulfilled, the closed-loop system (4.6) is rendered absolutely stable. Since this criterion guarantees global asymptotic stability for all nonlinearities in a given sector, this controller would be robust against changes in friction, as long as the [0, ∞] bound is satisfied.

G.2 Controller synthesis

Instead of verifying the feasibility of a given controller, the KYP condition can be used to design a PID controller which renders the resulting closed-loop system asymptotically stable. For this, the PID-controller given in (4.9c) is expanded to a full-state feedback controller $K_{full} \in \mathbb{R}^{1x6}$ and the system matrices in (4.9) are adjusted accordingly. Solving the

Solving (G.1) for both $K = K_{full}$ and P results in a non-linear problem, due to the multiplication of K_{full} and P. These generally non-convex optimization problems cannot be solved by standard LMI techniques. Therefore, before the KYP conditions can be used for controller design, a change in variables is needed to render the problem linear. This results in the following LMI condition:

$$\begin{bmatrix} AQ + BZ + QA^T + Z^T B^T & H - QC^T \\ H^T - CQ & 0 \end{bmatrix} < 0, \tag{G.2}$$

where $Q = P^{-1}$ and $Z = K_{full}Q$. For the derivation of (G.2), refer to Appendix G.3. A controller gain matrix $K_{full} \in \mathbb{R}^{1x6}$ can be found by solving (G.2) for Q and Z and then solve for $K_{full} = ZQ^{-1}$. However, this problem also turned out to be infeasible. Therefore, it is concluded that designing a controller based on absolute stability is too restrictive for this particular system.

G.3 KYP change of variables

Before the KYP conditions can be used for controller design, a change in variables is needed, to render the problem linear. The change in variables is given as follows.

$$\begin{bmatrix} P(A+BK) + (A+BK)^T P & PH - C^T \\ H^T P - C & 0 \end{bmatrix} < 0 \tag{G.3a}$$

$$\begin{bmatrix} P^{-1} & 0 \\ 0 & I \end{bmatrix} \begin{bmatrix} P(A+BK) + (A+BK)^T P & PH - C^T \\ H^T P - C & 0 \end{bmatrix} \begin{bmatrix} P^{-1} & 0 \\ 0 & I \end{bmatrix} < 0 \tag{G.3b}$$

$$\begin{bmatrix} (A+BK)P^{-1} + P^{-1}(A+BK)^T & H - P^{-1}C^T \\ H^T - CP^{-1} & 0 \end{bmatrix} < 0; Q = P^{-1} \tag{G.3c}$$

$$\begin{bmatrix} (A+BK)Q + Q(A+BK)^T & H - QC^T \\ H^T - CQ & 0 \end{bmatrix} < 0 \tag{G.3d}$$

$$\begin{bmatrix} AQ + BKQ + QA^T + QK^T B^T & H - QC^T \\ H^T - CQ & 0 \end{bmatrix} < 0; Z = KQ \tag{G.3e}$$

$$\begin{bmatrix} AQ + BZ + QA^T + Z^T B^T & H - QC^T \\ H^T - CQ & 0 \end{bmatrix} < 0 \tag{G.3f}$$